# UC Riverside

## UC Riverside Electronic Theses and Dissertations

### Title

Dynamic Precision Measurement of the Casimir Force using Short Coherence Length Fiber-Based Interferometer

### Permalink

https://escholarship.org/uc/item/72s13831

### Author

Chang, Chia-Cheng

### Publication Date

2010

Peer reviewed|Thesis/dissertation

eScholarship.org Powered by the California Digital Library
University of California

UNIVERISTY OF CALIFORNIA

RIVERSIDE

# Dynamic Precision Measurement of the Casimir Force Using Short Coherence length Fiber-based Interferometer

A Dissertation submitted in partial satisfaction

of the requirements for the degree of

Doctor of Philosophy

in

Physics

by

Chia-Cheng Chang

March 2011

Dissertation Committee:

Professor Umar Mohideen, Chairperson

Professor Harry W.K. Tom

Professor Roya Zandi

Copyright by

Chia-Cheng Chang

2011

The Dissertation of Chia-Cheng Chang is approved:

_____

_____

_____

Committee Chairperson

University of California, Riverside

# ACKNOWLEDGEMENTS

It would not have been possible to complete this dissertation without the great support and help of a number of people whom I would like to recognize and thank. First of all, I would like to express my deepest appreciation to Professor Umar Mohideen for his expert guidance and enthusiastic commitment to my dissertation. I also want to extend my special thanks to my committee members, Professor Harry W.K. Tom and Professor Roya Zandi for their thoughtful insights and comments to help develop my research. Special gratitude is also extended to Professor V.M. Mostepanenko and Professor G.L. Klimchitskaya for the theoretical supports.

My heartfelt appreciation goes out to all the people who have helped me over the years. I would like to especially express my profound gratitude to my lab colleague, Rodrigo, shomeekm, Douglas Chiu, Vector Chen and Gui Dong Wei Liu and Feng Chen for their assistance and to my best friends in Physics Dept. of Riverside, Kevin Kao, Feng Miao and Kyle Pi ,who always encourage me and give me useful advices. I am specially indebted to Miss Ching-Fen Tsai. Without her encouragement, I can never finish this work.

Finally, I express my deep gratitude to my wonderful family. My elder sister, Chang Chiung Wen always believed in me and help me taking care of our parents. Of course, I would like to thank my parents, Mr. Cheng-Chung Chang and and Mrs. Shie Huei Ying for their unending love and support.

# DEDICATION

To Pro. Wun-Shain Fann (1961~2008) who has always been my inspiration through my arduous journey.

ABSTRACT OF THE DISSERTATION

Dynamic Precision Measurement of the Casimir Force

using

Short Coherence length Fiber-based Interferometer

by

Chia-Cheng Chang

Doctor of Philosophy, Graduate Program in Physics

University of California, Riverside, March 2011

Professor Umar Mohideen, Chairperson

The Casimir effect has become very important in modern physics since its prediction in 1948. Not only is it the most accessible evidence of vacuum fluctuations in macroscopic systems but also has important applications in many areas such as condensed matter physics, atomic physics, cosmology and nano-technology. Therefore, the theoretical activity in the analysis of the Casimir effect has dramatically increased in the past 60 years. To provide deeper insights, precise Casimir force measurements are necessary. Here, we develop a high precision dynamic Casimir force measurement system based on short coherence length fiber-optics interferometer in UHV. The frequency modulation (FM) technique and precise calibration are the key points to achieve a high precision in the Casimir force measurement. It is also the first time in our

group; random errors are reduced to be smaller than systematic errors. The Casimir force was measured between a Au-coated sphere and Au-coated plate using FM technique. A comparison to the theory where the description of the permittivity using the generalized Plasma and Drude model is done. In addition, Casimir Pressure measurement between a Au-coated sphere and Ito plate will be presented.

# List of Tables

# List of Figures

# Chapter 1. Introduction of Casimir effect[1]

Recent years have seen increased attention being given to Casimir force measurement in quantum physics. This is because it provides the most direct evidence of the existence of zero point vacuum oscillation is the Casimir effect which was predicted by Casimir in 1948. He showed that one consequence of the zero-point field fluctuations is an attractive force between the two electrically neutral, perfect conducing, and infinitely large parallel plates. Unlike other evidence such as Lamb shift, spontaneous emission or atomic stability, the Casimir effect has potential applications in micro- or nanotechnology, because of its unique shape dependence not to mention its importance in multidisciplinary areas. In beginning of this chapter, we will discuss the physical foundations of Casimir effect and the simplest case, Casimir effect between ideal metals. This is followed by some background information on the research. Finally, the overview of my thesis is presented.

## 1.1 The origin of Casimir effect

### 1.1.1 Zero-point energy

Zero point energy is one of the most interesting results in quantum theory. It is also the source of Casimir effect. To better understand the Casimir effect, it is worthwhile to briefly review the harmonic oscillator in quantum mechanics.

The basis of quantum field theory is the representation of the field as a system of oscillators. The Hamiltonian of each state $H_k$ has the eq. (1-1) as below:

$$E = \sum_k H_k = \sum_k \frac{1}{2}\left(P_k^2 + \omega_k^2 Q_k^2\right) \tag{1-1}$$

Where the $P_k$ and $Q_k$ are quantum mechanical operators.

Because of the commutation rule $\left[a_k, a_k^+\right] = \delta_{k,k'}$, we can define the operator and its ad-joint eq. (1-2) and (1-3)

$$a_k = \left(2\hbar\omega_k\right)^{-\frac{1}{2}}\left(\omega_k Q_k + iP_k\right) \tag{1-2}$$

$$a_k^+ = \left(2\hbar\omega_k\right)^{-\frac{1}{2}}\left(\omega_k Q_k - iP_k\right) \tag{1-3}$$

The eq. (1-1)-(1-3) allow us to write the Hamiltonian in the form

$$H = \sum_k \left( a_k^+ a_k + \frac{1}{2}\right)\hbar\omega_k \tag{1-4}$$

The harmonic oscillator has discrete energy levels which are given by

$$E = \sum_k \left( n_k + \frac{1}{2}\right)\hbar\omega_k \tag{1-5}$$

Where the k is the wave factor, $\omega_k$ is the angular frequency of the oscillator and $n_k$ =1,2,3…. is number of energy quanta. According to the eq. (1-5), the sum energy of the vacuum (ground state $n_k$ =0) is given by:

$$E = \sum_K \frac{1}{2}\hbar\omega_K$$

.

## 1.1.2 Casimir effect due to zero point energy fluctuation

Obviously, from the above equation, we know that the vacuum energy is infinite in free space. This is one of the manifestations of the problem of ultraviolet divergences. Casimir first subtracted the infinite vacuum energy of the quantized electromagnetic field in the presence of ideal conductor plane, from the infinite vacuum energy to the same field in free Minkowski space. Mathematically speaking, to obtain a finite value immediately from the subtraction of two infinite numbers a procedures such as regularization and renormalization have to be used. Based on these two techniques, the derivation of the attractive Casimir force between two ideal metal plates can be expressed as follows. Assuming two ideal conducting plates are closely spaced at a distance L from each other in vacuum, the electromagnetic fields are given by boundary condition on plate surfaces. In the bounded region as shown in figure 1.1, the electromagnetic field is subject to the Dirichelt and Neumann boundary condition ($n \cdot B = 0$ and $n \times E = 0$). Some

of the wave vector components become discrete in the perpendicular direction because of the tangential component of the electric field vanish on the metal surface.

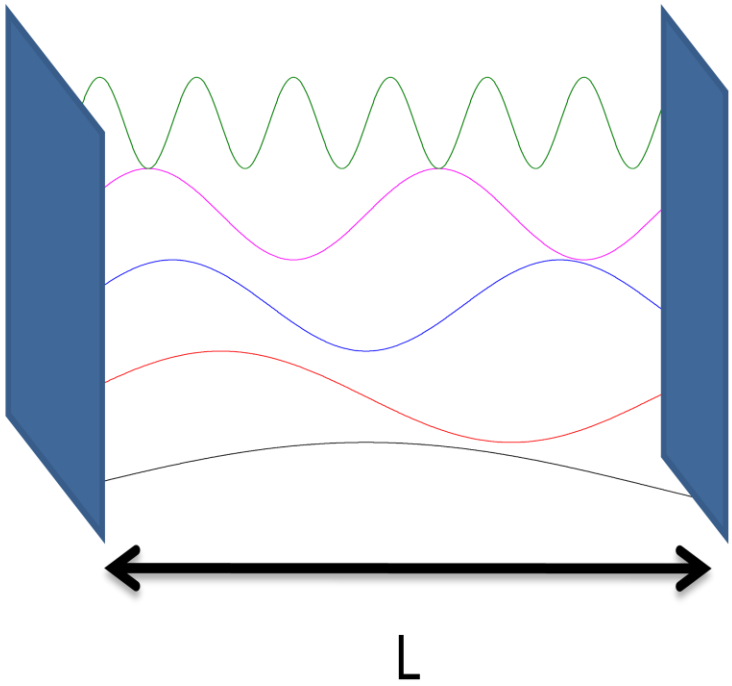


Figure1- 1 Two perfect conducting parallel plates experience an attractive force due to the zero-point electromagnetic field. Only certain modes are allowed, which are given by the boundary conditions that could exist inside the cavity.

For example, the modes of the electromagnetic field are labeled by a three dimensional wave vector k. Thus, the frequency is given by eq. (1-6)

$$\omega_k = c\sqrt{k^2} = c\sqrt{k_x^2 + k_y^2 + k_z^2} \tag{1-6}$$

At the boundaries (z-axis), $k_z = \frac{\pi n}{L}$, $n \in (0, \pm 1, \pm 2...)$, while $k_x$ and $k_y$ are continuous components. The sum of vacuum energy from eq. (1-5) is

$E_0(L) = \frac{\hbar}{2} \int \frac{dk_x dk_y}{(2\pi)^2} \sum_{n=-\infty}^{n=\infty} \omega_{k_x, k_y, n} \cdot A$ , where A is the area of the metal plate.

The vacuum energy is infinite in any given condition. The potential energy of system when the plates are separated by a distance L is $U_{casimir}(L) = E_0(L) - E_0(\infty)$, the energy required to bring the plates from far distance to the separation L. This is the difference between two infinite quantities. So we introduce a regularization method with cutoff wavelength (frequency) to extract from the difference (infinite) a meaningful finite value. Since metals become transparent to light with very small wavelengths, especially those small compared with an atomic dimension, it is reasonable to have an exponential decay function to limit the contribution to the sum of the vacuum energy for short wavelengths.

Therefore, the subtracted energy with cut-off function $\mathbf{exp}(-\delta\omega_{k_i})$ (Casimir energy) is shown as below:

$$E_{Casimir}(L) = \lim_{\delta \to 0} \frac{\hbar}{2} \int \frac{dk_1 dk_2}{(2\pi)^2} \left( \sum_{n=-\infty}^{n=\infty} \omega_{k_1, k_2, n} e^{-\delta\omega_{k_1, k_2, n}} - 2L \int \frac{dk_3}{2\pi} \omega_k e^{-\delta\omega_k} \right) A = -\frac{c\hbar\pi^2}{720 z^3} A$$

The Casimir force per unit area (Casimir pressure) is given as:

$$F(a) = -\frac{\partial E_{Casimir}(L)}{\partial Z} = -\frac{\pi^2 \hbar c}{240 Z^4} \qquad (1\text{-}7)$$

which is finite and is independent of the cutoff frequency. It is worth noting that eq. (1-7) only relates the fundamental constants $\hbar$ and c (without electron charge e) which implies that real light (electromagnetic field) does not couple to matter in the ordinary sense through the charge, in the case of ideal metal plates. It worth to note that Dirichlet and Neumann boundary conditions are not specific to the EM field

## 1.2 The connection between van der Waals and Casimir forces

Essentially, the Casimir force can be understood in a unified way with van der Waals force[2,3]. The van der Waals force acts between two neutral atoms separated by a distance which is small (smaller than the characteristic absorption wavelength) but much larger than the atomic dimensions (Bohr radius ~0.053nm). It arises in second order perturbation theory from the fluctuating dipole-dipole interaction, i.e. the mean value of the operator of the dipole moment in the ground state is equal to zero but the square of the dipole moment is not. To put it briefly, the origin of both the van der Waals and Casimir forces is connected with the existence of quantum fluctuations[4]. Usually, we refer to them as dispersion forces.

Considering large distances (larger than the characteristic absorption wavelength) between two atoms or two macro objects, we need to take retardation effects into account. In this regime, dispersion forces are called Casimir-Polder force (atom-atom) or Casimir force[1] (micro size boundary conditions). However, eq. (1-4) is universal at any separation distance. They do not change back to the non-relativistic dispersion forces at short distances. It leads to the idea that there are two different kinds of forces rather than two limiting cases of a single physical phenomenon. The result motivated Lifshitz[5] to develop a unified theory between those two forces in the case of two parallel dielectric plates. Lifshitz's theory not only provides all the results of Casimir, Casimir-Polder and van der Waals[4] forces in their respective limits of applicability, but also produces smooth transitions between them.

In this theory, the plate materials are considered as continuous described by the frequency-dependent dielectric permittivity $\varepsilon(\omega)$ and characterized by zero point energy fluctuation of the electromagnetic field. Lifshitz's theory has found many applications [2,6] in the investigation of Casimir forces. Lifshitz's theory related to real materials will be discussed more in the Chapter 2. In the following section, the importance of modern experiments will be presented.

## 1.3 Application of Casimir effect in multidisciplinary field

Precise investigation of Casimir force has powerful impact on multidisciplinary areas, such as the fields of particle physics, atomic physics, astrophysics, mathematical physics[6-8], condensed matter and biophysics. Besides the impact on fundamental physics, the applications in MEMS or NEMS[9] (nano-electromechanical systems) are worth emphasizing.

### 1.3.1 Fundamental physics

**Astrophysics** - Casimir-type polarization of vacuum is important in cosmic string theory used to describe the early Universe before the Big Bang.

**Atomic Physics**- Casimir effect helps us to understand the atom-atom and atom-wall interaction and absorption of atoms by nano structures.

**Particle physics** - The understanding of the Casimir energy of quarks and gluons can help us to realize the hadron masses and provides an effective mechanism for understanding extra spatial dimensions[7]. Also, the Casimir effect has been actively used for obtaining stronger constraints on hypothetical long-range interactions[10,11].

**Mathematical physics** - The derivation of the Casimir effect has inspired scientists to develop powerful regularization methods based on the zeta function and the heat kernel expansion.

**Condensed mater physics** – The Casimir force leads to the investigation of various properties of thin films, surface tension, colloids, and adhesion of microelements. It also plays a role in bulk phenomena such as by modifying the free carrier density in semiconductor which in turn can tune the scale of the Casimir force[12,13].

## 1.3.2 Application in Micro- and nano-technology

Although the Casimir force is too small to be observed for plate-plate at very large separation distances, it becomes very strong in the micro- or nano- scales. At separations of 10nm the Casimir effect produces the equivalent of 1 atmosphere of pressure as shown in figure 1-2. The Casimir force is an obviously dominant force compared to the electrical force at 10nm as shown by the red dash line. Most of MEMS or NEMS devices are actuated or affected by the electrostatic force.

These devices, therefore, are likely to have coupled effect of electrostatic and Casimir forces[14]. The combined action can cause non-linear[15] and bi-stable phenomena[16] and even lead to device failure as shown in figure 1-3 by such effects as abrupt "pull-in"[9]of the moving elements.

Thus, the modification of the Casimir force by changing parameters of materials, rather than the separation is a very important project to investigate. It should be noted that researchers from MIT[17] have developed new tools for calculating the effects of Casimir forces which are useful for MEMS design to keep micro-machines from sticking together. Other than the Casimir force reduction, the force itself can switch the sign from the attractive to repulsive force because of its unique shape dependence. It makes the Casimir force a potential candidate for making frictionless devices[18].

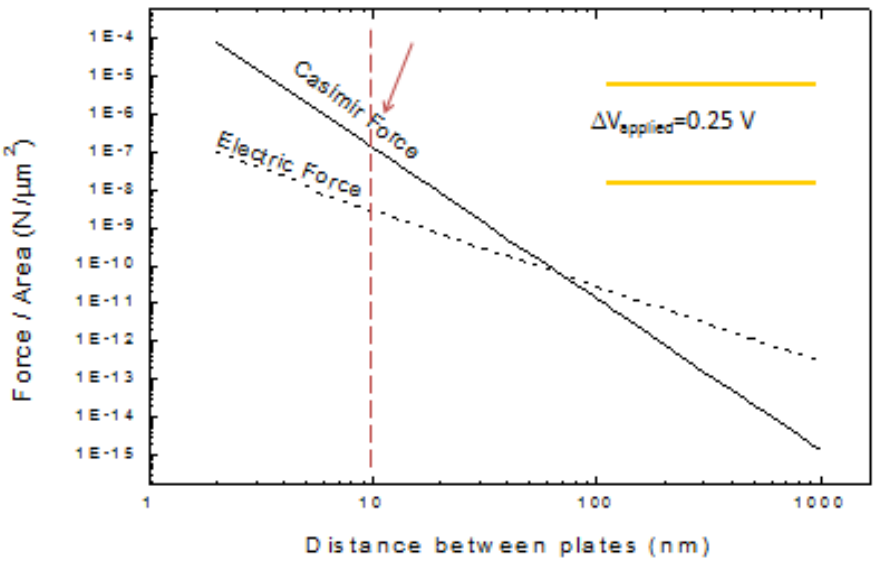


Figure1- 2 Casimir force compared to electrostatic force with a potential difference of 0.25V for two parallel plates as a function of separation distance.

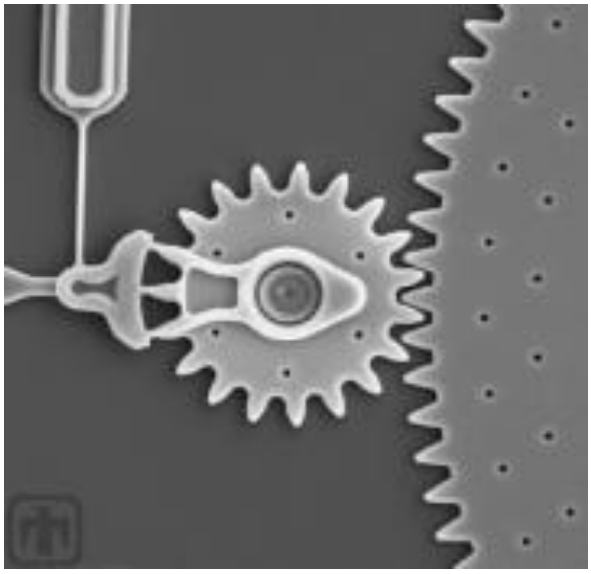

Figure1- 3 The MEMS device might stick together by Casimir force (pull-in effect). Image download from Sandia National Laboratories. .

## 1.4 Review of Casimir force experiments

In the past 50 years since the prediction of Casimir effect, science and technology for Casimir force measurement have progressed tremendously. The first attempt was undertaken by Sparnaay[19] using the spring balance in the separation range of 0.5um~5um. Although the force error was 100% error with respect to the theory of Caimir force, it raised interest in Casimir force measurements. In this chapter, in order to clearly and easily compare contributions to Casimir force measurements from various experiments, we present them with tables and diagrams.

| | Research information | Instrumentation |
|---|---|---|
| Sparnaay[19] (1957) | Parallel metal plates in Air (AL,Cr and steel)<br>Force sensitivity ~$10^{-4}$ dyne<br>Measurement Range: 0.5~5 um<br>Systematic error 100% | **Spring balance system** (Figure 1-4)<br>extension of spring was calibrated by capacitive method |
| Blockland & Overbeek (1978) | Measurement type (lens to plate) In Air<br>(Cr coating plate to lens)<br>Measurement Range: 0.1~0.7 um<br>Systematic error ~40 to 50%<br>"First unambiguous Casimir force measurement[6]" | Spring balance system (Figure 1-5)<br>(force measurement)<br>Separation distance calibrated by Schering bridge |
| Lamoreaux et.al (1997) | Au lens to Au plate in vacuum<br>Measurement Range: 0.1~6 um<br>Radius of lens curvature ~15cm<br>Systematic error ~5% at the closest distance | Torsion pendulum system with phase-sensitive circuit (Figure 1-6)<br>static (force )measurement |
| Mohideen et.al[13,20,21]. (1998~ 2009) | Au sphere to plate in vacuum<br>Measurement Range: 60 nm~1 um<br>Radius of sphere ~ 100um<br>Systematic error ~1% at the closest distance | Atomic Force Microscopic (Figure 1-7)<br>static (force )measurement<br>z distance calibrated by interferometry[22] |
| Bressi et.al. (2002) | Chromium plate to plate<br>Measurement Range: 0.5~3 um<br>Radius of sphere ~ 100um | Dynamic measurement<br>(Casimir force gradient measurement)<br>Figure 1-8 |

| | | |
|---|---|---|
| | Systematic error ~15% at the closest distance | |
| Chen et al.<br>Chiu et al.<br>(2002,2008) | First experimental demonstration of lateral Casimir force measurement.<br>Demonstration of Asymmetrical lateral Casimir force | AFM (Figure 1-9)<br>(lateral Casimir force measurement) |
| Decca et al.<br>(2003,2007) | "Most precise measurements so far".<br>Measurement Range: 0.2~5 um<br>Radius of sphere ~ 150um<br>Systematic error ~0.2% at the closest distance | MTO (Figure 1-10)<br>(micro-mechanical torsion oscillator)<br>The oscillator was made by heavily doped poly-silicon plate.<br>static and dynamic measurement |
| Chan et al.<br>(2001,2008) | Au sphere to Silicon rectangular trenches<br>Studied the expected deviation from PFA | MTO (Figure 1-11)<br>(micro-mechanical torsion oscillator)<br>static and dynamic measurement |

Table 1- 1 Tabulation of the primary achievements of a normal Casimir force measurement. Note that some of important experiments such as the Casimir torque, force measurement in liquids and Casimir-Polder force are not shown in this table.

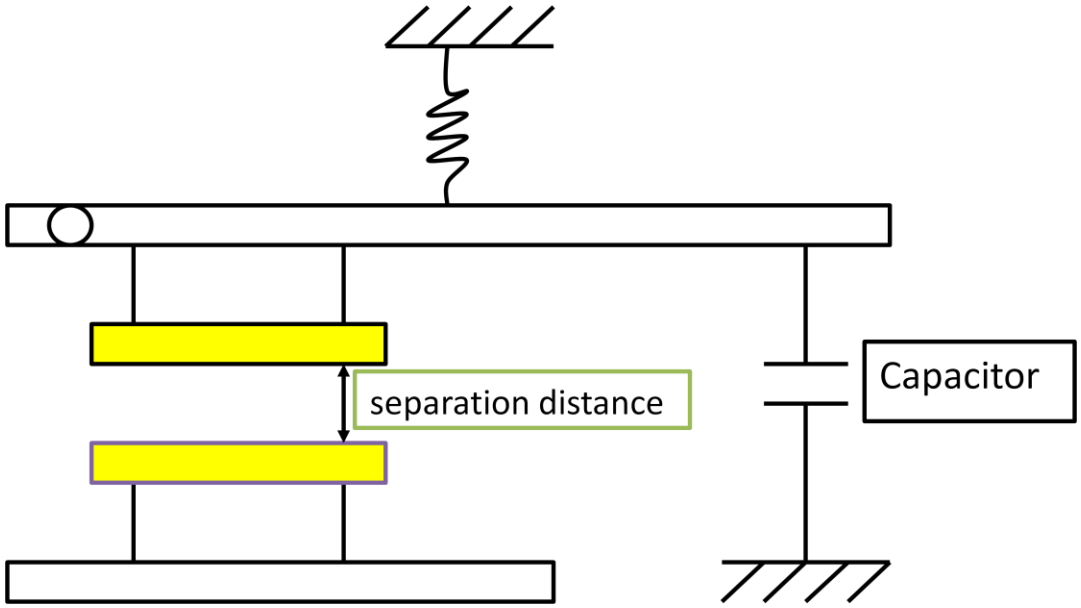


Figure1- 4 shows the simple schematic of the spring balance system used by Sparnaay. The extension of the spring was measured through a measurement of the capacitance between two plates.

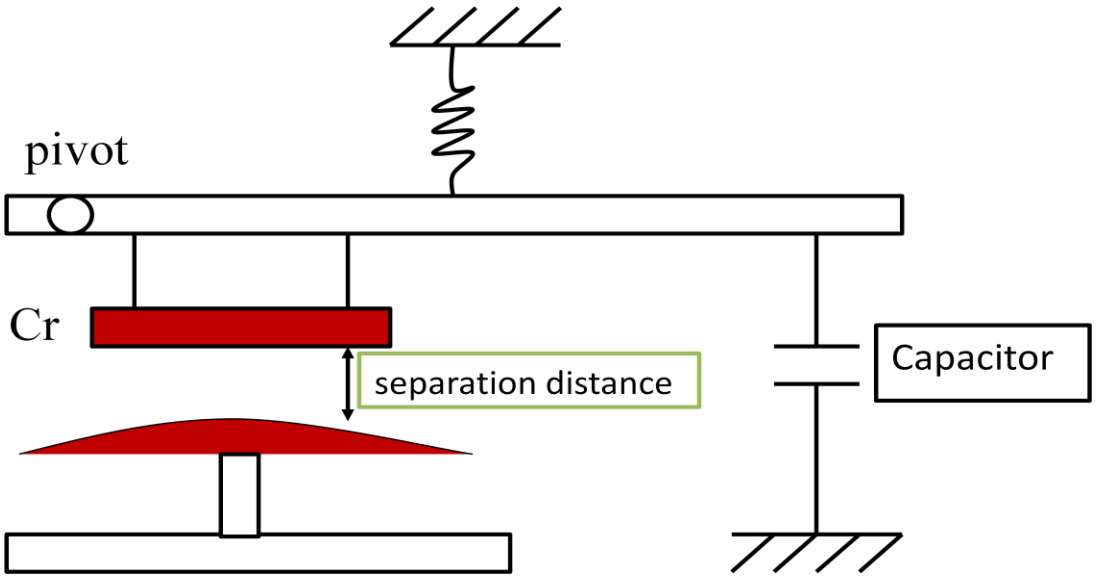


Figure1- 5 Schematic of lens-plate force balance system used by Overbeek et.al

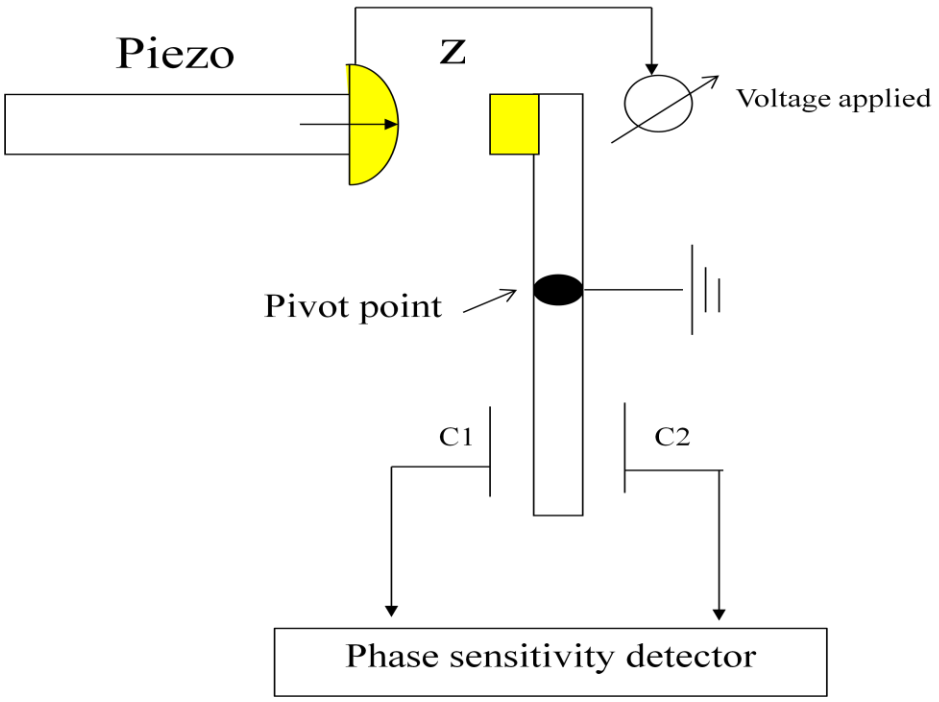


Figure1- 6 Experimental setup of torsion balance pendulum by S.K.Lamoreaux.

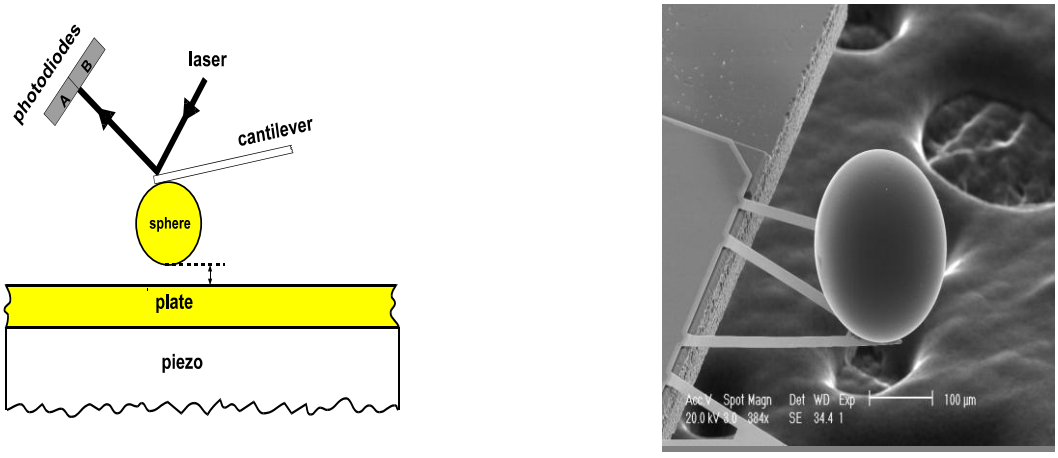


Figure1- 7 The picture on the left shows schematic diagram of Mohideen et al.[20,23] experimental setup. The distance between the bottom of sphere and plate is changed by application of voltage to the piezo. Right hand side picture shows Scanning Electron Microscope image of the metalized sphere on a triangular AFM cantilever.

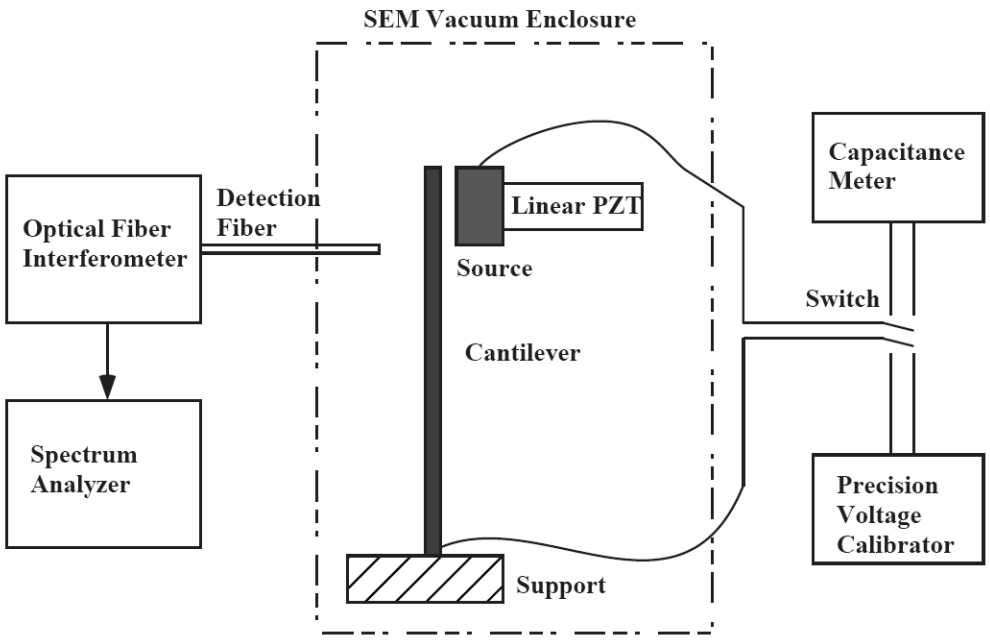


Figure 1- 8 Interferometer-based Vacuum system with FFT spectrum analyzer by Bressi et al[24].

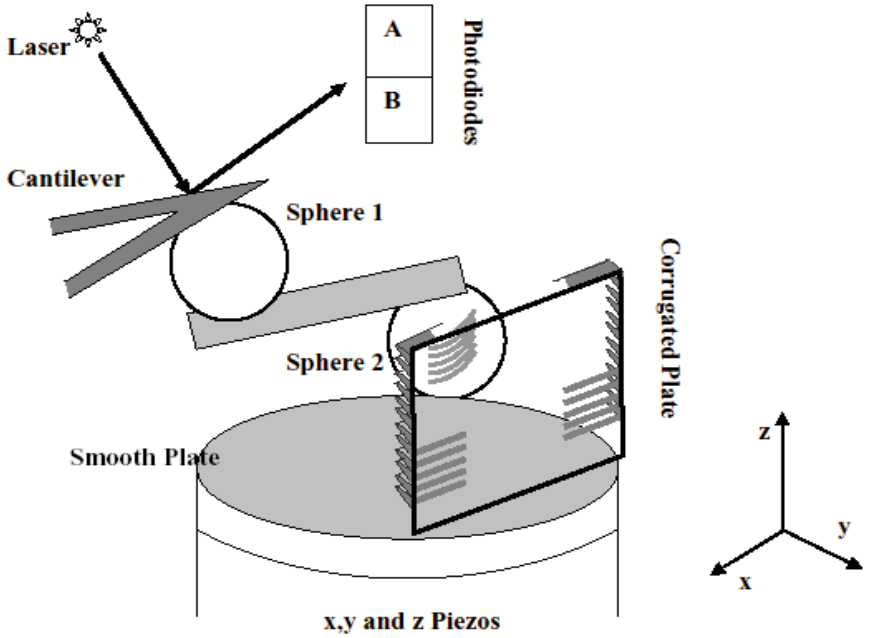


Figure 1- 9 Schematic of the experiment setup of the lateral Casimir force measurement. A modified cantilever was used in vacuum with an AFM.

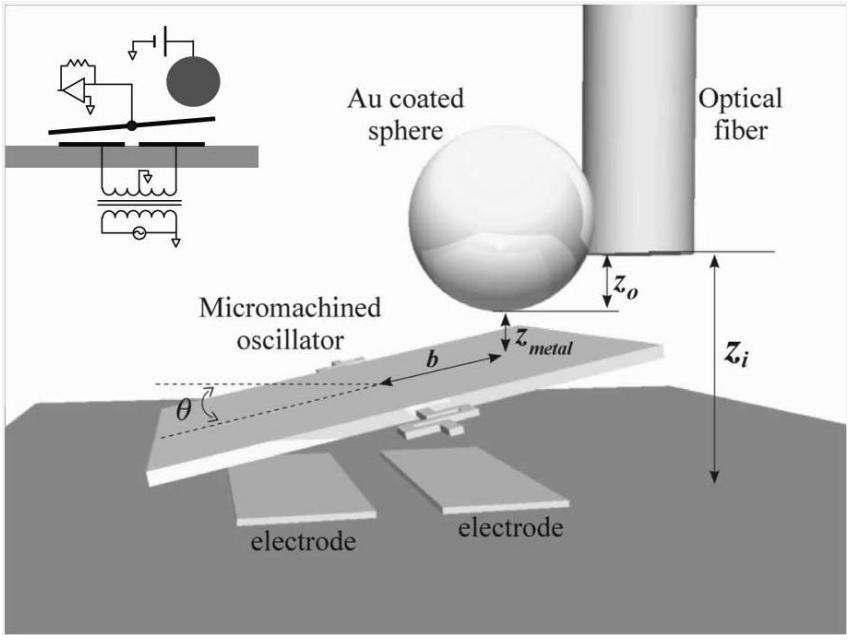


Figure 1- 10 Schematic diagram of the measurement o of the Casimir force using a MTO by Decca et al.2003[25,26] and Chan et al.2001[14]

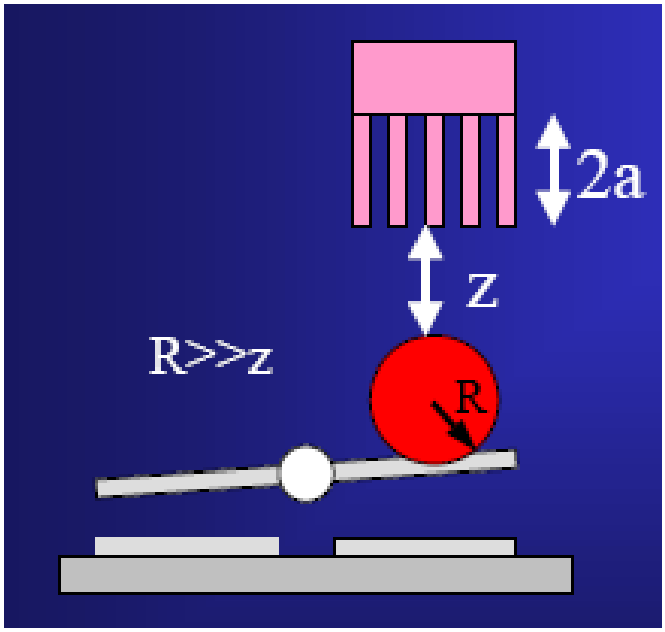


Figure 1- 11 Schematic of the experimental set-up, including the MTO, gold sphere and silicon trench array by Chan et al[27].

### 1.4.1 General requirements for a high precision Casimir force measurement

From the history of development in Casimir force measurement, some fundamental requirements for precision Casimir force measurement are,

(1) Completely clean sample surface.

(2) Precise, independent, and reproducible measurement of separation between two sample surfaces.

(3) Low electrostatic charges.

(4) High force sensitivity system.

## 1.5 Overview

The reminder of this thesis is divided into four sections. The first section (chapter 2) is a review of the theory, addressing the Lifshitz's equations and its applications to ideal materials. Special attention is paid to geometry (approximation methods ) other than planar boundaries. In the middle of this section, corrections to the Casimir force between real materials with temperature, roughness and finite conductivity will be discussed. At the end of chapter 2, the main purpose of this thesis which is a consideration of the Drude, Plasma and generalized Plasma-like model that takes into account inter-band transitions of core electrons in application of Lifshitz equation will be presented.

In chapter 3, the research methodology with full details of the instrumentation (high vacuum short coherence length interferometer) and procedure will be presented. To address the limited force sensitivity, the noise levels of measurement system will be discussed. The next chapter deals with data analysis, i.e. the rigorous procedures for comparison of experiment and theory.

Finally, in the chapter 5, conclusions are presented and suggestions are made for further research.

# Chapter 2. Lifshitz theory for real materials

As we mentioned in chapter 1, Lifshitz developed a more general theory which successfully describes the Van der waals and Casimir force in a unified way. The assumption of Lifshitz theory is based on random fluctuating currents at the surface of material caused by the fluctuation of charges in the medium through Maxwell's equations. Thus, the results from Lifshitz theory depend strongly on the model of dielectric permittivity used to describe real materials. In this chapter, contrary to the ideal case, we will focus on the distinguishing features such as non-zero temperature, surface roughness or finite conductivity of the boundary materials which should be taken into account in order to obtain accurate results. In the final section of this chapter, thermo-dynamical aspects of thermal Casimir force between real metals will be presented.

## 2.1 Lifshitz theory for two parallel dielectric plates

### CASE T=0:

Let us consider the case in which a monochromatic electromagnetic field, eq. (2-1), (2-2), interacts with the dielectric medium as shown in figure 2-1:

$$E(t,r) = E(r)e^{-i\omega t} \qquad (2\text{-}1)$$

$$B(t,r) = B(r)e^{-i\omega t} \qquad (2\text{-}2)$$

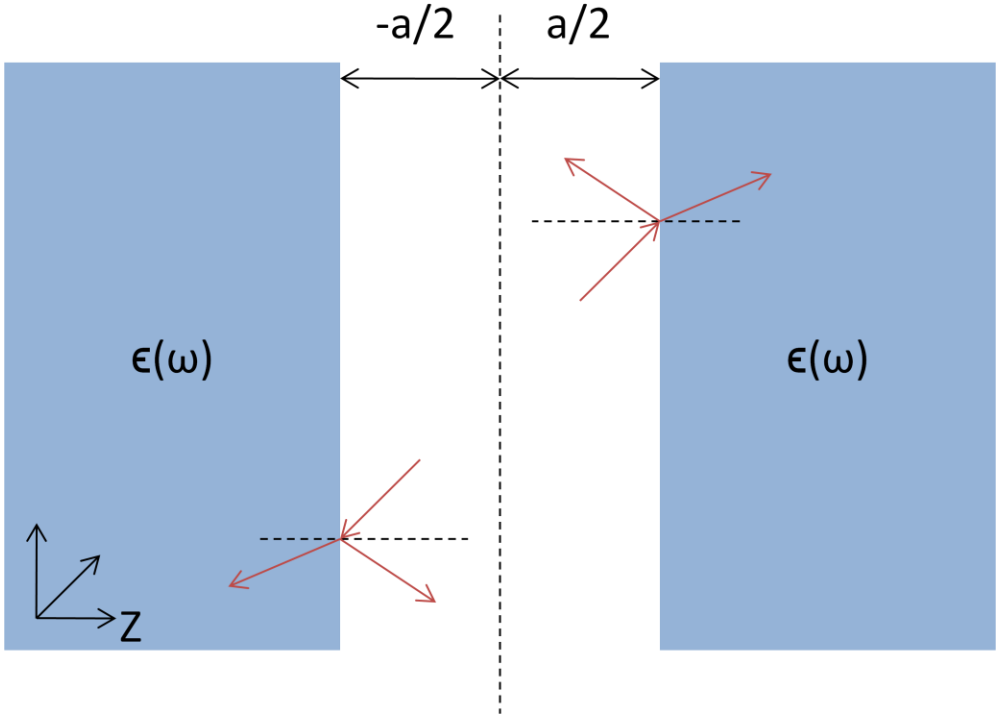


Figure 2- 1 Two plates with the dielectric permittivity ϵ(ω) and reflections of electromagnetic oscillations at the surface given by the boundary conditions.

Considering only non-magnetic materials in the absence of charge and current densities, we obtain equations inside the dielectric plates by substituting the eq.2-1 and 2-2 into Maxwell's equations. The equations are shown below:

$$\nabla \cdot E(r) = 0 \tag{2-3}$$

$$\nabla \times E(r) - i\tfrac{\omega}{c}B(r) = 0 \tag{2-4}$$

$$\nabla \times B(r) + i\varepsilon(\omega)\tfrac{\omega}{c}E(r) = 0 \tag{2-5}$$

$$\nabla \cdot B(r) = 0 \tag{2-6}$$

Now, let us supplement the boundary conditions by using the continuity conditions at the surface separated by distance a/2,

$$E_{1t}(t,r) = E_{2t}(t,r) \tag{2-7}$$

$$D_{1n}(t,r) = E_{2n}(t,r) \tag{2-8}$$

$$B_{1n}(t,r) = B_{2n}(t,r) \tag{2-9}$$

$$B_{1t}(t,r) = B_{2t}(t,r) \tag{2-10}$$

where n and t refer to the normal and tangential component to the boundary plane directed inside the dielectric. D(ω) is the electric displacement which is equal to ε(ω)E(ω). And ε(ω) is the complex dielectric constant of the dielectric.

The solutions of vacuum energy of the electromagnetic field in thermal equilibrium with the dielectric plates at zero temperature is given by (in terms of un-known photon eigen-frequencies)

$$E_0(a) = \frac{\hbar}{4\pi}\int_0^\infty k_\perp dk_\perp \sum_n (\omega_{k\perp,n}^{TM} + \omega_{k\perp,n}^{TE})A \tag{2-11}$$

where the TE and TM are represent the transverse electric mode and transverse magnetic mode and$k_\perp = (k_x, k_y)$ ,respectively. Using the regularization method mentioned in Chapter1, the finite Casimir energy per unit area of the boundary planes is

$$E(a) = \frac{E_0(a)}{A}$$

By using the explicit expressions shown below

$$q^2 = q^2(i\xi, k_\perp),\ k^2 = k^2(i\xi, k_\perp), \qquad (2\text{-}13)$$

We arrive at the Lifshitz formula at zero temperature,

$$E_0(a) = \frac{\hbar}{4\pi}\int_0^\infty k_\perp dk_\perp \int_0^\infty d\xi \{\ln[1 - r_{TM}^2(i\xi, k_\perp)e^{-2qa}] + \ln[1 - r_{TE}^2(i\xi, k_\perp)e^{-2qa}]\} \qquad (2\text{-}14)$$

Hence, the Lifshitz formula for the Casimir pressure is

$$\mathrm{P}(a) = -\frac{\partial \mathrm{E(a)}}{\partial \mathrm{a}}$$

$$= \frac{\hbar}{4\pi}\int_0^\infty k_\perp dk_\perp \int_0^\infty d\xi \{[r_{TM}^{-2}(i\xi, k_\perp)e^{-2qa} - 1]^{-1} + [r_{TE}^{-2}(i\xi, k_\perp)e^{-2qa} - 1]^{-1}\} \qquad (2\text{-}15)$$

From the derivation of Lifshitz theory, we know the electrical and optical properties of real materials will have to be accounted for, to provide a consistent theory of the Casimir force.

## CASE T≠0:

The Lifshitz equation for the dispersion force takes into account not only fluctuations of zero point energy but also thermal photons when the material of the plates is in thermal equilibrium at non-zero temperature T. Therefore, the final equation of the free energy

and pressure in terms of the two independent polarizations of the electromagnetic field and Matsubara frequencies$\xi_l$, ($\xi_l = 2\pi \frac{k_B T}{\hbar} l$) are presented as eq.2-16 and eq. 2-17.

$$E_0(a,T) = \frac{\mathrm{k_B T}}{2\pi} \sum_{\mathrm{l}=0}^{\infty}{}' \int_0^{\infty} k_\perp dk_\perp \{\ln[1 - r_{TM}^2(i\xi_l, k_\perp)e^{-2qa}] + \ln[1 - r_{TE}^2(i\xi, k_\perp)e^{-2qa}]\}$$

(2-16)

$$\mathrm{P(a,T)} = \frac{-\mathrm{k_B T}}{\pi} \sum_{\mathrm{l}=0}^{\infty}{}' \int_0^{\infty} \mathrm{q} k_\perp dk_\perp \{[r_{TM}^{-2}(i\xi, k_\perp)e^{-2qa} - 1]^{-1} + [r_{TE}^{-2}(i\xi, k_\perp)e^{-2qa} - 1]^{-1}\}$$

(2-17)

where the prime on the summation sign means that the term for l=0 has to be multiplied by ½ . The expressions for the reflection coefficients at the Matsubara frequencies are

$$r_{TM}(i\xi, k_\perp) = \frac{\varepsilon_l q_l - k_l}{\varepsilon_l q_l + k_l}, \quad r_{TE}(i\xi, k_\perp) = \frac{q_l - k_l}{q_l + k_l}, \qquad (2\text{-}18)$$

$where,\ q_l^2 = k_\perp^2 + \frac{\xi_l^2}{c^2}\ ,\ k_l^2 = k_\perp^2 + \varepsilon_l \frac{\xi_l^2}{c^2}, \varepsilon_l = \varepsilon(i\xi_l)$ . Bearing in mind; Eq. (2-18) represents the standard reflection coefficients which are usually real, this is along the imaginary axis. It is worth pointing out again that the Lifshitz theory applied in real materials is obtained by the solution of one-dimensional scattering on the axis perpendicular to the plates. Thus, the scattering method leading to eq.2-16, has the definite solution under the condition that

$$\lim_{\xi\to\infty}\xi^2\varepsilon(i\xi) = constant \neq 0 \qquad (2-19)$$

## Temperature correction

Note that the representation of equations 2-16 and 2-17 for the finite temperature Casimir force has a disadvantage as the l=0 term is the product of zero by divergent integral. Because of this, the representation of eq. 2-14 is preferable as compared eq. 2-16. Thus, let us apply eq.2-14 to ideal metals of infinitely high conductivity in order to find the temperature correction to the Casimir energy between ideal metals. One should take limit $\varepsilon \to \infty$ before setting l=0 (Schwinger prescription).

The expression of Casimir force can be presented as a function of the Casimir force at zero temperature and temperature correction terms.

$$\mathrm{P(a,T)} = P(a,0)\{1 + \frac{30}{\pi^3}\sum_{\mathrm{n=1}}^{\infty}[\left(\frac{\mathrm{T}}{\mathrm{T_{eff}}}\right)^4\frac{1}{\mathrm{n^4}} - \pi^3\frac{\mathrm{T}}{\mathrm{T_{eff}}}\frac{1}{\mathrm{n}}\cosh\left(\pi\mathrm{n}\frac{\mathrm{T}}{\mathrm{T_{eff}}}\right)\sinh^{-3}\left(\pi\mathrm{n}\frac{\mathrm{T}}{\mathrm{T_{eff}}}\right)]\} \quad (2\text{-}20)$$

where the effective temperature is defined as $k_B T_{eff} = \frac{\hbar C}{2a}$.

**Low temperature limit:** ($T \ll T_{eff}$), it follows from eq. 2-20 $\mathrm{P(a,T)} \cong$

$$P(a,0)[1+\frac{1}{3}\left(\frac{\mathrm{T}}{\mathrm{T_{eff}}}\right)^4] \qquad (2\text{-}21)$$

From eq. 2-19, we could estimate the error from the temperature correction ~0.15% for T=300K and separation distance a~1um.

**High temperature limit:** ($T \ll T_{eff}$),

$$\mathrm{P(a,T)} \cong \frac{\mathrm{k_B T}}{4\pi \mathrm{a}^3}\xi_{\mathrm{R}}(3) \qquad (2\text{-}22)$$

Where $\xi_{\mathrm{R}}(3)$ is the Riemann zeta function and $\xi_{\mathrm{R}}(3) \sim 1.202$. In comparing with these two temperature terms eq. 2-21 and 2-22, we know the corrections to the original Casimir force at short separations are negligibly small. Contrary to the low temperature limit, if the separation "a" is about a few micrometers or in the higher temperature region, the corrections become large. For example, at a room temperature of 300K and plate separations larger than 6um, the total Casimir pressure is already equal to the thermal term (behavior as classical limit determined by thermal photons) as mentioned in eq. 2-22.

## Finite conductivity correction (skin depth correction)

To calculate the Casimir force between real dielectric materials, we need to correct for the frequency as a function of permittivity. In contrast to dielectrics, metals have a non-zero conductivity which comes from free electrons at zero temperature. Compared to

perfect metals, in real metals we need to take the penetration depth (skin depth) of an electromagnetic wave into account. Considering the penetration depth, intuitively, the real separation distance could be treated as larger than real distance. Thus, the force is smaller compare to the real value. Essentially, the skin depth is presented as the function of plasma frequency depending on the property of the metal. Thus, in this section, we will study the effect of the skin depth using the plasma model.

Based on the characteristic frequency $\xi \sim \frac{c}{2a}$ (optical region from visible to infrared), it is reasonable to consider separation distances from 100nm to 1.5um. As mentioned in the previous section, the thermal correction is negligibly small. We can assume the temperature is effectively equal to zero. A good approximation for the dielectric permittivity of metals is represented by the free electron plasma model $\varepsilon(\omega) = 1 - \frac{\omega_p^2}{\omega^2}$, and $\omega_p^2 = \frac{4\pi N e^2}{m^*}$ where $\omega_p$ is the plasma frequency. N is the density of conduction electrons. $m^*$ is their effective mass. The skin depth is $\delta_0 = \frac{\lambda_p}{2\pi}$ is given by the plasma wavelength$\lambda_p$. In terms of the dielectric permittivity along the imaginary frequency axis $\varepsilon(i\xi) = 1 + \frac{\omega_p^2}{\xi^2}$, the final Casimir energy with a finite correction term is

$$E_{pp}(a) = E^{T=0}(a)\left[1 - 4\frac{\delta_0}{a} + \frac{72}{5}\frac{\delta_0^2}{a^2} - \frac{320}{7}\left(1 - \frac{\pi^2}{210}\right)\frac{\delta_0^3}{a^3} + \frac{400}{3}\left(1 - \frac{163\pi^2}{7350}\right)\frac{\delta_0^4}{a^4}\right]$$

(2-23)

,where the subscript “p” indicates the plasma model and E (a) is Casimir energy for ideal metals.

$$F_{pp}^{caimir}(a) = F_{pp}^{T=0}(a)[1 - \frac{16}{3}\left(\frac{\delta_0}{a}\right) + 24\left(\frac{\delta_0}{a}\right)^2 - \frac{640}{7}\left(1 - \frac{\pi^2}{210}\right)\left(\frac{\delta_0}{a}\right)^3 + \frac{2800}{79}\left(1 - \frac{163\pi^2}{7350}\right)\left(\frac{\delta_0}{a}\right)^4$$

(2-24)

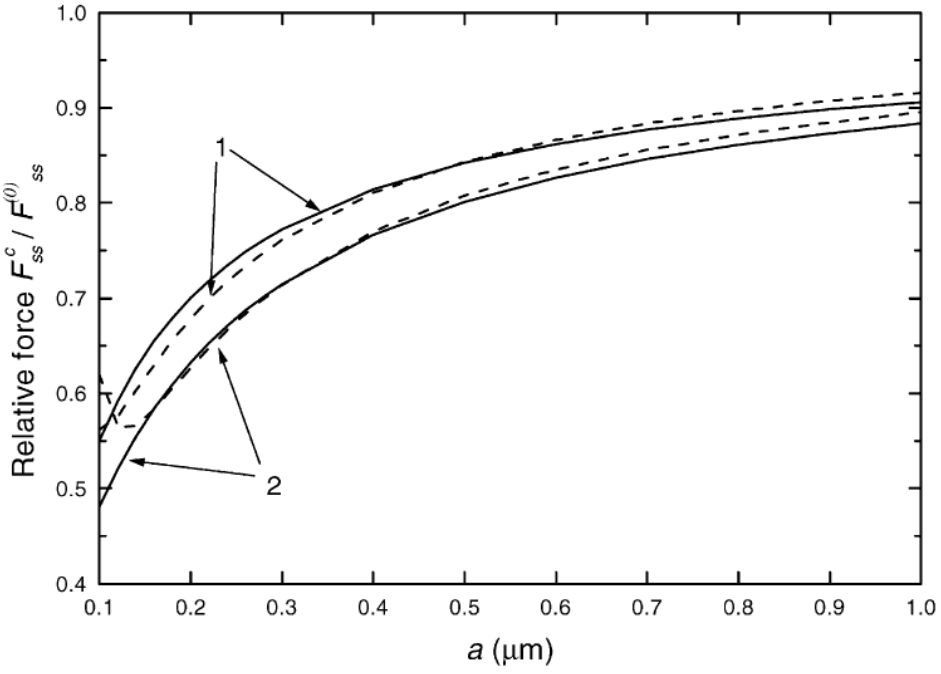


[28]Figure 2- 2 The ratio of the correction due to the finite conductivity of metal. The solid line 1 and 2 represent the computational results for Al and Au, respectively. The dashed lines 1 and 2 represent the correction factor up to the fourth order for the same material as eq2-24.

## Roughness correction[29]:

The surface of real bodies always has small deviations from perfect geometry. In the theory, so far, we discussed, dispersion force are determined by the reflection of electromagnetic waves from the surface. Thus, reflecting processes on rough surfaces become important for corrections to the Casimir force resulting from surface roughness. Here, we apply the method of PWS, (pair-wise summation), to calculate the roughness corrections to Casimir force between real material bodies.

As depicted in figure 2-3 , we consider two parallel plates of thickness D with sides of length 2L with surface roughness. Assuming the separation distance between the plates is sufficiently large and roughness is extremely irregular, the descriptions of roughness could be presented by the stochastic function as below:

$$z_1 = A_1 f_1(x, y) \tag{2-25}$$

$$z_2 = a + A_2 f_2(x, y) \tag{2-26}$$

where a is the mean separation distance as shown in figure 2. The $A_1$ and $A_2$ are amplitude of the roughness function which is defined as $\max|f_i(x, y)| = 1$. Here, we introduce the Casimir energy by PWS[30] (the interaction energy between two bodies can be obtained as an integral of the inter-atomic potentials over the volumes of both bodies).

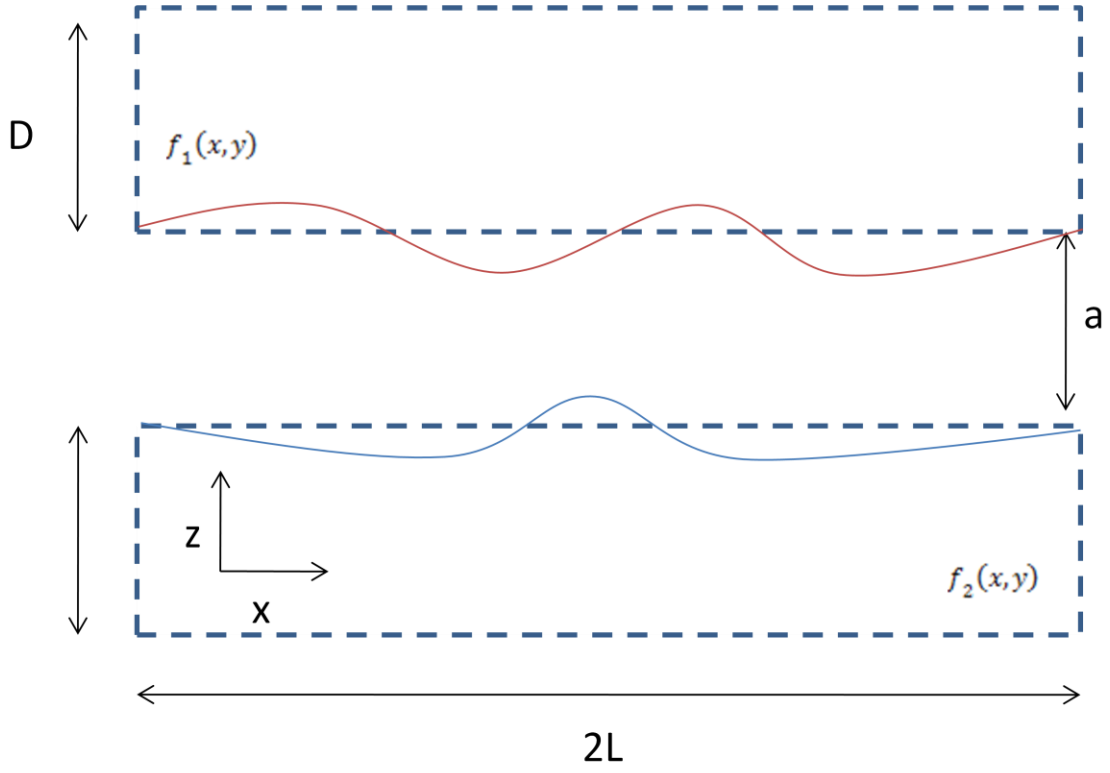


[31]Figure 2- 3 presents two parallel plates with rough surfaces. $f_i(x,y)$ indicates the stochastic roughness function.

The total Casimir energy between two rough surfaces is

$$E^{add}_{casimir}(a) = U(r,\varepsilon)\int_a dx_1 \int_a dy_1 \int_a dx_2 \int_a y_2 \int_{-D}^{z_1} dz_1 \int_{z_2}^{L+D} dz_2 \, |r_1 - r_2|^{-7}$$

where $U(r,\varepsilon)$ is potential energy in-between two bodies. The Casimir force between the plates is given by

$$F_{PP}^{Rough}(a) = F_{PP}^{0}(a)\{1 + 10\left[\left(\frac{\delta_1}{a}\right)^2 + \left(\frac{\delta_2}{a}\right)^2\right] + 105\left[\left(\frac{\delta_1}{a}\right)^2 + \left(\frac{\delta_2}{a}\right)^2\right]\} \qquad (2\text{-}27)$$

For example, as is the usual case, the respective amplitude of the stochastic roughness is around 1.2nm in our previous static experiment. It introduces effective corrections of ~0.22% at the shortest distance of around 100 nm.

# 2.2Thermal Casimir Force: calculations and controversy

## In Metals

Conceptually, the Lifshitz theory for the Casimir Force at any temperature provides a way for obtaining all the necessary results for any real metal. To precisely calculate thermal Casimir force between two real metal plates, the correct permittivity $\varepsilon(\omega)$ related to the dielectric properties of material is needed. For the UV, optical and infrared region, tabulated data is available for most materials. However for the low frequency, the dielectric permittivity is described by either the Plasma or Drude models..

There is at present unresolved controversy of whether the Plasma or Drude is more appropriate for presenting permittivity $\varepsilon(\omega)$ in the thermal Casimir force calculation.[32]. Note that the Casimir energy given by the Lifshitz theory depends strongly on the model for the different dielectric functions we choose, as shown in picture below.

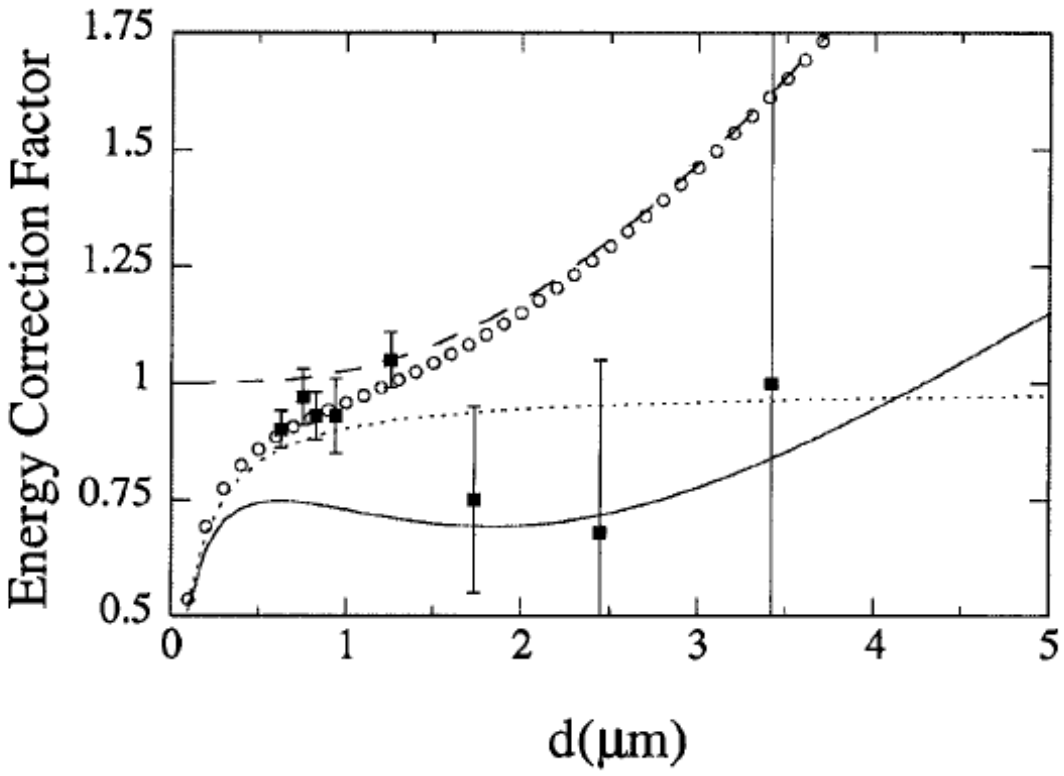


Figure 2- 4 The energy correction factor for Au in different temperature (thermal corrections) and different dielectric models (Plasma and Drude corrections). The dashed line is the thermal correction (300K) for ideal metal plates. The thermal correction factor with Plasma or Drude model is shown by the open circles and solid line, respectively. The dotted line indicates the plasma model correction at zero temperature. The solid square with error bar is experimental data from Lamoreaux 1997.

In the Plasma model, the dependence of dielectric function on the frequency is given by $\varepsilon_p(\omega) = 1 - \frac{\omega_p^2}{\omega^2}$ along the real frequency axis or by $\varepsilon_p(i\xi) = 1 + \frac{\omega_p^2}{\xi^2}$ along the imaginary frequency axis. This dielectric permittivity is applicable in the frequency region of infrared optics. At 300K, all non-zero Matsubara frequencies are located in this frequency region. It leads more accurate results for the Casimir force when separation distance is above the plasma wavelength due to penetrate depth. The generalized Plasma-

like model is similar to Plasma model but it includes the role of the core electrons which are modeled by Lorentz oscillators. Compared to the Plasma model, the generalized Plasma-like model can be applied even for short separation distances between the plates. To answer whether the Plasma model is appropriate to Lifshitz theory of thermal Casimir forces, we need to find the asymptotic expression for the Casimir free energy given by the Plasma model. As defined in the section "temperature correction", the low temperature asymptotic expression for Casimir energy given by Plasma model is

$$\Delta_T E^{Plasma}(a,T) = \mathrm{E}_{\mathrm{pp}}^{\mathrm{T}=0}\left\{1+\frac{45\xi(3)}{\pi^3}\left(\frac{\mathrm{T}}{\mathrm{T}_{\mathrm{eff}}}\right)^3-\left(\frac{\mathrm{T}}{\mathrm{T}_{\mathrm{eff}}}\right)^4+\frac{2\mathrm{c}}{\omega_{\mathrm{p}}\mathrm{a}}\left[\frac{45\xi(3)}{\pi^3}\left(\frac{\mathrm{T}}{\mathrm{T}_{\mathrm{eff}}}\right)^3-\left(\frac{\mathrm{T}}{\mathrm{T}_{\mathrm{eff}}}\right)^4\right]+\ldots\right\} \quad (2\text{-}28)$$

Thus, the corresponding Casimir entropy is presented as below.

$$\mathrm{S}(\mathrm{a},\mathrm{T}) = -\frac{\partial\Delta_T E^{Plasma}(a,T)}{\partial \mathrm{T}} = \frac{-k_B T\xi_R(3)}{8\pi a^2}\left(\frac{\mathrm{T}}{\mathrm{T}_{\mathrm{eff}}}\right)^2\left\{1-\frac{\pi^3}{45\xi(3)}\frac{\mathrm{T}}{\mathrm{T}_{\mathrm{eff}}}+\frac{2\mathrm{c}}{\omega_{\mathrm{p}}\mathrm{a}}\left[1-\frac{\pi^3}{45\xi(3)}\frac{\mathrm{T}}{\mathrm{T}_{\mathrm{eff}}}\right]\right\} \quad (2\text{-}29)$$

As can be seen in above equation, the thermal Casimir entropy goes to zero when the temperature goes to absolute zero. This means that the third law of thermodynamics is satisfied. It is worth noting that the Casimir entropy using the plasma model is positive as shown in figure2-5 at all temperatures which is different from the Drude model as shown in the following section.

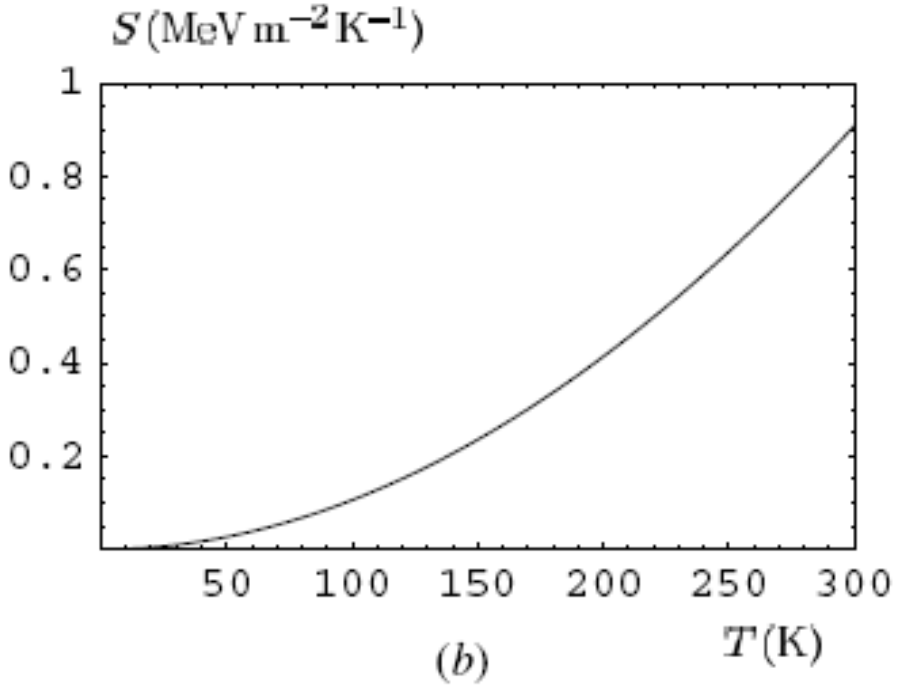


Figure 2- 5 The Casimir entropy per unit area versus temperature at a separation a=300nm given by plasma model ($\omega_p$=9.0 ev)[33].

The Drude model provides a proper an alternative low-frequency description for metals in condensed matter physics and the dielectric permittivity, $\varepsilon_D(\omega) = 1 - \frac{\omega_p^2}{\omega(\omega+i\gamma(T))}$ depends on $\omega^{-1}$, where the $\gamma(T)$ is the relaxation parameter (Drude dielectric function along the imaginary frequency axis is $\varepsilon_D(i\xi) = 1 + \frac{\omega_p^2}{\xi(\xi+\gamma(T))}$). Actually, the first violation of Lifshitz equation is evident. According to the eq. (2-19), dielectric function must approach a constant value (the static permittivity) when the $\xi$ goes 0. The second problem, concern the value of the reflection coefficients (eq.2-17) from TM and TE mode at zero frequency are

$$r_{TM}(0,k_\perp)=1, r_{TE}(0,k_\perp)=0$$

For example, if we substitute eq. 2-25 into thermal casimir energy and pressure eq.2-15 2-16, we obtain asymptotic expressions as given by Drude model,

$$E_{Drude}(a,T)=\frac{-k_BT}{16\pi a^2}\xi_R(3), \qquad P_{Drude}(a,T)=\frac{-k_BT}{8\pi a^3}\xi_R(3)$$

Those expressions are equal to one-half value of the corresponding value for ideal metal plates regardless of how large a conductivity is used for the real metal. The result is counter-intuitive because the conductivity does not play any role in this approach.

The other important issue is the violation of third law of thermodynamics for the Drude model. Recalling the temperature correction, the Casimir energy for the Drude model at low-temperature limit can be presented in the form[29,34]:

$$\Delta_T E^{Drude}(a,T)=\Delta_T E^{Plasma}(a,T)+E^{\gamma}(a,T)-$$

$$\frac{k_BT}{16\pi a^2}\int_0^{\infty} ydy\times ln[1-\left(\frac{cy-\sqrt{4a^2{\omega_p}^2+c^2y^2}}{cy+\sqrt{4a^2{\omega_p}^2+c^2y^2}}\right)^2 e^{-y}]$$

where $\Delta_T E^{Plasma}(a,T)$ is the low temperature asymptotic expression for the Casimir energy given by the plasma model. The second term is the contribution to Drude free energy, $E^{\gamma}(a,T)=\gamma(T)\ln\left(\frac{T}{T_{eff}}\right)$, and depends on the relaxation parameter $\gamma(T)$ given by Drude model. Therefore, the Casimir entropy is given by

$$S(a,0) = -\frac{\partial E(a,0)}{\partial T} = \frac{k_B}{16\pi a^2}\int_0^\infty ydy \times ln[1 - \left(\frac{cy - \sqrt{4a^2{\omega_p}^2 + c^2y^2}}{cy + \sqrt{4a^2{\omega_p}^2 + c^2y^2}}\right)^2 e^{-y}]$$

$$= \frac{-k_{B\xi(3)}}{16\pi a^2}\left(1 - \frac{4c}{\omega_p a} + 12\left(\frac{c}{\omega_p a}\right)^2 - \cdots\right) < 0$$

where $-\frac{\partial E^{\gamma}(a,0)}{\partial T} = 0$, because $\gamma(T)$ is proportional to $T^2$ and the entropy given by plasma model goes to zero when T vanishes.

From the above equation, the Casimir entropy for perfect crystal lattice metal calculated by the Drude model at zero temperature is equal to a non-zero negative value as shown in figure 5. This value depends on parameters such as the plasma frequency, and the separation distance. According to the third law of thermodynamics (the Nernst heat theorem), ***as a system temperature approaches the absolute zero, the entropy of the system approaches a minimum value***. Therefore, Drude model combined with Lifshitz equation violates the third law of thermodynamics.

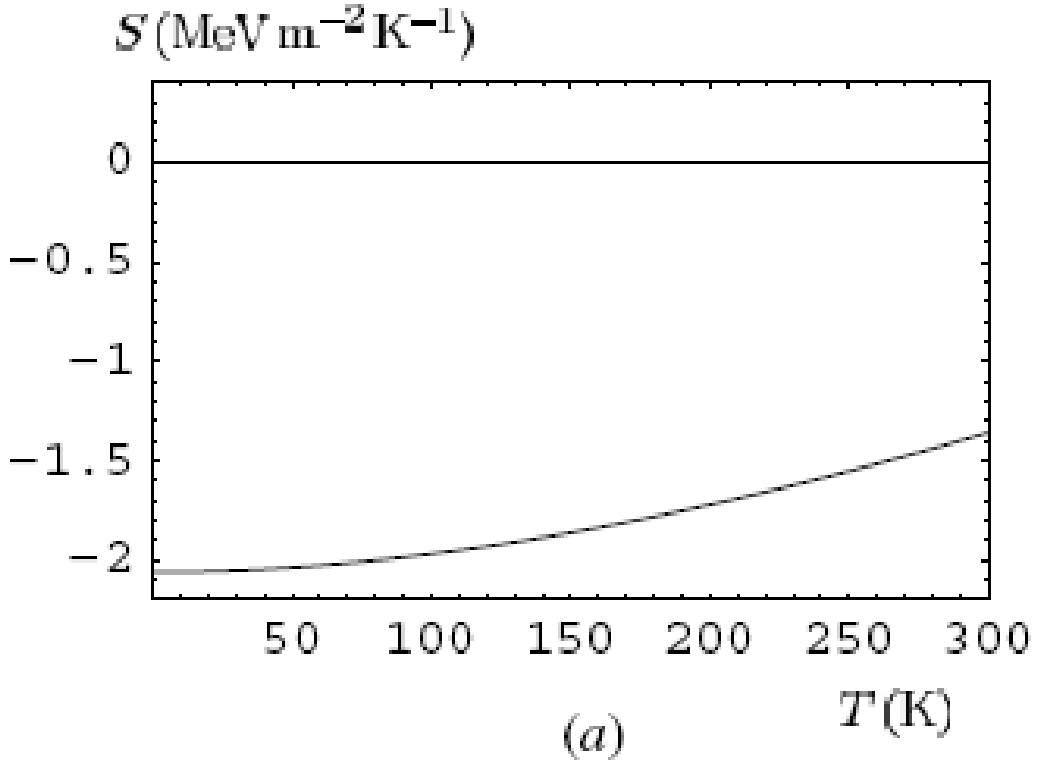


Figure 2- 6 [33]The Casimir entropy per unit area as function of temperature at a separation 1um is given by Drude model

To sum up, thermodynamics helps us make a decision regarding which model is in accordance with fundamental physical principles. Lifshitz theory combined with Plasma model is thermodynamically consistent. In condensed matter field, Plasma model does not take free electron dissipation into account and is applicable in the frequency region of infrared optics. Unlike plasma, Drude model is the self-consistent solution of Maxwell equations with the real current of conduction electrons. These real current (DC current) which involves electric resistance and heating of a metals created by real electromagnetic fields are better explained by the Drude model. In the infrared region

frequencies are too high to cause real current. Since for the separation regions of interest to the experiment, the infrared and visible frequencies are more important, the plasma model might be more applicable. Or the neglect of dissipation in the Drude model might be necessary when dealing with virtual photons.

# Chapter 3. Instrumentation and experimental method

## 3.1 Introduction[35]

A scanning force microscope is usually used to detect small forces or force gradients. In our case, we are doing measurements of Casimir effect between a 100 micron size sphere and plane sample surface. In order to reach high precision, we must pay more attention to the sensitivity of the detection system. Our detection system consists of a cantilever with attached micro-sphere, piezoelectric actuator, fiber interferometer including pre-amplifier, light source and electronic frequency modulation controller, phase detector, voltage amplifiers, etc. Each of them contributes phase noise to the detecting system. The ultimate sensitivity of system is determined by the ratio between signal (frequency shift) and the total noise level. Apart from noise sources listed above, there are external noise sources such as vibrations from environment, 1/f low frequency noise level or acoustic noise. With a carefully designed the system, the amplitude of the passive cantilever approaches the thermal noise limited amplitude. In this chapter, we will focus on the principles of force microscopy including up-to-date measurement techniques, including theoretical considerations of cantilever-based force or force gradient measurements.

We will discuss the contribution of each noise source in my system and also the theoretical consideration of noise limited minimum detectable force gradient. In the last part of this chapter, the standard experimental method will be presented.

## 3.2 Review of Measurement techniques

Currently, there are some unique techniques for detecting motion of the sensor (micro-sized cantilever). Each of techniques have their advantages and disadvantage with respect to sensitivity, low-frequency stability and complexity. At micron scales, for example, SPM (Scanning probe microscopies) and MEMS, their readout system are usually optical or capacitance based, respectively. However, when the size of system goes to the nano scale, usually the piezo-based detection is the favored way because of its low noise level.

### Piezo-based detection[36]

The effect was first discovered by Lord Kelvin in 1856 who noted that the resistance of copper and iron wires increased when in tension. The basic idea is that a sensor patterned from piezoresistive material, affixed to moving parts of a mechanical device undergoes a resistance change due to the motion-induced strain. On biasing with a current source, the piezoresistor translates the strain into voltage signal. The merit of this method is that it does not need any external system for alignment and could be fabricated on the nano scale.

This simplifies the detection system design. But the main disadvantages are the need for extensive calibration and temperature compensation of "offset" and "sensitivity", since piezoresistor change their resistance value because of leakage currents.

## Capacitive-based detection

The physical structures of capacitive sensors are simple. Essentially the device comprise a set of parallel plates and the capacitance is given by

$$c = \frac{\varepsilon_0 \varepsilon_r}{d} A$$

where $\varepsilon_0$ is the permittivity of free space, $\varepsilon_r$ is the relative permittivity of the material between the plates, A is the area of overlap between the plate electrodes, and d is the separation between the electrodes. In this configuration, there is a linear relationship between the capacitance and area of overlap. If we monitor the capacitance, we will be able to detect the motion of the sensor. One of advantages in the capacitive technique is that it is inherently less noisy than those based on piezoresistance due to the negligible thermal noise (thermal noise is effective small as the plates are massive). Another advantage, other than the noise level, is that no external alignment system is required. However, when the size shrinks to the micro or nano scale, the additional noise from the interface electronic circuits or thermal noise often exceeds the signal level. An added concern is the role of the fringe fields.

## Optical based detection

The optical detection system can basically be divided into two methods, Beam-bounce and interferometer-based detection. The optical based detection is capable of monitoring small vibrations all the way to the sub-angstroms scale.

## Optical Beam deflection detection

Most of the commercially available AFMs use the optical beam deflection method because of the simplicity of the experimental setup and the easy optical beam alignment. A simple setup is shown in picture 3-1. Because the noise level of this method depends on the geometry (optical lever length) and shape of the light beam, the noise level in practice is usually worse than that from interferometry detection. But recently [37] Fukuma et.al have developed a low noise cantilever deflection based on optical beam deflection which has the same noise level as that of an interferometer.

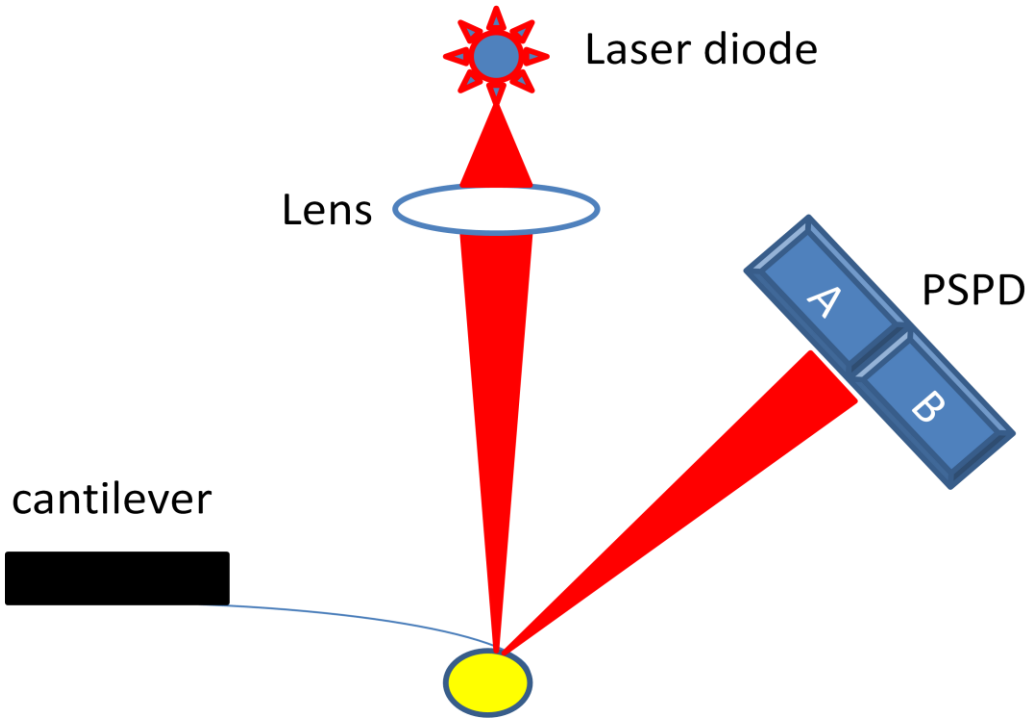


Figure 3- 1 Typical experimental setup for the cantilever deflection sensor using optical Beam deflection technique. The deflection of the cantilever is detected from the difference signal between the photodiodes A and B (PSPD stands for position sensitive photo-detector).

## Fiber-optic interferometer

Many cantilever deflection sensors have been used. But so far, the highest deflection sensitivities have been achieved with optical interferometers. For example, Rugar et al[38,39]. reported a fiber-based interferometer with 17 fm/(Hz)$^{1/2}$. and [40]Schȍnenberger et al. demonstrated a noise level of 6 fm/(Hz)$^{1/2}$ with a polarizing optical interferometer. The basic principle is that by using the cantilever and fiber end as simple Fabry-Perot Cavity as shown in picture 3-2., part of the light is reflected back into the fiber and interferes with the light reflected from the cantilever surface. Because of its simple design and low noise level, we will use an interferometer to monitor the motion of our cantilever.

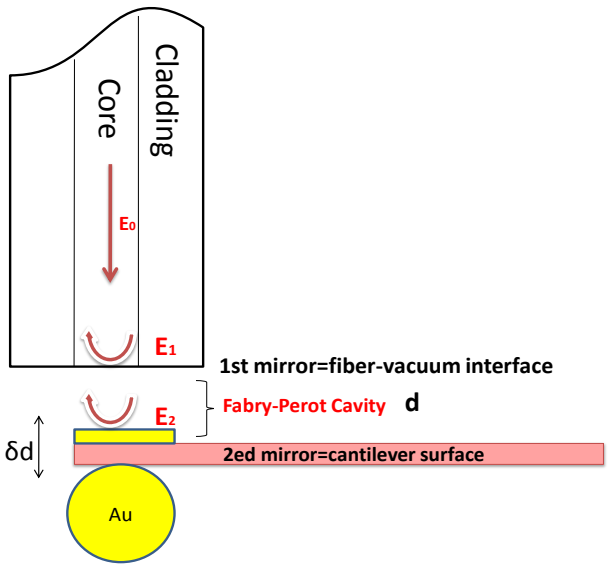


Figure 3- 2 The schematic of a fiber optic interferometer.

## 3.3 Theoretical considerations of a cantilever position sensors

### 3.3.1 Static Force measurement

The force measurement can be explained by the elastic response of cantilever to the first order term of tip-sample force that is related to Hooke's law. $\boldsymbol{F = kZ}$ where k is the spring constant of cantilever and Z is the elastic response (deflection of the end of cantilever). By measuring the deflection of cantilever, we can have the interaction force on cantilever. The minimum detectable force is determined by the characteristics of cantilever. In our static mode Casimir force measurement[41] using a commercial AFM, the force sensitivity can be as low as $0.01 pN/(Hz)^{1/2}$. However, in the static measurement, the signal is given by the DC deflection of cantilever which is subject to the 1/f noise background. The sensitivity is determined by the integrated noise level over the low frequency region. It usually degrades the sensitivity dramatically.

### 3.3.2 Force Gradient (Dynamic) measurement

In dynamic measurements, the cantilever is typically far away from the sample surface as compared to static force measurements and the excitation is done near or at the cantilever resonant frequency with a constant amplitude. A force gradient acting on the cantilever modulates the resonant frequency according to the equations given below. A cantilever driven by an external force can be treated as a damped harmonic oscillator. Thus, the equation of motion is given by:

$$mz'' + \frac{m\omega_0}{Q}z' + k(z - z_0) = F_{ext}(t) + F_{int}(z) \quad (3\text{-}1)$$

where $F_{ext}$ is the sinusoidal excitation force $A_{exc}e^{i2\pi\omega t}$ and $F_{int}$ stands for interaction force between cantilever sensor and sample which can be Taylor expanded at the average separation distance $Z_0$. Eq. (3-1) as,

$$mz'' + \frac{m\omega_0}{Q}z' + k_{eff}(z - z_0) = F_{ext}(t) + F_{int}(z_0) \quad (3\text{-}2)$$

where $k_{eff} = k - (\frac{\partial F_{int}}{\partial z})_{z=z_0} \Rightarrow \omega(z_0) = \omega_0\sqrt{1 - \frac{1}{k}(\frac{\partial F_{int}}{\partial z})_{z=z_0}}$

if $(\frac{\partial F_{int}}{\partial z})_{z=z_0} \ll k$, then, the responses of the cantilever deflection can be presented as :

$$\omega(z_0) - \omega_0 = \frac{\omega_0}{2k}\left(\frac{\partial F_{int}}{\partial z}\right)_{z=z_0} \quad (3\text{-}3)$$

The absolute value of the amplitude is given by

$$|A(\omega, z_0)| = \frac{A_{exc}}{\sqrt{(1-\frac{\omega^2}{{\omega_0}^2})^2 + \left(\frac{\omega^2}{Q^2{\omega_0}^2}\right)}} \quad (3\text{-}4)$$

and the phase angle between the driving and resulting signals is

$$\tan\psi = \frac{\omega\omega_0/Q}{\omega^2 - {\omega_0}^2} \quad (3\text{-}5)$$

The force gradient can be measured using several modes such as Slope or as described in the following section.

## ➢ Slope mode[42]:

The slope mode is usually referred to as the tapping mode in the common terminology of AFM systems. This technique measures force gradients by detecting changes in amplitude or phase of the cantilever with a constant drive at a frequency slightly off resonance as described by eq. (3-4), (3-5). A change in force gradient give rise to a shift in the resonance leading to a shift in the vibration amplitude of cantilever and phase change as shown in picture 3-3.

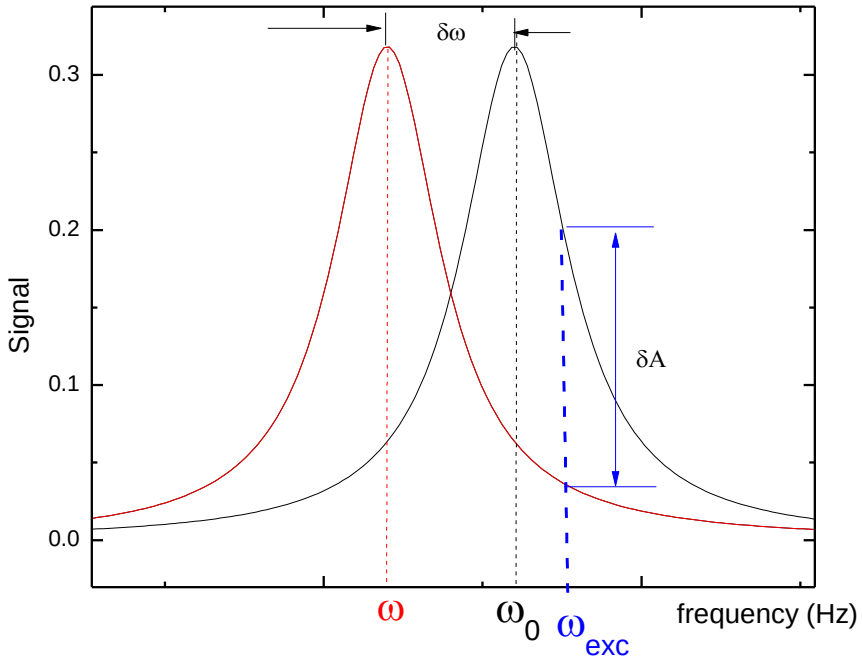


Figure 3- 3 In slope detection , the cantilever is excited at fixed frequency $\omega_d$ slightly off resonance. Force gradients are measured by monitoring either the amplitude change δA or phase change (frequency) δω

- **FM mode (**Frequency Modulation technique)

The frequency modulation technique[39,43,44] has been used to enhance the sensitivity of non-contact mode force microscopy in high vacuum because it is inherently insensitive to the amplitude vibration noise and can operate over a wide range. The FM technique uses the force sensor as resonator in an active feedback circuit. By phase shifting the resonator (cantilever) $90^0$ and driving it with the resultant waveform, the resonant frequency and amplitude of cantilever could be measured . In other words, if the phase shift between cantilever drive and signal is maintained at $90^0$ , the cantilever will be excited at its resonant frequency as eq. (3-5) shown. Because the force gradients acting on the cantilever can cause instantaneous shift of resonant frequency as shown in equation (3-3) where the $F_{int}$ is the interaction force, we can measure the force gradients through frequency demodulation. The eqs. (3-3) (3-4) (3-5) represent the response motion of cantilever. The cantilever can be treated as a damped harmonic oscillator that is driven by $\omega$ externally.

In the case of the phase-controlled oscillator set-up used for dynamic force measurement as shown in figure 3-4, the driving frequency is determined by resonant frequency $\omega$, Q, and phase shift $\varphi$. The main purpose of the block circuit is the controlled positive feedback with a phase $\varphi=1/2\pi$ to keep the cantilever at the resonant frequency and at a constant amplitude. Unlike the commonly used method "slope detection" as described in the previous section, the unwanted effects of changes in Q factor are also eliminated by exciting cantilever at the resonant state ($\varphi=1/2\pi$).

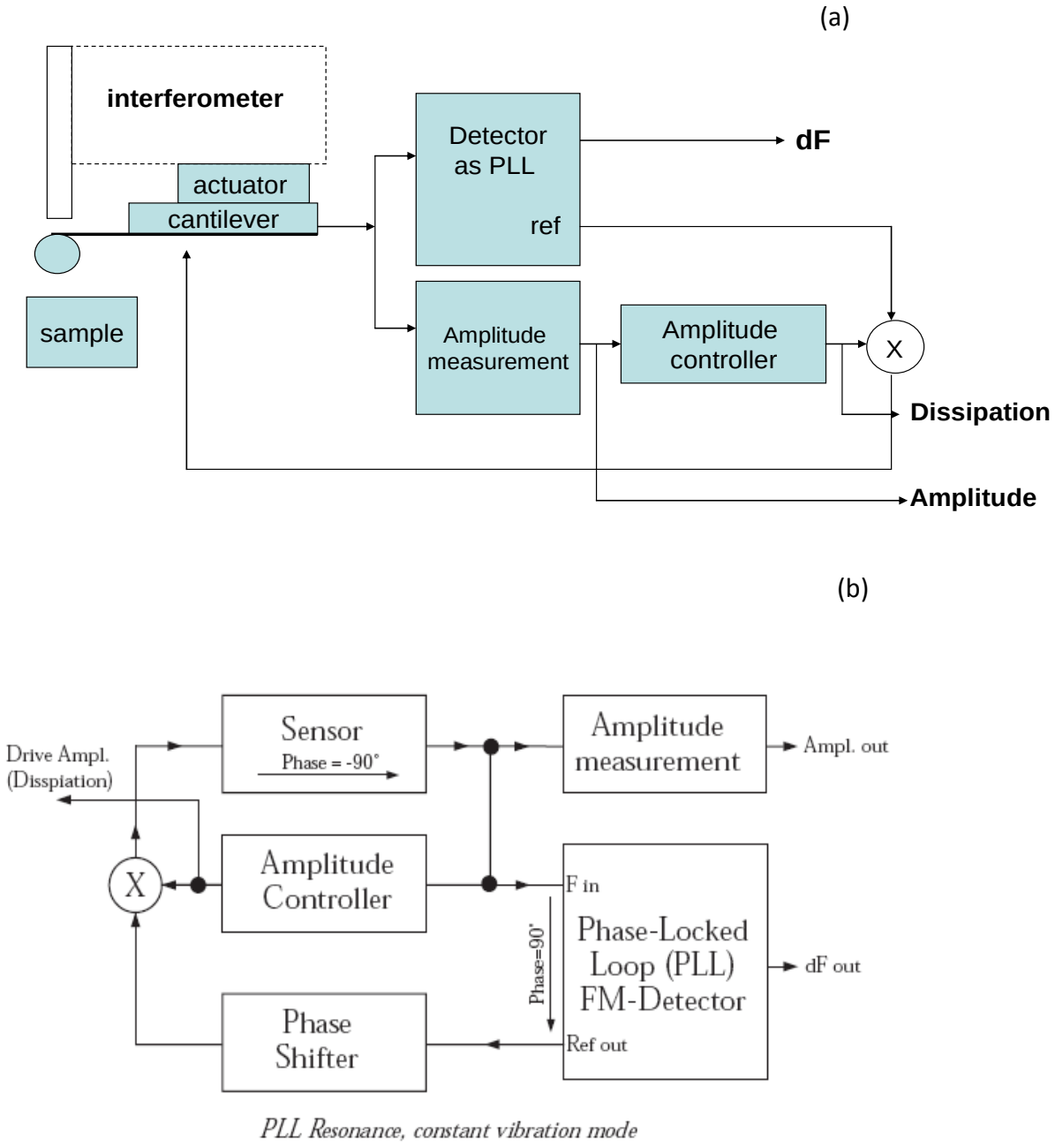


Figure 3- 4 (a) The block diagram of the constant amplitude mode of a frequency-modulation force detection method as provided by nano-surf. co. In picture (b), the phase locked loop used for the phase lock of $\varphi=1/2\pi$ between the driving voltage and interference signal to regulate the phase signal along with the FM-detector which outputs the frequency shift dF.

As shown in figure 3-5, a change in Q will cause the frequency shift which is coupled to a frequency shift due to an interaction force gradient. It will lead to a systematic error in our precise measurement.

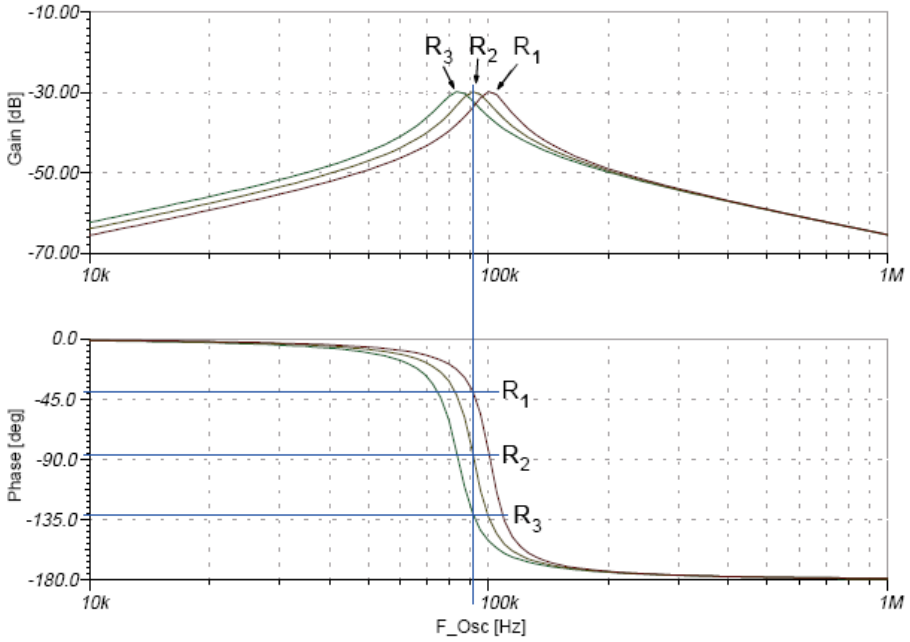


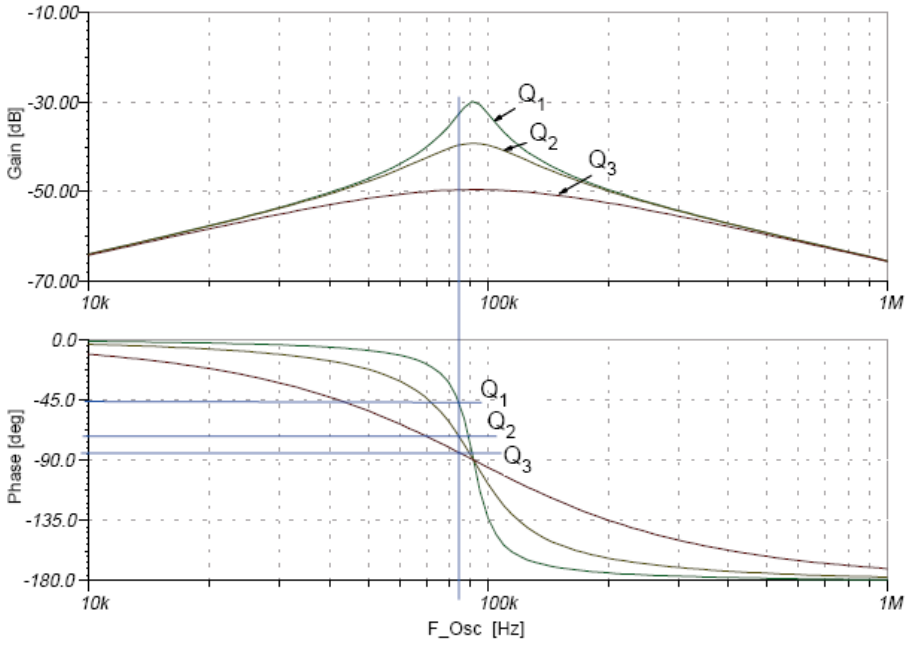

Figure 3- 5 The figures (x-axis is excitation frequency and y-axis are the gain of amplitude and phase, respectively.) indicate that a frequency shift might be indistinguishable between that resulting from a force gradient (conservative force as shown in (a)) or Q (dissipation as shown picture (b)). The change in the dissipation Q (Q1>Q2>Q3) can mimic as a shift of resonance frequency which can lead to systematic error in the force gradient measurement.

## 3.4 Instrumentation

A scanning force microscope is used to detect small force or force gradients e.g. from Casimir effect between a 100 micron sized sphere and sample surface. In order to achieve the best precision, we must pay more attention to each part of system to reach the lowest noise level. Our detection system consists of a cantilever attached to a 100 micron sized sphere, piezoelectric actuator, fiber interferometer including pre-amplifier, light source and electronics (PLL circuit, voltage amplifiers, etc.). Each of them contributes noise to the detecting system. The ultimate sensitivity of the system is determined by the summation of those noise levels. Apart from those noises, there are external noise sources including vibrations from pump, room floor low frequency oscillation or acoustic noise. Thus, with careful design of the vacuum system, we could make vibration noise approach the thermal amplitude of cantilever.

In the beginning of this chapter, the design of detection system as shown in picture 3-7 including vacuum system, short coherence length fiber-based interferometer, cantilever fabrication, FM-AFM and programming will be discussed. This is followed by contributions of each noise source in my system in order to approach the noise limited minimum detectable force gradient. Finally, we will demonstrate the improvement of precision Casimir force measurement by the dynamic mode (FM-AFM).

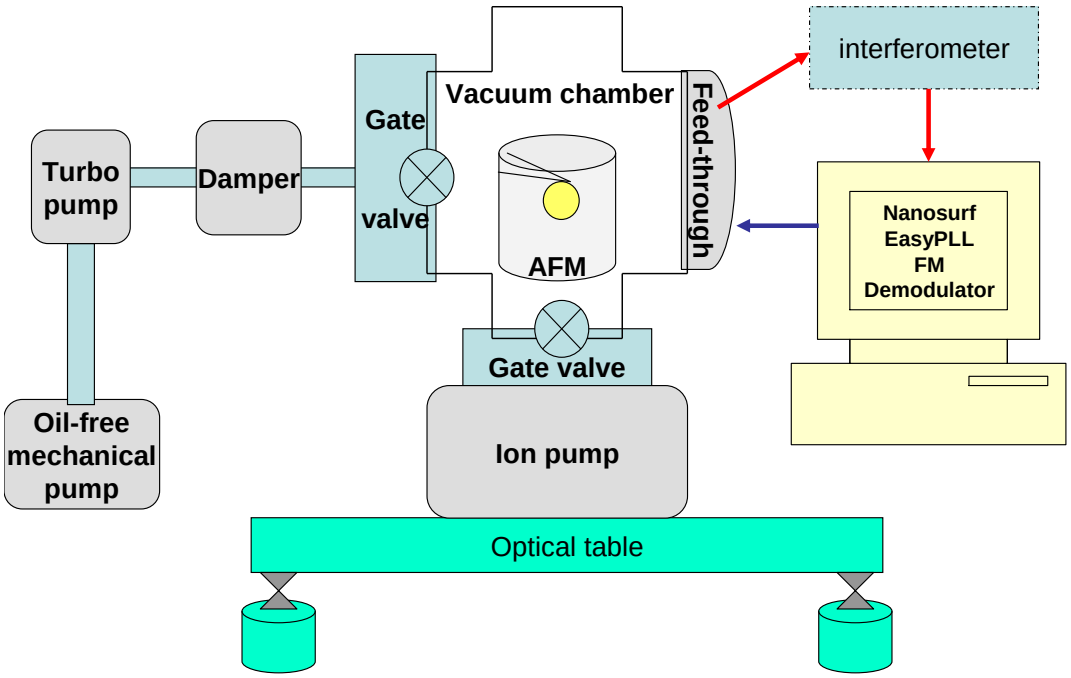


Figure 3- 6 Layout of the vacuum FM-AFM setup used in precision dynamic measurements of the Casimir force.

### 3.4.1 Vacuum system[45]

In a dynamic measurement, increased sensitivity is made possible by operation in a high vacuum by as it increases the Q factor of the vibration force sensor (cantilever)[46]. Also, it is important that the sample surfaces used in Casimir force measurements be preserved in the cleanest state possible, as the optical properties of the material are directly used for the Casimir force measurement. Those conditions require a high vacuum technique. Basically, our vacuum system as shown in figure 3-8 consists of five parts, pumps system, chamber body, valve, gauge and different kinds of vacuum feed-through. Before designing the vacuum system, one key parameter which is the ultimate pressure must be specified.

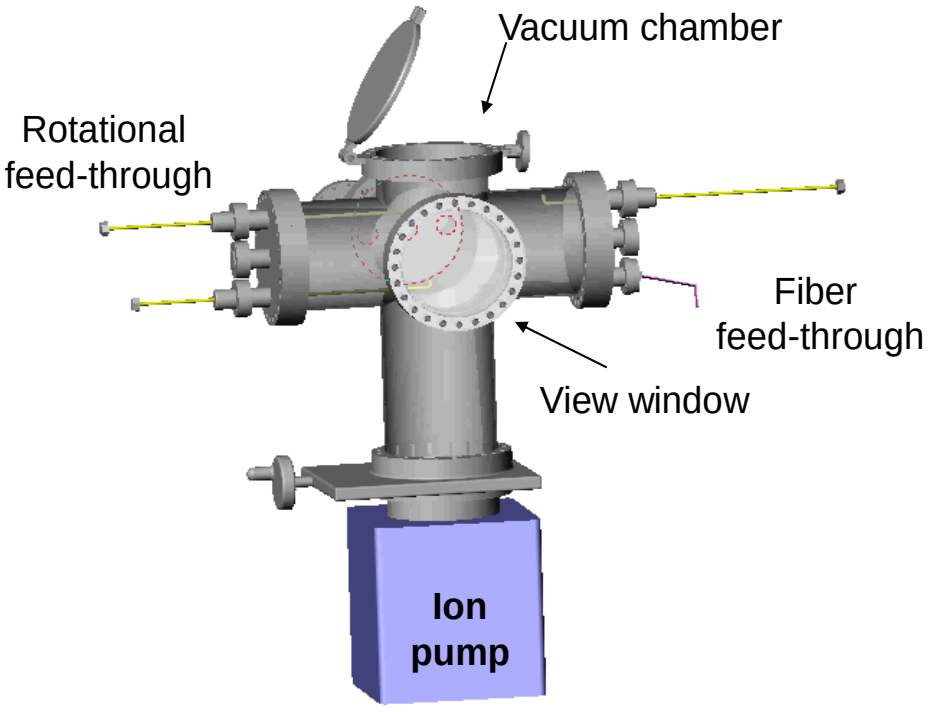

Figure 3- 7 Layout of the vacuum chamber with rotational feed-through and view window for manually aligning the fiber . The rotational feed-through used for align optical fiber.

- **Vacuum pressure:** The ultimate pressure requirement dictates the choices of the vacuum system. In our system for the precision Casimir force measurement, ultimate base pressure that we achieve is $10^{-9}$ Torr.
- **Chamber and pumping system:** The main chamber, is a six-way stainless cross, connecting the turbo-pump (V-301, pumping speed for nitrogen ~ 250 l/s) followed by an oil-free dry scroll pump which can reach a vacuum down to $2x10^{-7}$. To achieve pressures below $10^{-7}$ Torr, baking chamber is necessary to remove water or other absorbed molecule from vacuum system walls. Heating to 100 $^{0}$C for several hours and activating. ion pump can improve the ultimate pressure down to the $10^{-9}$ level. During data acquisition, the turbo and scroll pump will be turned off to reduce vibration noise. Thus, we close the valve (6" viton o-ring sealed gate with stainless steel construction) between the chamber and the turbo before venting the pumps by clean and dry nitrogen gas to make the mechanical pump system come to a complete stop. The pressure of chamber keeps going down when only the ion pump is active. Notice that the chamber should be supported on a damped optical table and designed to have a large mass to reduce the mechanical noise.

- **Gauges**: The vacuum pressure is measured by thermal–conductivity gauge for low vacuum (about $10^{-3}$ Torr) and an ionization gauge (from $10^{-4}$ to $10^{-10}$ Torr) connected to main vacuum chamber (to get exact working pressure).
- **Electric supply in vacuum**: We use type D subminiature connectors offering UHV feed-throughs with 25 pins which are hermetically sealed and electrically insulated using glass ceramic bonding. Feed-throughs are on CF conflate metal seal flange. For vacuum side connections, a kapton insulated in-vacuum ribbon cable and polyether-ketene thermoplastic connector meet the demands of our UHV system.
- **Optical-fiber feed-through**: the home-made optical fiber feed-through is made by cladding-stripped 1550nm SM28 fiber sealed by Varian vacuum Torr seal inside a clean stainless steel tube welding on a CF flange.
- **Surface preparation**: To lower the outguessing rate, any metal part put into the high vacuum environment must satisfy some surface requirements. The surface should be as smooth as possible to minimize the surface area and thus decrease the amount of adsorbed gas. In addition, organic, hydrocarbon oils, greases and water, must be removed from the surfaces of the vacuum apparatus. Disposable plastic gloves (powder free) are convenient for holding vacuum apparatus after cleaning.

### 3.4.3 Design of the short coherence fiber-optical interferometer

In my atomic force microscopic, a fiber optic interferometer shown schematically in picture 3 is implemented as the displacement sensor. A SLD (Super Luminescent Diode) with a wavelength of 1550 nm, serves as the light source for the interferometer. We use an IR wavelength because it is above the band-gap in silicon which prevents the cantilever heating and frequency fluctuation. The SLD is packaged with an FC-APC connection to the optical fiber. An optical isolator with FC-APC connectors (the fiber-air junction is intentionally cut at an angle) joins the diode to 50/50 directional coupler. The isolator attenuates light reflected back to the laser source by >58dB; therefore, it can prevent instabilities in the light source resulting from optical feedback.

The directional coupler splits the laser into 50% (primary output) and 50% (secondary output). The primary output is used for monitoring the laser power. The secondary output is a bare optical fiber which enters into the high vacuum chamber through a home-made (sealed with high vacuum sealant) conflates feed-through, and mounted on the oil-free xyz stage above the cantilever holder. Through the xyz stage and glass view window, we can control the fiber alignment in the vacuum chamber manually by the rotation of the vacuum feed-through. They are shown in figure 3-8. The fiber end is cleaved to give a mirror-like reflective surface (figure 2). Approximately 4% of incident light is reflected from the glass-vacuum interface. Most of the light transmitted out of the fiber end is reflected from the backside of cantilever to which it is aligned, and re-enters the fiber. Interference occurs between these two beams, providing the cantilever

deflection signal. In order to avoid unwanted back reflection, the ends of the fibers for signal output is terminated with an APC connector. There are issues relating to the operation of fiber-based interferometer. The active core diameter of 1550 nm SM28 fiber is 5um and the cantilevers we use are around 35um wide and 350um long.

Therefore, precise positioning of the optical fiber above the cantilever is major concern in any interferometer design. In our system, this is done with the help of a CCD camera and a high precision xyz stage. The gap between the cantilever and the fiber along the z-axis is maintained as small as possible to have better SNR (Signal to Noise ratio) in addition to a cavity length smaller than coherence length of light source.

However, the drifting of the cavity length limits the stability of the force sensor which always occurs at room temperature. A closed loop controls the distance between the fiber and the cantilever in our system.

## ➢ Principles of the fiber-based interferometer:

As mentioned above, the interferometer signal can be assumed to be a two beam system, low-finesse Fabry-Perot interferometer as shown in Figure 3-2. $E_0$ is the incident energy. Intensity $E_1$, $E_2$ are reflected from the mirrors 1 and 2

$$E_1 = r_1 E_0 \tag{3-6}$$

$$E_2 = \sqrt{\alpha(d)}\, r_2 t_1^2 E_0 e^{-i\theta} \tag{3-7}$$

where $r_1$ and $t_1$ are the reflection and transmission coefficients from fiber end (1st mirror), and $r_2$ is the reflection coefficient of cantilever (2nd mirror). $\alpha(d)$ is the attenuation coefficient of optical intensity due to the divergence of the light beam, which is closely related to the numerical aperture and core radius of the fiber. Θ is the optical path length difference between fiber and cantilever reflections and can be expressed as $\frac{4\pi nd}{\lambda}$, where n is a refractive index of cavity (vacuum) ~1 and d is the length of the cavity. The total power in the reflected beam can be obtained by time averaging the total output of the electrical field $E_1$+$E_2$ which is associated with the product of the overall output fields $E_1$+$E_2$ and its complex conjugate given by:

$$P_{out} = < (E_1+E_2)\,(E_1+E_2)^{*} > \tag{3-8}$$

$$= {E_0}^2 |{r_1}^2 + {r_2}^2 {t_2}^4 + 2r_1 r_2 \cos\theta| \tag{3-9}$$

$$= P_{input} \left| R_1 + \alpha(d) \cdot R_2 (1 - R_1)^2 + 2\sqrt{\alpha(d)} \cdot \sqrt{R_1 R_2} \cos\theta \right| \tag{3-10}$$

Where $R_1 = {r_1}^2 = (1 - {t_2}^2)$ and $R_2 = {r_2}^2$ are the power reflection coefficients. The typical fiber power reflection coefficient is given by

$$R_2 = \left(\frac{n_{fiber} - n_{vacuum}}{n_{fiber} + n_{vacuum}}\right)^2 \cong 4\%$$

where $n_{fiber} \cong 1.5$ $and$ $n_{vacuum} \cong 1$ are indices of refraction of the fiber and vacuum, respectively. Because of $R_2 \ll 1$, the equation (3-10) can be written as:

$$P_{out} = P_{effective}\left(1 + V\cos\left(\frac{4\pi nd}{\lambda}\right)\right) \tag{3-11}$$

Where the $P_{effective} = P_{input}(R_1 + \alpha(d) \cdot R_2)$ and a visibility $V = \frac{2\sqrt{R_1 R_2 \cdot \alpha(d)}}{R_1 + \alpha(d) \cdot R_2}$

According to equation (6), the interferometer response to a motion of the cantilever is given by:

$$\frac{\Delta P}{P_{effective}} = \frac{4\pi V}{\lambda} \cdot \Delta d \sin\frac{4\pi d}{\lambda} - \frac{4\pi V d}{\lambda^2} \cdot \Delta\lambda \sin\frac{4\pi d}{\lambda}$$

The most sensitive operating point is where the optical path difference is at the quadrature point i.e. $\boldsymbol{d = \lambda/8}$ , $\boldsymbol{3\,\lambda/8}$, $\boldsymbol{5\lambda/8}$ ..... as shown in figure 3-8

When the separation distance is at the Q point as shown in figure 3-9 and $\boldsymbol{\Delta\lambda}$ is ideally small (using PID control of the laser temperature and single mode fiber position) , the response for small amplitude oscillations of the cantilever is given by:

$$\frac{\Delta P}{P_{effective}} = \frac{4\pi V}{\lambda} \Delta d$$

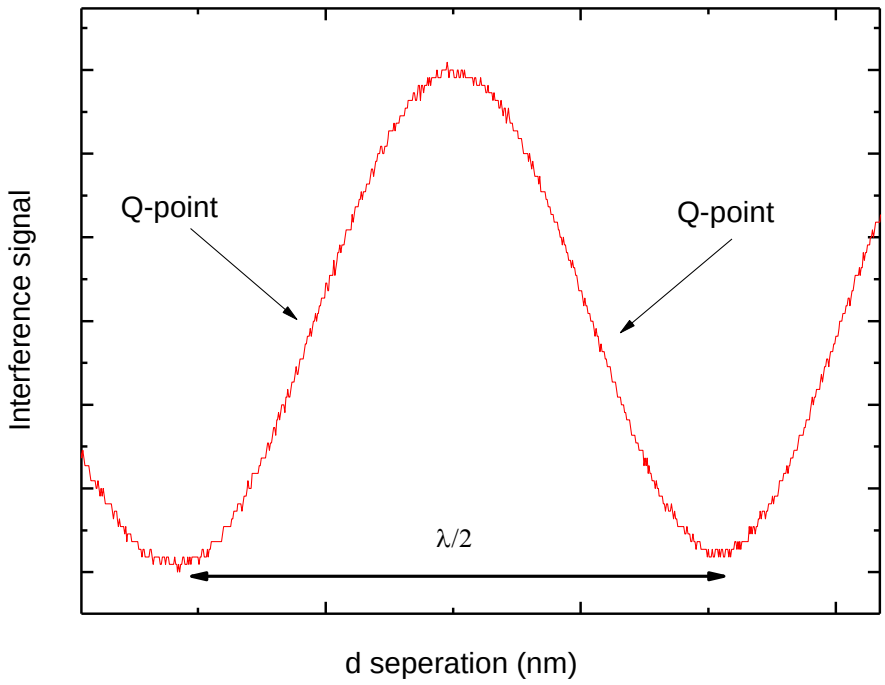


Figure 3- 8 Observed experimental interferometer fringes taken from a sweep of cavity length d at fixed wavelength 1550nm

## ➢ Short coherence length light source

Many of fiber-based interferometers for scanned probe application has been made of narrow-line-width He-Ne laser light sources. However, because of its characteristic, long coherence length, the stray reflections in the optical path led to spurious interferences and substantial low-frequency noise. Our experiment is based on the principle of LCI[47] (Low Coherence Interferometry) using an optical homodyne interferometer. It provides a coherence passive filter to achieve path-length selectivity. For a low-coherence length source, the auto-correlation function usually has the Gaussian profile shown in figure 3-9 as it is determined by the spontaneous emission. Then equation (3-6) can be rewritten as

$$\mathbf{P_{out} = P_{effective}\left(1 + V \cdot \frac{1}{2} e^{-\left(\frac{2d}{L_c}\right)^2} \cos\left(\frac{4\pi nd}{\lambda}\right)\right)} \quad (3\text{-}12)$$

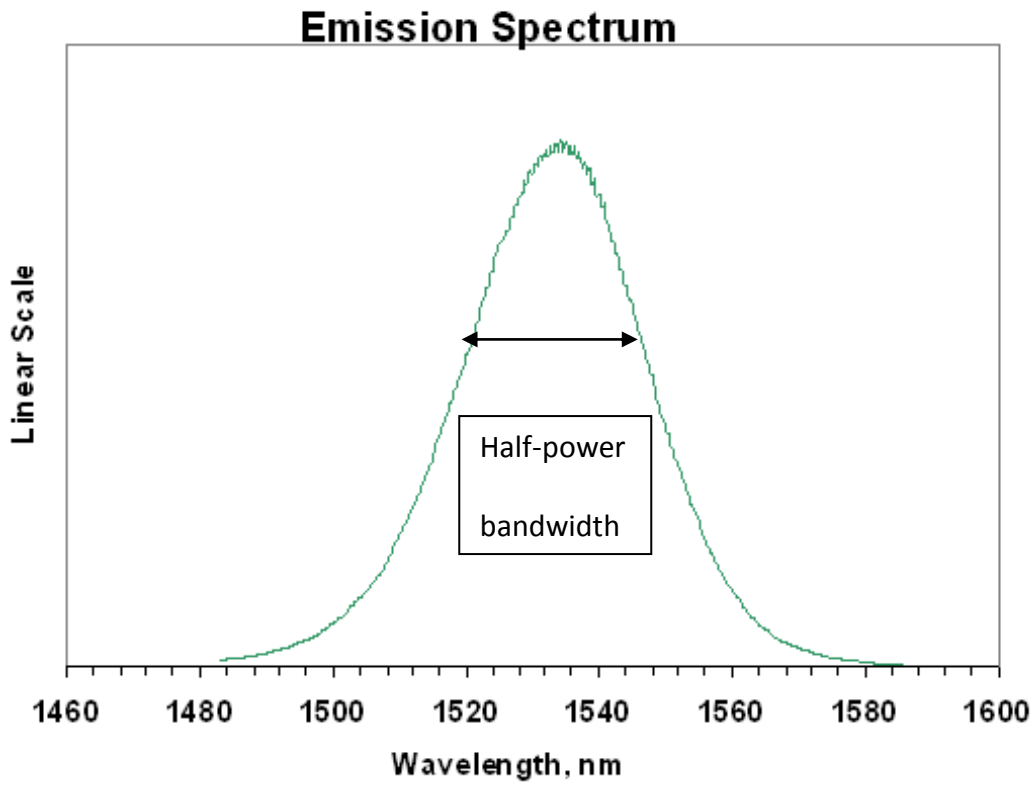


Figure 3- 9 The coherence length of the SLD used is Lc~($\lambda^2/\Delta\lambda$) =66um

The interference signal as we consider coherence length is given by equation (3-12) as shown in figure 3-9 (b).

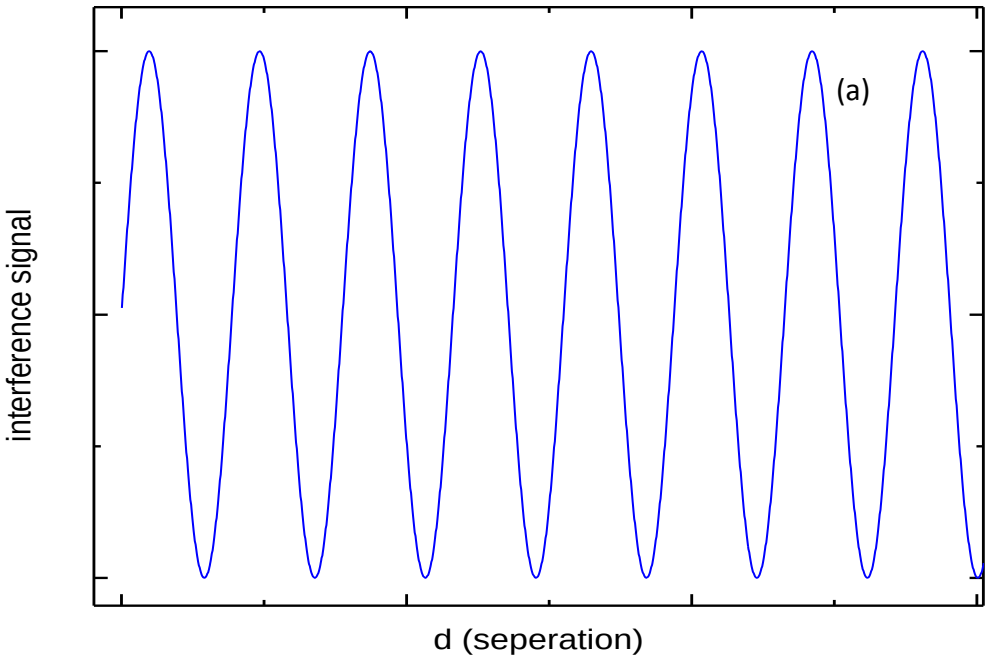
(a)
interference signal
d (seperation)

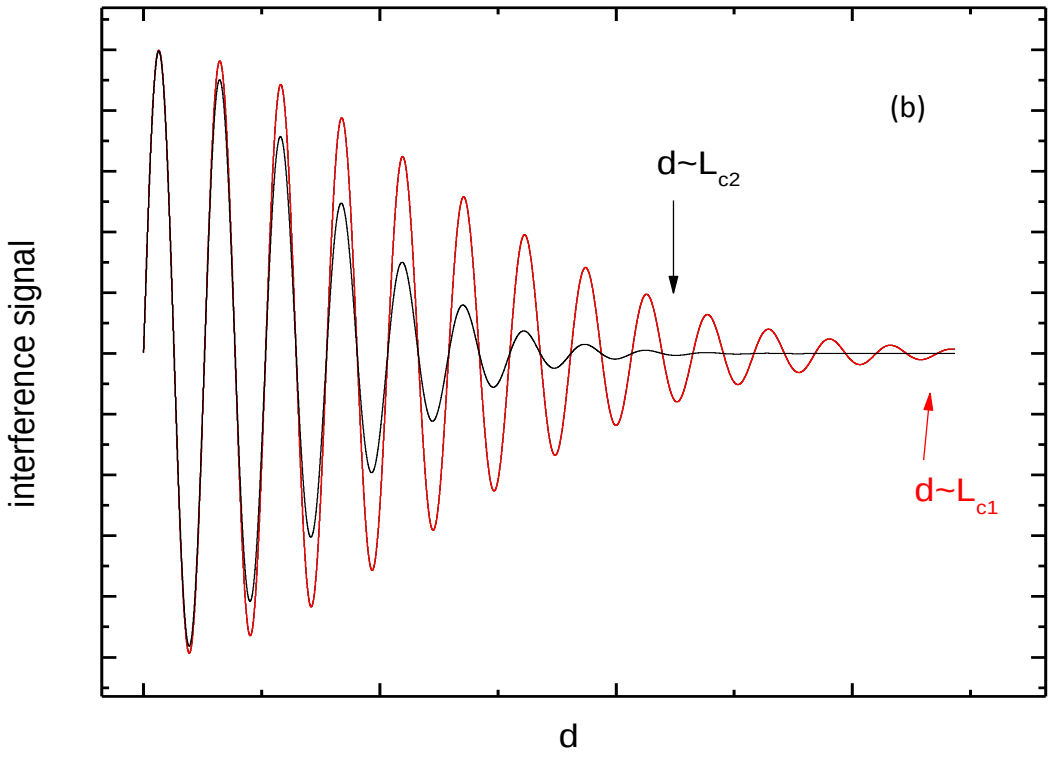
(b)
d~L_c2
d~L_c1
interference signal
d

Figure 3- 10 (a) indicates the regular laser (with long coherence length). Power of interference fringes follow sinusoidal function. Figure 3-9-(b) illustrates the case when the path-length difference reaches the coherence length, the interference signal almost vanishes. The difference between the red and black lines is when the coherence length Lc1 >Lc2. The coherence length acts as a filter to help in the selectivity of the preferred optical cavity.

Obviously, if the optical path length difference is longer than the coherence length, the interference signal from that cavity will be eliminated in the system. In figure 3-11, we compare noise the interference signal for three different light sources with different coherence lengths.

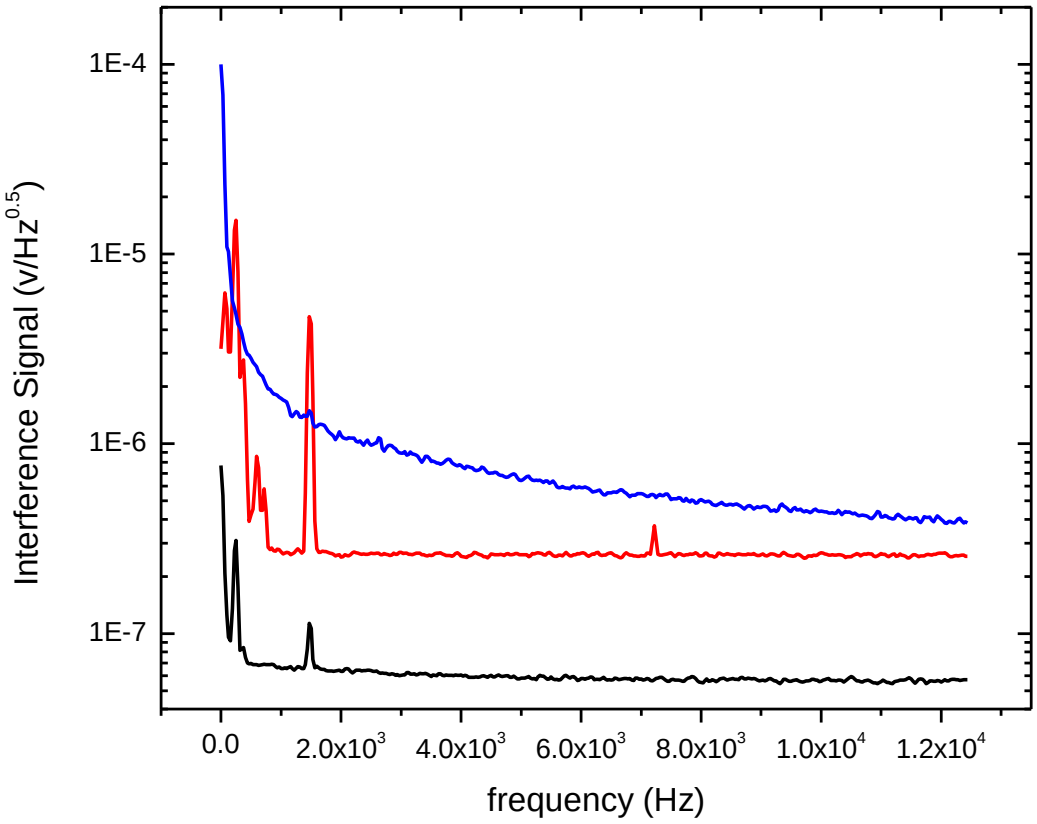

Figure 3- 11 The noise level of the interference signal (at the same power) from cantilever and fiber surface can be greatly reduced by selecting the coherence length. The blue line indicates the interference signal from a 1550nm DFB laser with a 0.1nm line width which corresponds to as coherence length $C_L$~24 cm. The red and black lines are signals from a regular laser ($C_L$~600um) and SLD ($C_L$~66um), respectively. The peaks of signal indicate the thermal noise of the cantilever. In the blue line (DFB), we are not able to observe thermal noise vibration because of the large background noise level. Therefore, it is clear that the corresponding noise reduction in the short coherence length source is because of spurious signals resulting from other undesired interference[45].

- **Coarse approach (xyz stage):**

For our microscope, we decided to use a commercial anodized black xyz stage to manipulate the fiber toward the cantilever because of its relative simplicity. But the anodizing may significantly increase out gassing rates because of its porous structure. Therefore, some special treatment need to be done before placing the xyz-stage into the high vacuum chamber. The treatments are discussed below.

1) The xyz-stage was first disassembled into several parts
2) Scrub them with strong solution of detergent in an ultrasonic cleaner.
3) Rinse with very hot water

4) Immerse and pickle the surface of the parts in a 10% solution of sodium hydroxide (NAOH) saturated with common salt (NACl) at $80^0$ C.

5) Polish in conventional wheel polishing machine.

6) Immerse those parts into 10% solution of hydrochloric acid to obtain a bright finish.

7) Rinse with DI water.

8) Re-assemble xyz stage with powder-free disposable plastic gloves.

9) Rinse with acetone and ethyl alcohol.

## ➢ Optical components

The basic optical components such as fiber, coupler, fiber connector, and fiber feed-through used to build up our interferometer are depicted in figures 3-5 and 3-6. The proper selection and careful design steps of each component can improve the signal to noise ratio in the interferometer

**Directional coupler**: First a directional coupler with the lowest return loss possible should be used. The one we used is a typical fused-tapered bi-conic coupler at 1550nm wavelength with return-loss of -55dB relative to the input power. In the future, we will use an optically contacted evanescent wave coupler with a specified return loss of -70dB to decrease parasitic fringes due to the return reflection from fiber and coupler.

**Fiber**: Because any changes of amplitude or phase of the signal becomes a displacement error in our interferometer system, fixing the fiber with tape on heat sinks and preventing hanging loops is necessary as they could vibrate at low frequency and lead to bending noise. Also, we used 1550B-HP 1550nm single mode fiber which has extremely low bending loss and low splice loss compared to the standard SMF-28 1550nm fiber. We found that using bend-insensitive fiber significantly reduced the noise level in the low frequency region when we monitor the interference signal on a spectrum analyzer SR560 (show picture).

**Optical-fiber feed-through:** To reduce the signal power attenuation, we need to avoid using bulkhead connectors that usually have ~0.3dB power loss. The home-made optical fiber feed-through is made by cladding-removed 1550B-HP fiber sealed (Torr-sealant which has very low vacuum weight loss and can withstand repeated temperature cycling from -200 $^{0}$C to 450 $^{0}$C) inside a clean stainless steel tube welded on a CF flange.

## ➢ Photo detector and electronics

There are two sets of interferometers in my system as shown in figure 3-11.

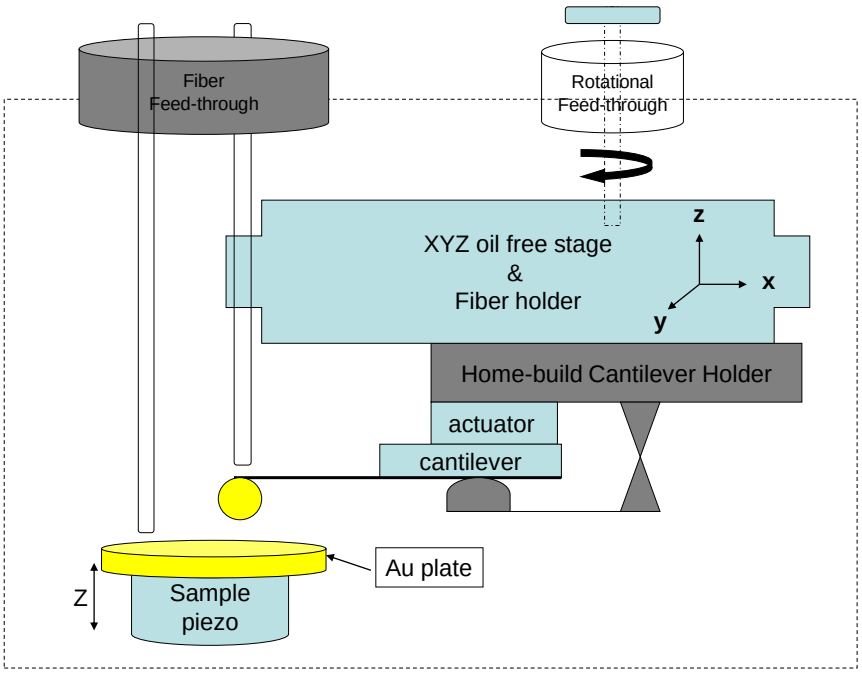


Figure 3- 12 The two sets of interferometers and the design of cantilever holder used inside the vacuum chamber is shown

One of them is used for monitoring the sample piezo movement with a regular laser diode. The other one is used for detecting the cantilever movement with the SLD. For the regular laser diode, we observe that the interference signal correlates significantly with the laser power. For having high signal to noise ratio fringe signal, there is a good benefit to use divider to normalize the signal to reduce the power intensity noise as shown in figure 3-13.

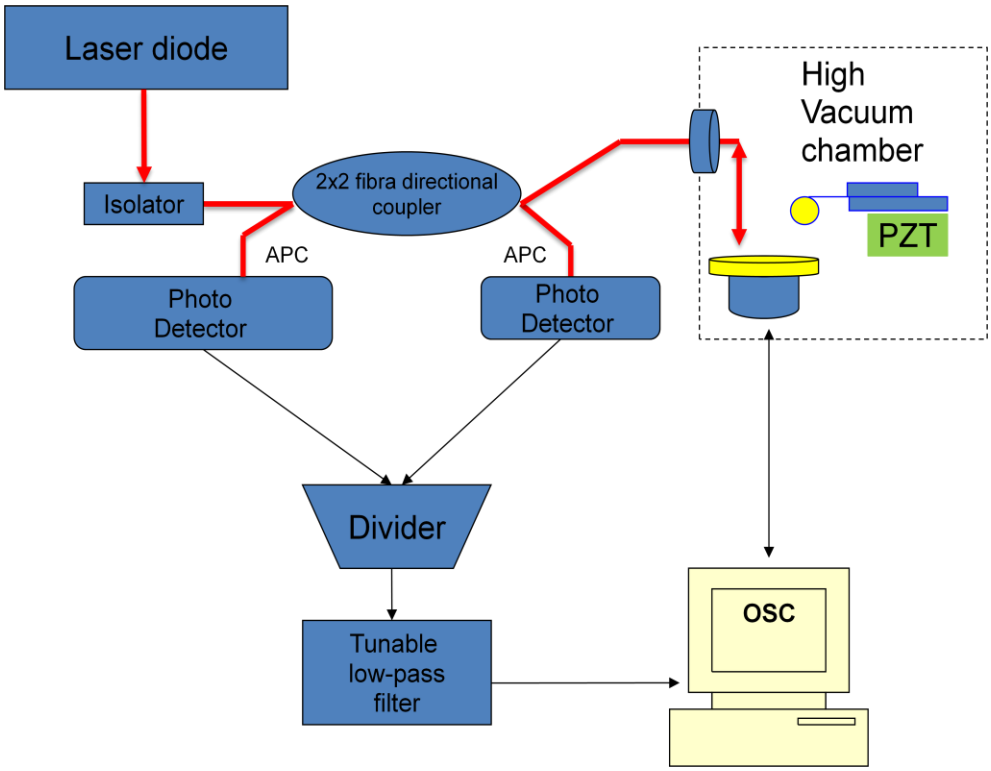


Figure 3- 13 The flowchart of interferometer we used to monitor and calibrate the movement of the sample plate piezo.

In contrast to the interferometer used for monitoring the sample plate movement, the noise level of the cantilever interferometer was not correlated with the light source power. To avoid any potential error source or noise the from divider or balancing system, we simply use the photon detector coupled to an OPA627 low noise operational amplifier (very high input impedance~$10^{13}\,\Omega$) as a trams-impedance amplifier. As shown in picture 3-14, the output interference signal directly goes into a band-pass filter cascaded by low and high pass filter to cut off unwanted frequency bands. The filtered signal is fed into the nano-surf PLL electronic device for Frequency Modulation detection. The other channel of the interference signal is fed into the divider and coupled with laser

output from second lead of optical directional coupler to form a closed loop PID control of the separation distance between the fiber and the cantilever during FM detection.

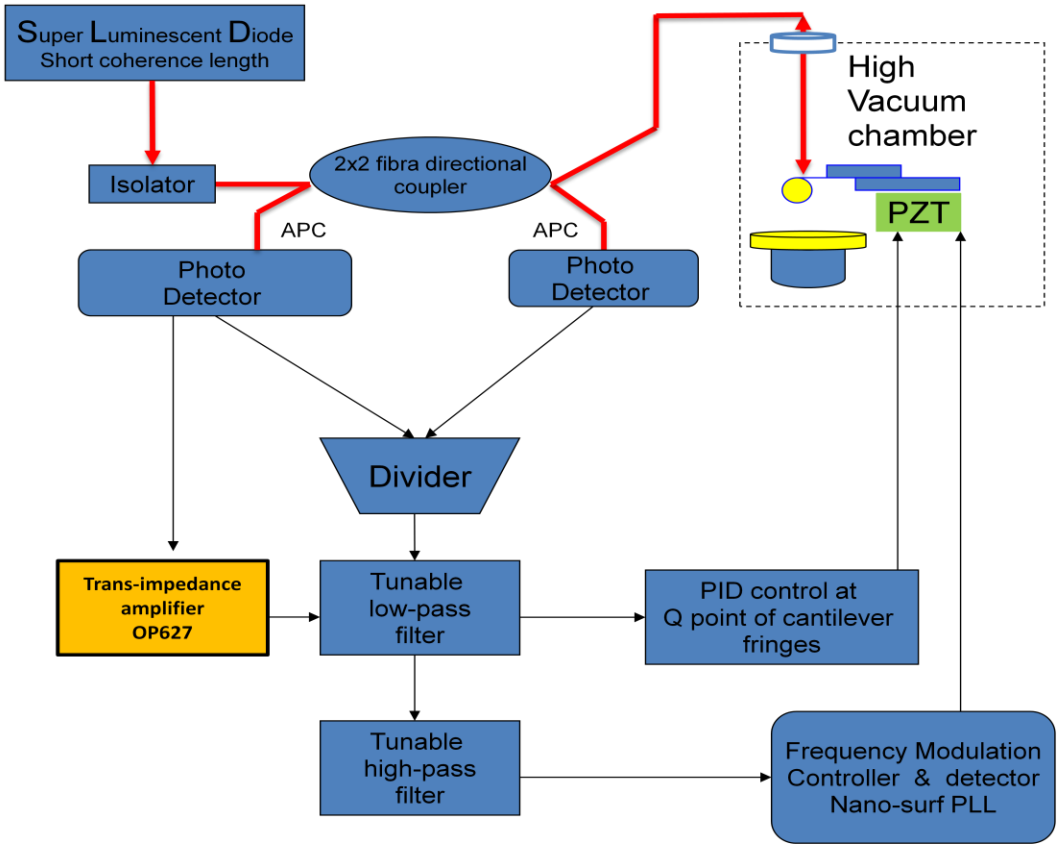


Figure 3- 14 The flow chart of my fiber-based interferometer experiment setup. The resonant frequency shift is detected by the FM-controller and detector. The separation distance between the fiber and the cantilever is PID controlled to keep it constant during measurement.

### 3.4.4 Design of piezo actuators

For precise Casimir force measurement, the most important thing as mentioned before is reproducible measurement of separation between two sample surfaces. It needs to precisely control the Piezo actuators. In our detection system, a piezo tube and monolithic chip multilayer piezo are used for controlling sample movement and cantilever actuation.

**Cantilever Piezo Actuator:** These actuators are made from ceramic material in which the piezo-ceramic properties such as stiffness, capacitance, displacement, temperature stability, leakage current are optimally combined. Because the lack of polymer insulation (lower out gassing rate) and the high Curie temperature, it is well suited to a high vacuum environment. As figure 3-13 shown, the piezo actuator is glued to a home-made holder. The cantilever is below the piezo and fixed by a spring clip. Thus, the cantilever can be oscillated at any chosen frequency. Note that since the displacement of a piezo actuator is based on ionic shift and orientation of the PZT unit cells, hysteresis and creep are unavoidable effects in piezo movement as shown in figure 3-16. However, by using the interferometer calibration one can precisely determined the movement of the piezo which we will present in chapter 4 **.**

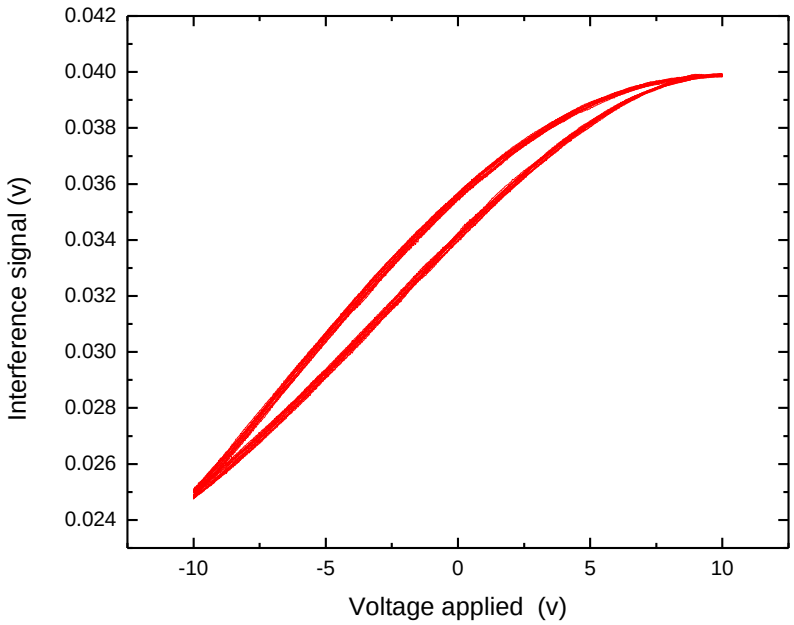


Figure 3- 15 Hysteresis curves of an open-loop piezo actuator . The hysteresis is related to the distance movement. Noted that for periodic motion, creep and hysteresis do not affect repeatability.

**Sample piezo tube:** In our experiment, we use a commercial piezo tube made by Veeco (E-Scanner) as shown in picture 3-17 and 3-18. The E-Scanner provides 3-demensional movement and is combined with A/D converters and feedback loop to perform a sample image.

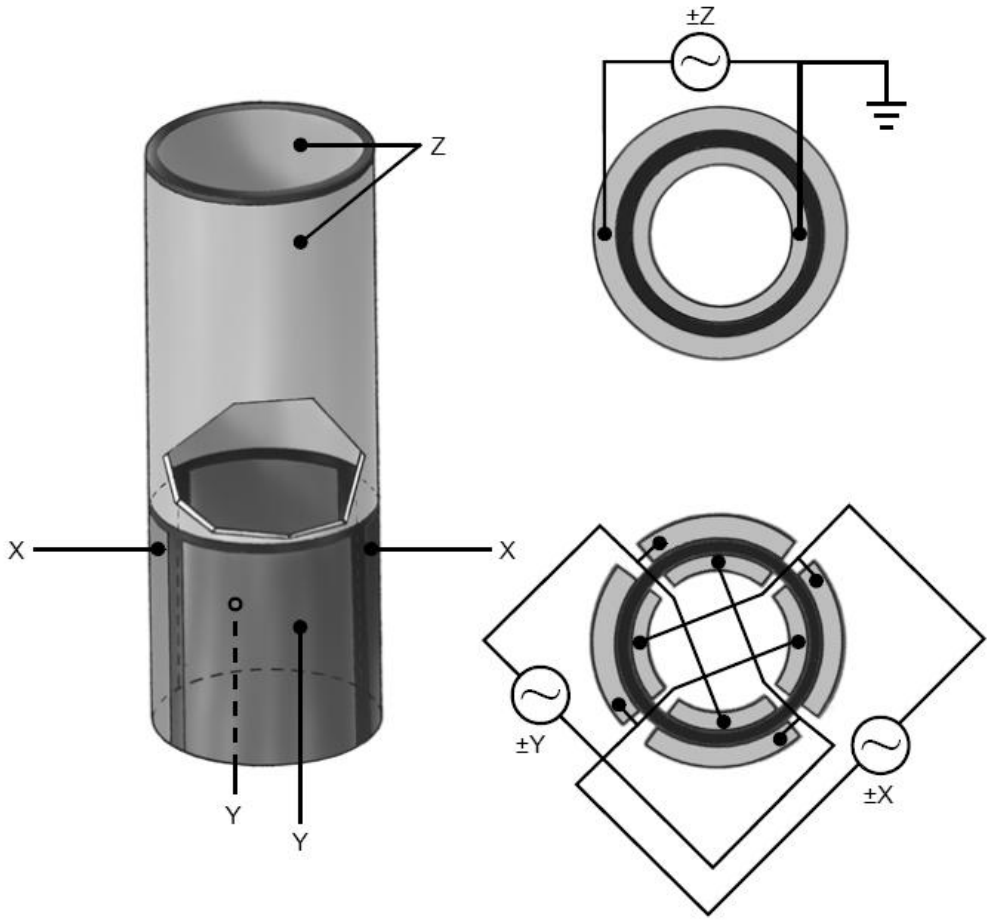


Figure 3- 16 The typical electrode configuration on the piezo tube. (provided by Veeco instruction manual)

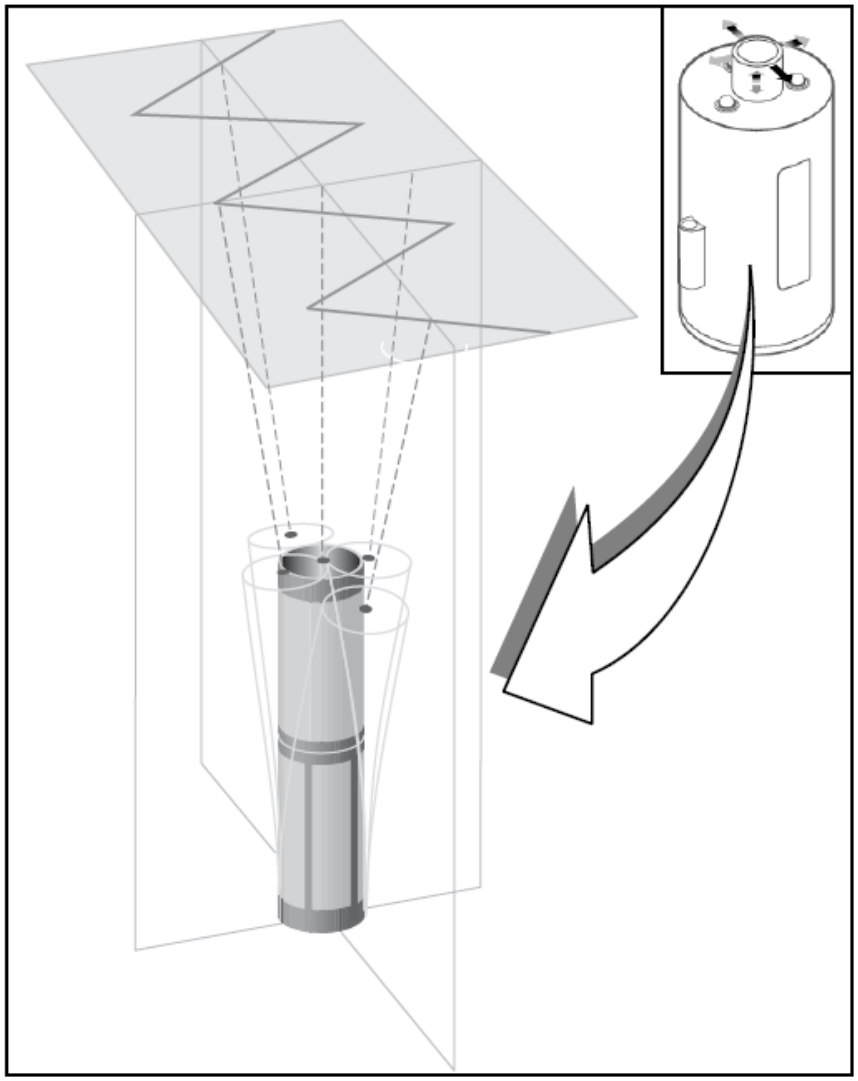

Figure 3- 17 AC voltages applied to the scanner crystal X-Y axes produce a raster-type scan motion shown. The picture is provided by Veeco.

### 3.4.5 Force sensor (cantilever) fabrication

In selecting an FM-AFM cantilever, we need to consider many parameters. The first priority is the consideration of force sensitivity which is limited by thermal noise. The thermally limited minimum detectable force gradient is given by[46,48]

$$F'_{\min} = \frac{1}{A}\sqrt{\frac{4kK_BTB_W}{f_0 Q}} \tag{3-13}$$

Substituting $k = \frac{Ywt^3}{4L^3}$ and $f_0 \cong \sqrt{\frac{k}{0.24m + M}} = \sqrt{\frac{k}{\rho Lwt + M}}$, where k is the spring constant and $f_0$ is resonant frequency, M is mass of the sphere coated with metal. If we ignore the mass M, then the minimum detectable force gradient in bandwidth $B_w$

$$F'_{\min} = \frac{1}{A}\sqrt{\frac{4kK_BTB_W}{f_0 Q}} \cong \frac{1}{A}\sqrt{\frac{wt^2 K_BTB_W}{LQ}}(Y\rho)^{1/4} \tag{3-14}$$

where Y is Young's modulus, L, w, t are the dimensions of the rectangular silicon cantilever which represent the length, width and thickness.

From the equation (3-14), the sensitivity is optimized by using narrow, thin, and long cantilevers. We used commercial silicon rectangular cantilevers which are 350um long, 35um wide and 1um thick. Notice that the use of the cantilever with high Q also helps to reduce the frequency noise . Therefore, the material for cantilever should have little internal dissipation. This holds for single crystal silicon. We use a silicon cantilevers with a sphere attached and coated with a gold film.

According to equation (3-13), the resonant frequency is dramatically lowered by adding mass to it. If the frequency is reduced below 1kHz (usually the knee of the 1/f noise level in my system), the sensitivity will be reduced because of the low frequency noise level. Therefore, instead of the polystyrene sphere (heavier and solid sphere), we use a 3M hollow silica sphere (Scotchlite glass bubbles).

For Casimir force measurement, the metal coated sphere attached to a cantilever is the major tool. However, as the Au films cover the entire cantilever, they tend to dramatically reduce the quality factor. This can potentially degrade the sensitivity in thermally limited measurements. Due to this concern, the cantilever is only coated at the tip by shadow masking the cantilever with a razor blade. The alignment and thermal evaporator setup used for this purpose are shown in figure 3-18 and figure 3-19. The finished force sensor for Casimir force measurement is shown in figure 3-20.

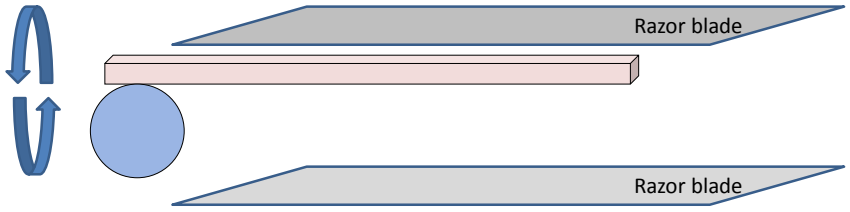


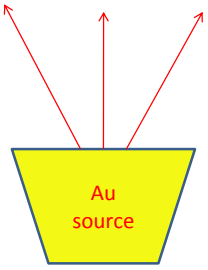

Figure 3- 18 The cantilever attached with silica sphere is shadow masked by a razor blade and rotated in vacuum with a high torque and stable stepper motor during the evaporation of Au.

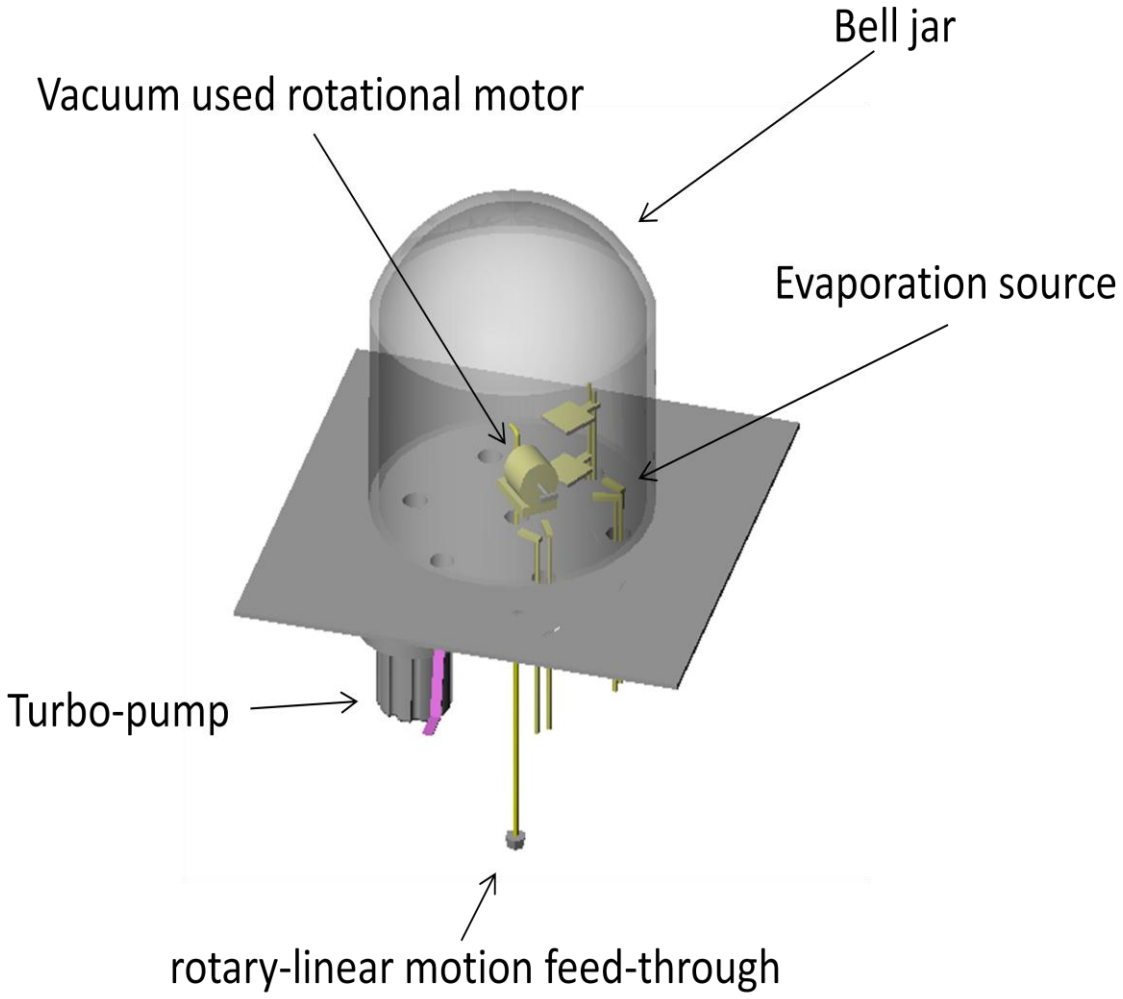


Figure 3- 19 The design of the resistive (thermal) evaporation system. It consists of filament coil (evaporation source), vacuum chamber (Pyrex bell jar), pump system , rotational motor and different kinds of feed-through.

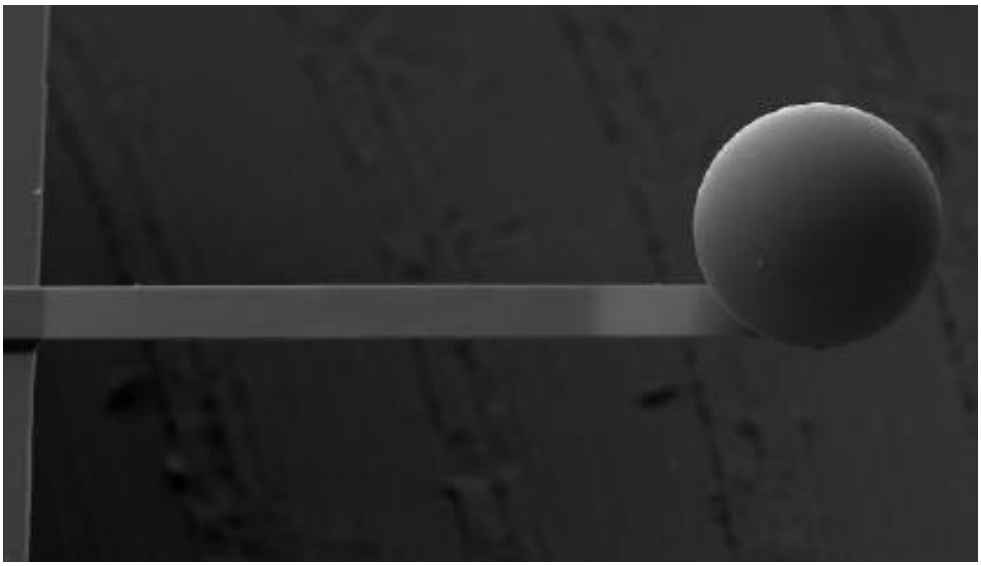

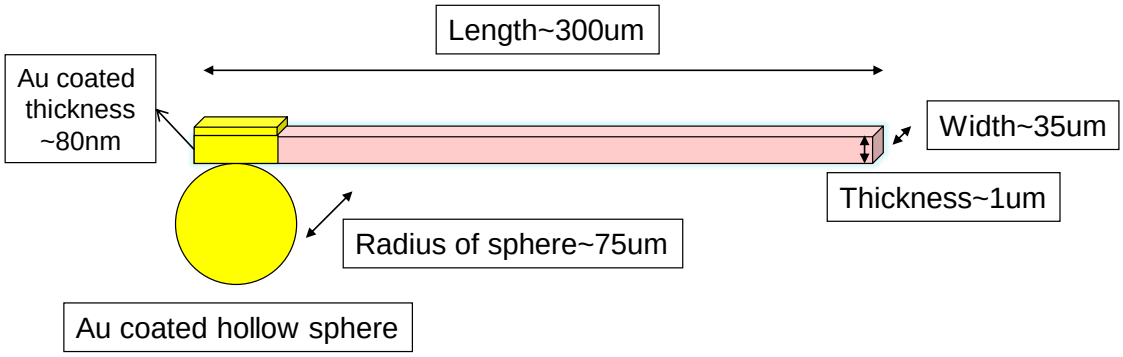


Figure 3- 20 (a) The SEM micrographs of Au coated cantilever (b)The finished Au coating sensor usually has a spring constant between 0.01~0.03 N/m, resonant frequency 1500Hz~5000Hz and Q factor of around 10000 after the gold coating.

### 3.4.6 FM controller and detector

Other than the interferometer used to monitor the motion of the cantilever, the FM controller and detector (frequency demodulator) are the two most important components in our system. We employ easy-PLL plus made by Nano-surf co. (including controller and detector) to measure the force gradient induced resonant frequency shift. The main function of the controller is to regulate the resonant amplitude and phase difference between the cantilever vibration and driving signal.

It consists of three parts. The first part is an analog phase shifter which can produces the phase shifted signal with respect to the reference which is the interference signal from "detector in" input. The second one is an RMS-to-DC converter used for amplitude measurement. The last part is an amplitude controller that consists of a PI-gain controller and a multiplier. By adjusting the set-point of the PI controller, the amplitude can be controlled to approach the set-point as shown in picture 3-21.

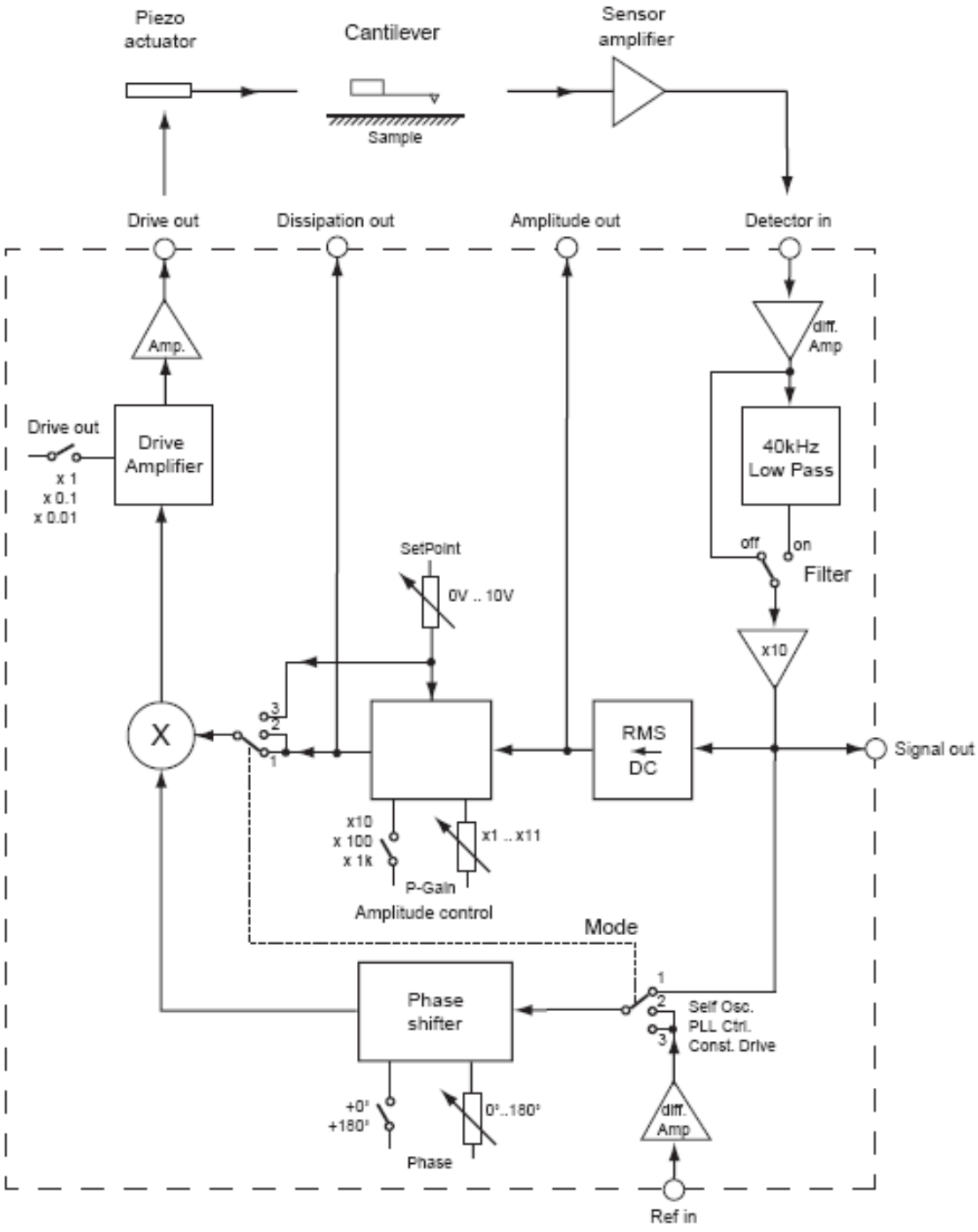


Figure 3- 21 The block diagram of the controller electronics (provided by nano-surf.)

The FM detector shown in figure 3-22 consists of three parts, a VCDO (voltage controlled digital oscillator), phase detector and PI controller as a PLL (phase lock loop). Note that the PLL circuit serves simultaneously as an accurate frequency detector because the control voltage applied to the VCDO is a measure of its frequency.

- **VCDO-** it digitally produces an internal signal and sets the phase shift with respect to the reference signal. In the locked-in state, the VCDO signal shows a mirror image (within the bandwidth of the PLL) of the frequency components contained in the cantilever response signal.

- **Phase detector-**is composed of a multiplier and a low pass filter. The input signal multiplied with the internal reference signal results in a low frequency term from difference of the two signals and the high frequency term from the sum of the two frequencies. Once the system is in the lock-state, the high frequency term is equal $2\omega$ which will be eliminated by a low frequency filter.

- **PI controller (PLL) -** it regulates the output frequency generated by the VCDO as a control voltage.

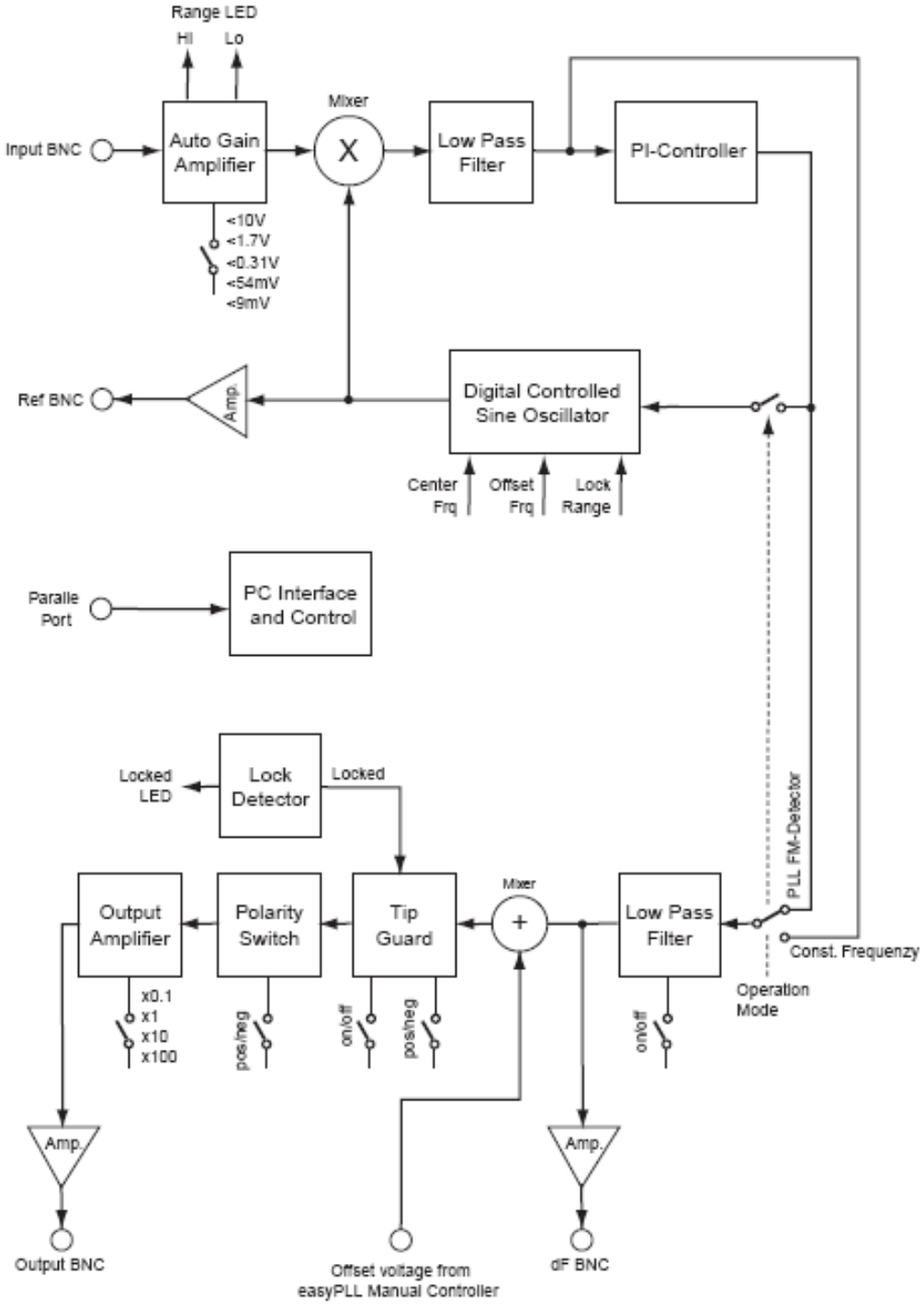


Figure 3- 22 The block diagram of the FM detector electronics (provided by nano-surf.)

### 3.4.7 Sensitivity and frequency noise level in FM-AFM[43,46,49]

In the frequency modulation AFM, we applied the phase locked loop technique to demodulate the frequency shift. It is an electronic circuit consisting of a variable frequency oscillator and a phase detector that compares the phase of the signal derived from the oscillator to an input signal. Thus, in the locked state, any phase noise added to the signal will be converted to the noise level of the DC output signal. For example, an ideal oscillator (cantilever) would generate a pure sinusoidal wave $v(t) = A\cos(\omega_0 t)$ It can be presented as delta function in the frequency domain as shown. In the real case, phase noises such as thermal (Lorentzian), electronic and interferometer noise (white noise ) are added to this signal by adding stochastic process represented by φ(t) to the signal as $v(t) = A\cos(\omega_0 t + \varphi(t))$ as shown in figure 3-23. Therefore, the phase noise (jitter) arising from thermal and instruments result in the frequency noise in FM-AFM. The root mean square frequency fluctuation can be presented as

$$\delta\omega = \sqrt{\int_0^{Bw} \omega^2 \boldsymbol{\delta\varphi}^2(\omega) d\omega} \qquad (3\text{-}15)$$

(see appendix 1) where $\delta\varphi$ is **the** phase noise density. It can be measured by the Spectrum analyzer and related to the spectral density and detection bandwidth $B_w$[50].

The sensitivity of the FM technique is usually limited by three major noise sources[43,46].(1) The intrinsic noise of sensor due to thermal excitation and its own characteristics, (2) the noise of frequency detector (FM controller and detector) and (3) the noise generated by electronics and the interferometer associated with the detection of

the resonator response. In our detection system for Casimir force gradient measurement, the third noise source dominates the first two.

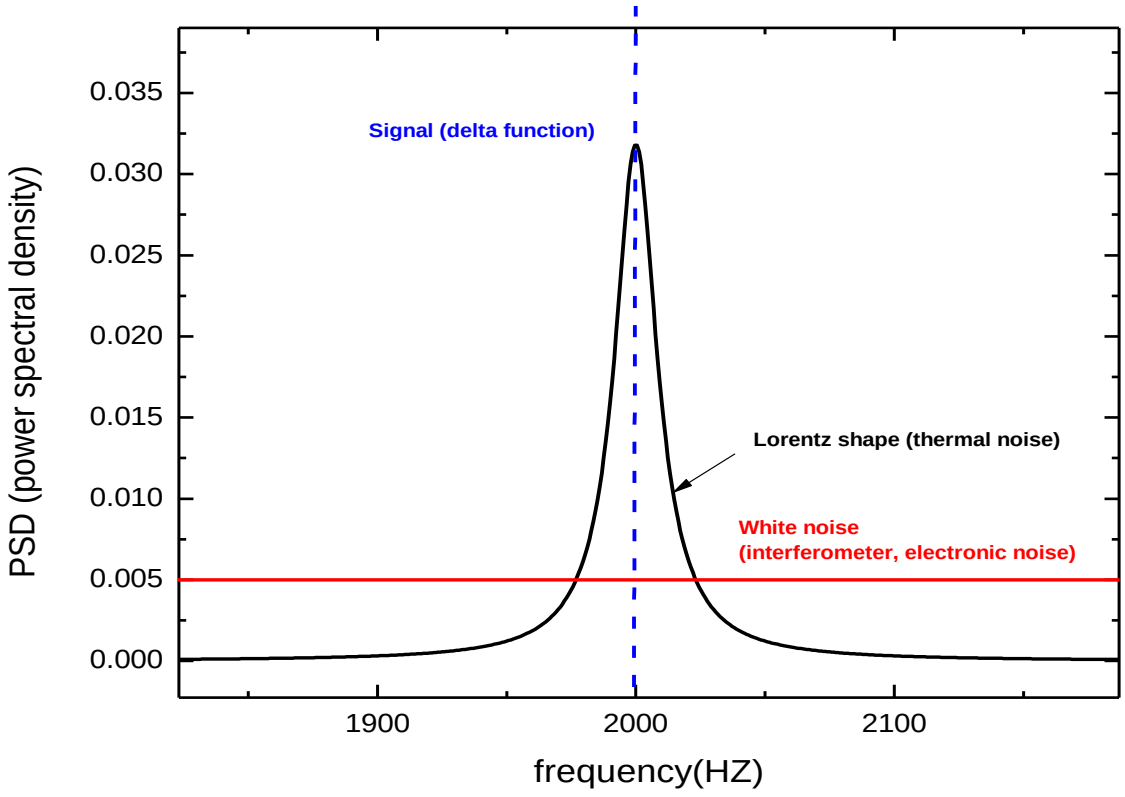


Figure 3- 23 The blue dashed line indicates the "ideal" oscillator signal with sinusoidal function which is delta function in the frequency domain. Considering the phase noise jitter from the thermal noise and other white noise as shown in the red solid line and black line, the noise level due to phase jitter will be added into the DC signal from the PLL loop.

**Thermal noise:** The intrinsic frequency noise due to thermal excitation of the cantilever as we mentioned before is $\delta\omega' = \sqrt{\frac{K_B T \omega_0 B_W}{E_0 Q}}$ ,where the $E_0=1/2kA^2$ is the

energy stored in the oscillator, and the $B_w$ is the detection bandwidth that can be controlled. In our experiment, the thermal amplitude of the oscillator is around 6Å and the Q factor and resonant frequency for our cantilever with sphere in ultra high vacuum is typically 10000~30000 and ~1.5kHz respectively as shown in figure 3-24. With these parameters, the frequency noise response to the thermal excitation is 1.2e-6 $\frac{Hz}{Hz^{0.5}} \cdot (B_w)^{0.5}$ corresponding to 3.8e-5 $Hz^{0.5}$ times the square root of 1kHz bandwidth which is the typical limited bandwidth for the frequency detector. Thus the spectral noise density due to thermal phase noise is a constant 1.2e-6 and related to $B_w$.

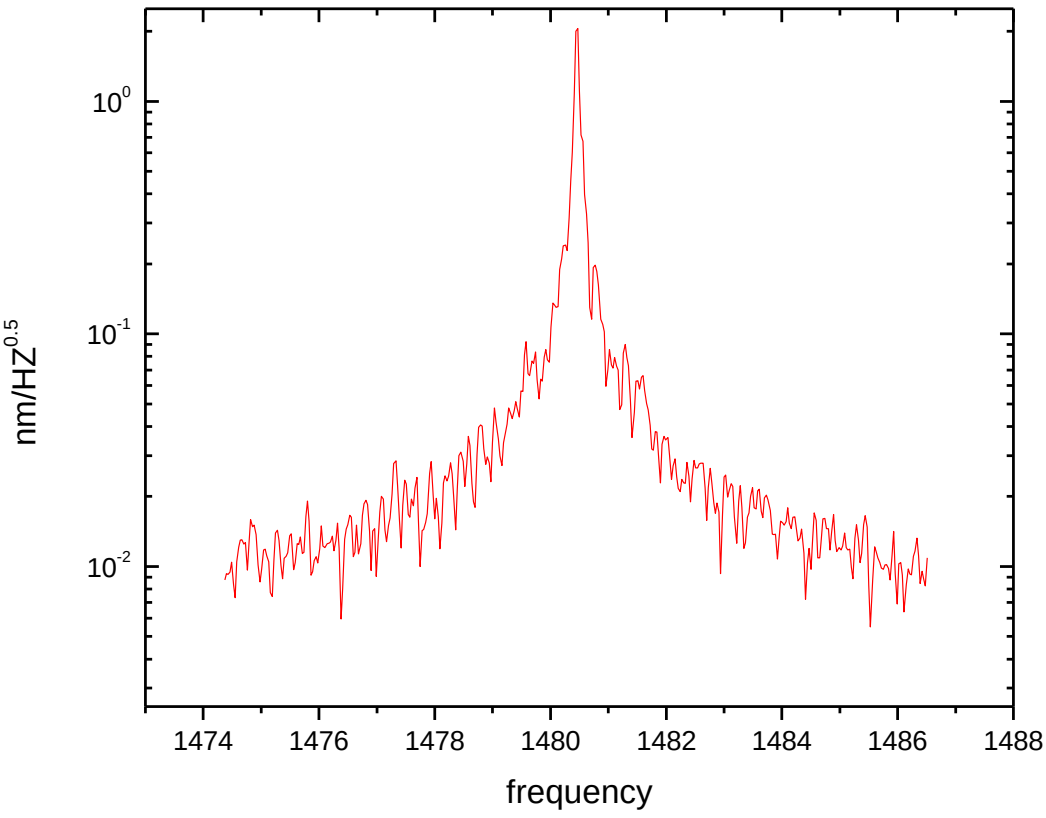

Figure 3- 24 Thermal cantilever noise in a vacuum of $10^{-7}$ (Torr). The x-axis is in Hz and the y-axis is in nm/$(Hz)^{0.5}$ (log scale). The parameters for the cantilever are: spring constant ~ 0.0125 N/m. Resonant frequency is ~1480Hz and Q~25000.

**Frequency detector noise** (phase noise due to FM controller and detector): We use the low noise AC signal from the function generator 33220A to test the noise level from the frequency detector. The AC signal was fed into the easy-PLL (frequency detector) and the output signal was analyzed with a spectrum analyzer SR 760. According to eq. 3-15, $\delta\omega = \sqrt{\int_0^{Bw} \omega^2 \delta\varphi^2(\omega) d\omega} = \delta\varphi B_w{}^{3/2}$ The frequency noise density from FM controller and detector can be presented as equation 3-16:

$$\frac{\delta\omega}{Bw^{1/2}} = \boldsymbol{\delta\varphi Bw} \qquad (3\text{-}16)$$

we assume that the $\boldsymbol{\delta\varphi}$ is a uniform phase noise density (white phase noise density) from frequency detector and $B_w$ is the detection bandwidth of the system. The slope of theory curve from eq.3-15 represents the phase noise density which is around 3.4-e7 (rad.•$Hz^{1/2}$) as shown in figure 3-25 (dashed line). With a bandwidth of 1KHz, this the ultimate instrumental sensitivity 6mHz specified by the company, Nano-surf, cannot be achieved. Therefore, it is worth noting that the noise level can be reduced greatly by low pass filtering the frequency shift signal as shown in figure 3-25 by the green (200Hz) and red curves (50Hz). If the ultimate sensitivity needs to be achieved, the detection bandwidth is the critical parameter which needs to be considered. The figure 3-26 represents the frequency noise level due to phase detector which is ~6mHz when we use the 200Hz filter.

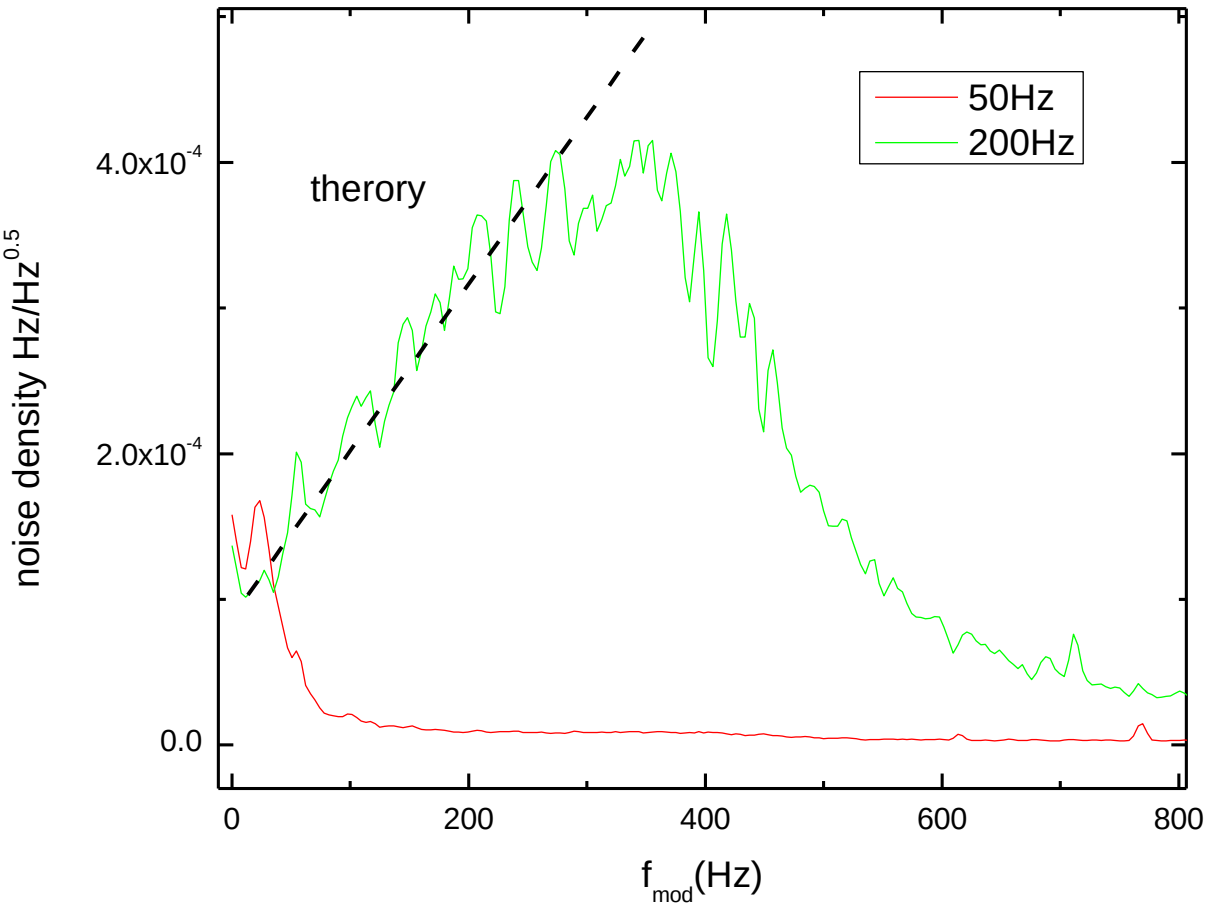


Figure 3- 25 The noise density of the FM controller and the phase detector. The input signal used for noise level test is from the very low noise function generator. Area underneath the curve shows the frequency noise. The dashed line shows the theory curve fitting from eq. 3-16. The deviation between the theory and test (experimental curve ) is due to low pass-filtering the output frequency signal.

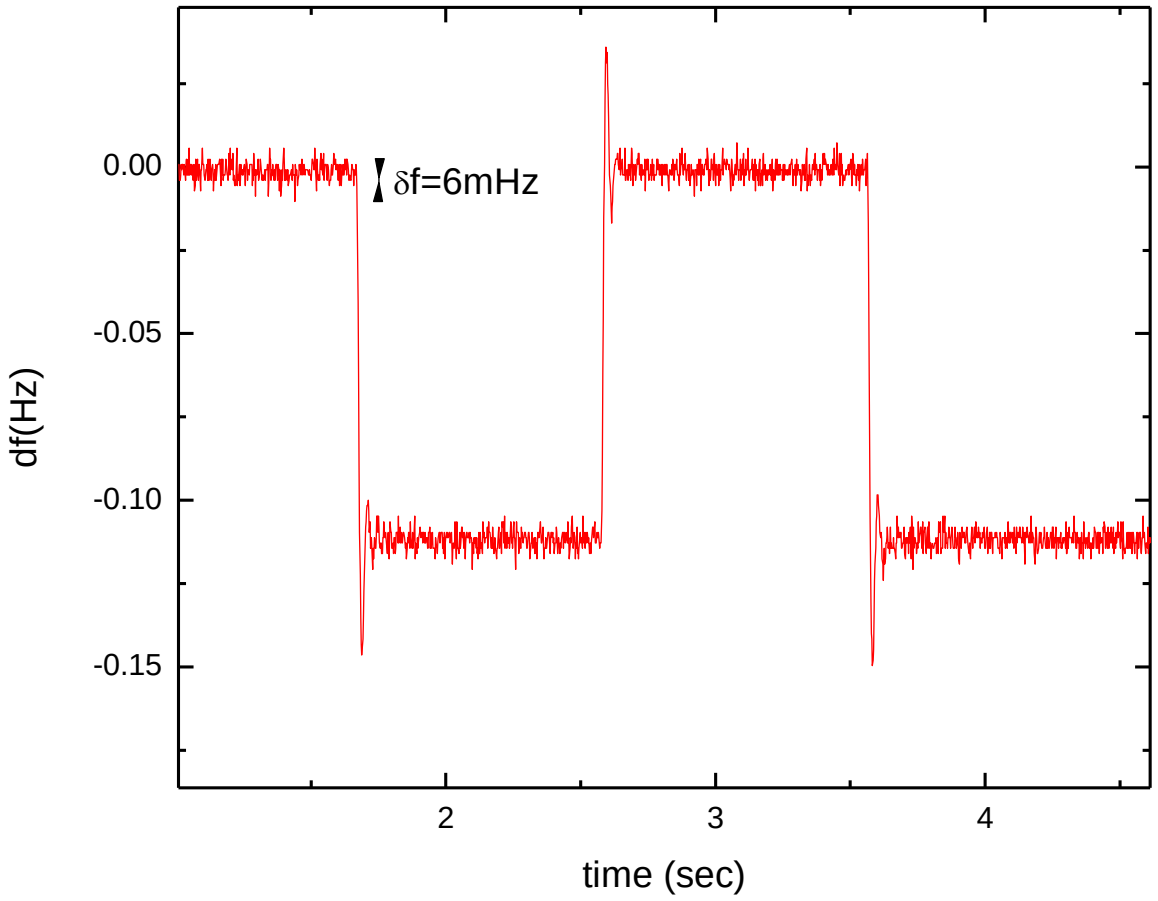


Figure 3- 26 A 0.1Hz square wave modulation and a 200Hz filter were used in the test of frequency noise level. The resolution of the phase detector is 6 mHz.

## Instrument noise source:

Even if the intrinsic (thermal) and detector noise is ideally small, we still have frequency fluctuation which originates from the finite SNR (signal to noise ratio) which can be measured. Assuming that a white noise signal with spectral density $\delta y^2$ is added to an oscillator signal y, the phase noise density[51] is given by

$$\delta\varphi^2 = \frac{\delta y^2}{2y^2} \tag{3-17}$$

According to eq.3-15, the corresponding frequency noise is

$$\delta\omega = \sqrt{\int_0^{Bw} \omega^2 \boldsymbol{\delta\varphi}^2(\omega) d\omega} = \frac{\delta y}{\sqrt{2}y} \mathrm{B_w}^{3/2} = \frac{\mathrm{B_w}}{\sqrt{2}\mathrm{SNR}} \tag{3-18}$$

is correlated to detection bandwidth $B_w$ and SNR. In our experiment, with the usual parameters and bandwidth $B_w$ ~50Hz and SNR ~1000, the frequency noise is 35mHz. However, if the resolution capabilities of the frequency detector need to be approached as shown in previous section, an SNR at least 6000 is required for the same bandwidth 50Hz.

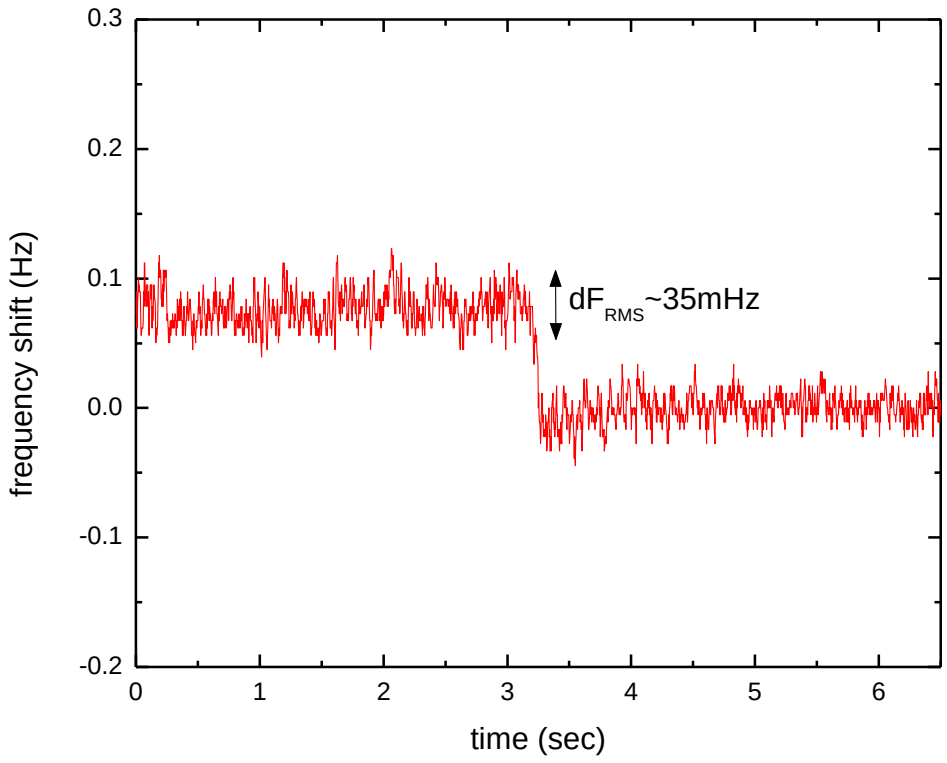


Figure 3- 27 A ~0.1Hz frequency shift due to square (voltage difference applied in-between sample plate and sphere) electrostatic force modulation. The RMS frequency noise level is ~35mHz (Q=10000, SNR~1000) as shown in eq.3-18 .

Therefore, how to improve the SNR to reduce frequency noise level in our system is worth discussing. As shown in section 3.4.3, we know that y is related to the amplitude of the cantilever and the laser power which can be presented as:

$$y \propto \Delta P = 4\pi v \mathrm{P}_{\mathrm{efftive}} \frac{\Delta d}{\lambda} \quad (3\text{-}19)$$

$\delta y$ is white noise spectrum originating from different noise sources. The common sources of noise in a fiber-based interferometer force microscopy are electronics noise (pre-amplifier noise) and optical noises (shot, laser intensity noise).

- **Electronic noises[52]**:

**Pre-amplifier noise:** Our Pre-amplifier consists of an OP-Amp and resistor. The noise level come from the Johnson Noise of the resistor and OP-Amp noise level. The noise level measured by the spectral analyzer is 50nV/Hz$^{0.5}$ for a 100kΩ load resistor.

- **Optical noises[55]:**

**Shot Noise** : Shot noise arises from statistics of photons incident on a photo-conductive detector. The shot noise can be described by the following equation**:**

$$\delta y_{shot} \propto \sqrt{2e\eta P_{efftive}} \quad (3\text{-}20)$$

where η is photo detector (A/W) efficiency and e is the electron charge.

**Laser intensity noise:** As long as the noise density is proportional to laser intensity, we call it as intensity noise. This noise comes from spontaneous emission, mode-hopping noise or laser phase fluctuation. The equation can be simplified as :

$$\delta y_{intensity} \propto e\eta P_{efftive} \tag{3-21}$$

In fact, the usual limit for the fiber-based interferometer is shot noise. The figure 3-28 depicts that the white noise density of interference signal is a function of square root of signal power $P^{0.5}$ . Hence, the shot noise is the dominant noise level in our system.

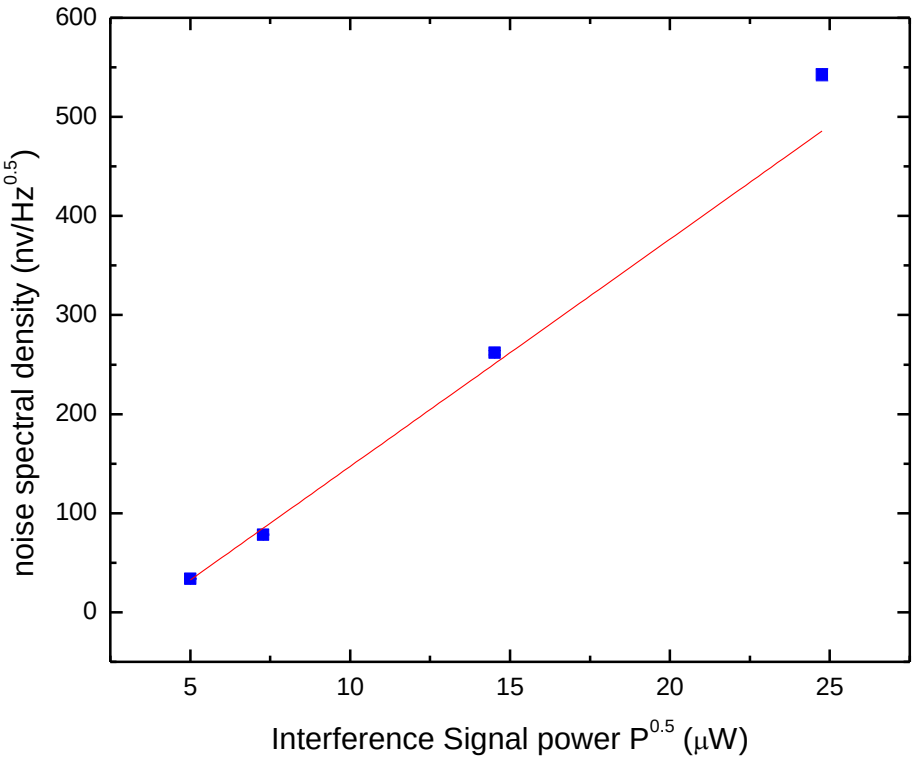


Figure 3- 28 The y-axis is white noise PSD (power spectral density) measured by SRS760 spectrum analyzer. The PSD is roughly linear with increasing $P^{0.5}$ as eq. 3-20.

From eq.3-19 and 3-20, the signal to noise ratio SNR is given by:

$$SNR \sim \frac{4\pi v \mathrm{P}_{\mathrm{efftive}} \frac{\Delta d}{\lambda}}{\sqrt{2e\eta P_{efftive}}} \propto 4\pi v \sqrt{\mathrm{P}_{\mathrm{efftive}}} \frac{\Delta d}{\lambda} \quad (3\text{-}21)$$

Therefore, SNR can be improved by increasing $\Delta d$ (the amplitude of cantilever), light source power as shown in figure 3-29 and by decreasing the wavelength of the light source. However, a large amplitude might introduces systematic error at short separation distances because of the uncertainty in frequency shift which we will discuss at chapter 5. Increasing the laser power and wavelength reduction can lead to increased heating in the cantilever. Also, when using a low spring constant and high vacuum like in our system, the light radiation can drive (heating) or damp (cooling) the cantilever. This will introduce another un-wanted force gradient in our system.

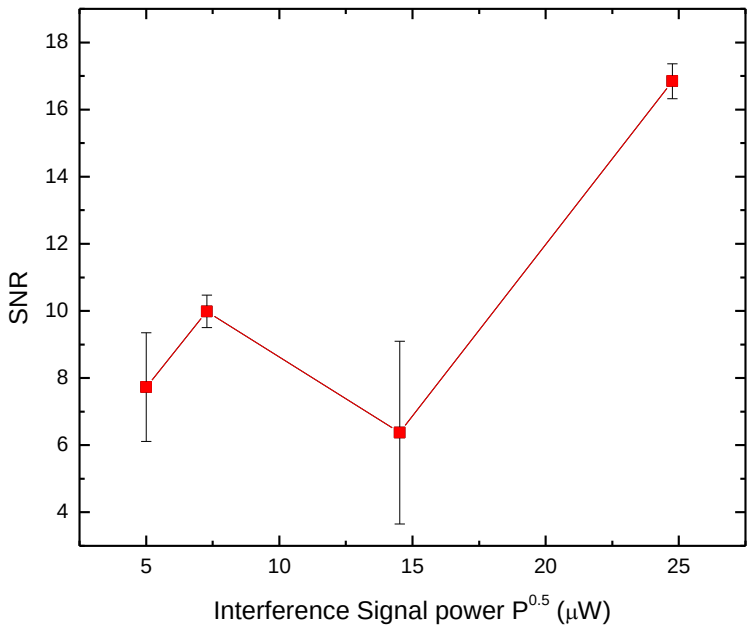

Figure 3- 29 SNR (thermal noise amplitude to shot noise (white noise level)) is roughly linearly with increasing $P^{0.5}$. The error might come from the un-wanted environmental vibration exciting the cantilever.

# Chapter4 Experimental arrangement for dynamic Casimir force measurements

## 4.1 Overview of experimental methods

The Casimir force is a strong nonlinear function of the separation distance between the two objects. The final precision of the Casimir force measurement is determined by how precisely you can measure the separation distance. Here, the experimental arrangements and methods for Casimir force measurement are presented graphically in figure 4-1. Basically, the first interferometer is used to monitor the cantilever motion and input the interference signal into two positive feedback loops where one is used for feedback (PID) control the separation distance between the fiber end and the cantilever, while the other one is used to generate the signal on the cantilever resonant frequency and also drive the cantilever . The second interferometer is used to precisely calibrate the sample movement which is driven by a ramp voltage provided by the high voltage power supply.

In our experiment, the Casimir force gradient is measured between a sphere and a plate. A sphere forms one surface because it provides easy alignment at each position compared to the case of two parallel plates which is hard to align. Therefore, we have to use proximity force approximation (PFA) to get the Casimir pressure between two plates from the gradient of the Casimir force between the sphere and the plate . We will also explain the PFA approximation in this chapter. The standard procedure we used to extract the Casimir pressure is through an electrostatic force calibration. We apply a known

potential difference between the Au-coated sphere and Au plate. For each applied potential difference, the frequency shift as a function of the sphere-plate separation is measured.

The parameters related to the cantilever and sample (k, $\omega_0$, R, and residual potential $V_0$), and the closest separation ($Z_0$) distance between sphere and plate can be extracted systematically using the shift in frequency with the applied electrostatic voltage. Using these parameters, the Casimir pressure can be determined . Note that all procedures related to the measurement is controlled by a lab-view program . In the following sections, details of the experimental process will be presented.

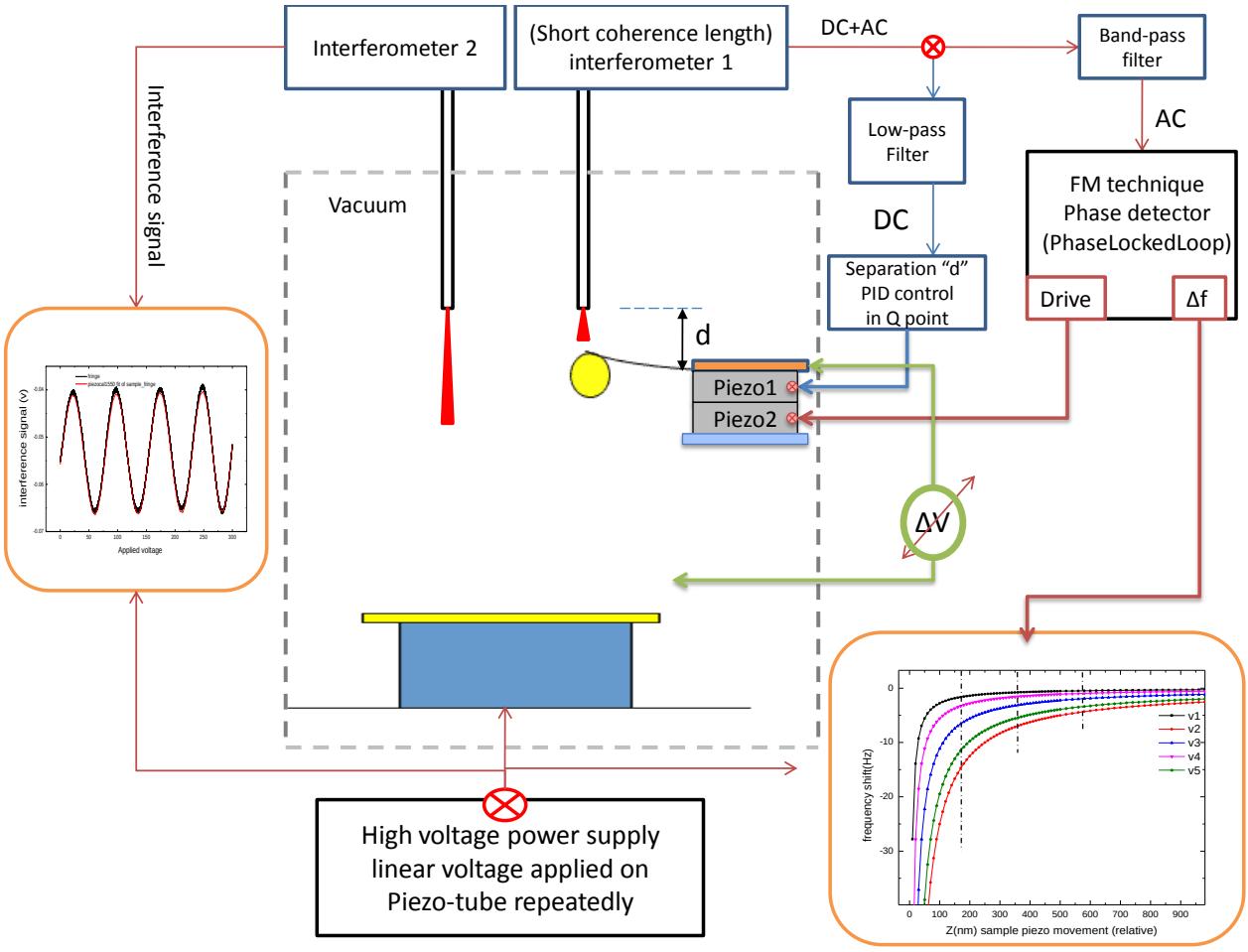


Figure 4- 1 Flow chart of dynamic Casimir force measurement technique used.

### 4.1.1 Calibration of piezo movement[22]

There are many ways to calibrate the movement of the piezo precisely. One of most precise and direct ways is to use the optical fiber interferometry technique. Our calibration of the movement of the piezo tube is determined by this technique. For precise Casimir force measurement, the piezo tube held under the sample plate is usually driven

with a periodic linear voltage (triangle wave of appropriate amplitude). The interference signal from the fiber and sample plate is varies with the displacement of piezo tube relative to the scale of voltage. To measure the expansion of the piezo leading to the displacement of the plate, we need to find the sensitivity coefficient P=ΔL/ΔV, which relates the piezo tube movement ΔL and voltage applied ΔV. Notice that for small scanning ranges the sensitivity coefficient is a constant. For large voltage ranges, the nonlinearities related to the magnitude, and polarity of the voltage and the frequency of applied voltage come from the effects of piezo tube hysteresis and creep. These nonlinearities will play an important role for precise measurement using the piezoelectric elements. As we saw in the previous section, the interference signal is given by:

$$P_{out} = P_{effective}(1 + \upsilon \cos(\frac{4\pi nd(V)}{\lambda}))$$

where, d is the length of the optical cavity. The d can be Taylor expanded to relate the sensitivity P to the applied voltage V. Therefore, the above equation can be modified as,

$$P_{out} = P_{effective}(1 + \upsilon\cos(\frac{4\pi}{\lambda}(P_1V + P_2V^2 + P_3V^3 + P_4V^4 + P_5V^5 + P_6V^6 + \cdots + \delta)) \quad (4\text{-}1)$$

$P_i$ are the coefficients corresponding to the exponents i of the voltage V and δ is the initial length of the cavity at V=0. Because the changes in the sensitivity are related to the applied voltage and frequency, we need to monitor the fringes during each scan. As the figure 4-1 shows, there are two fibers (interferometers) inside the chamber. One is used to monitor the cantilever, another is for sample piezo tube. Through simultaneously

monitoring each scan of piezo tube and using the least $\chi^2$ fit to obtain the $P_i$ , we can calibrate the piezo movement with sub-nanometer position resolution.

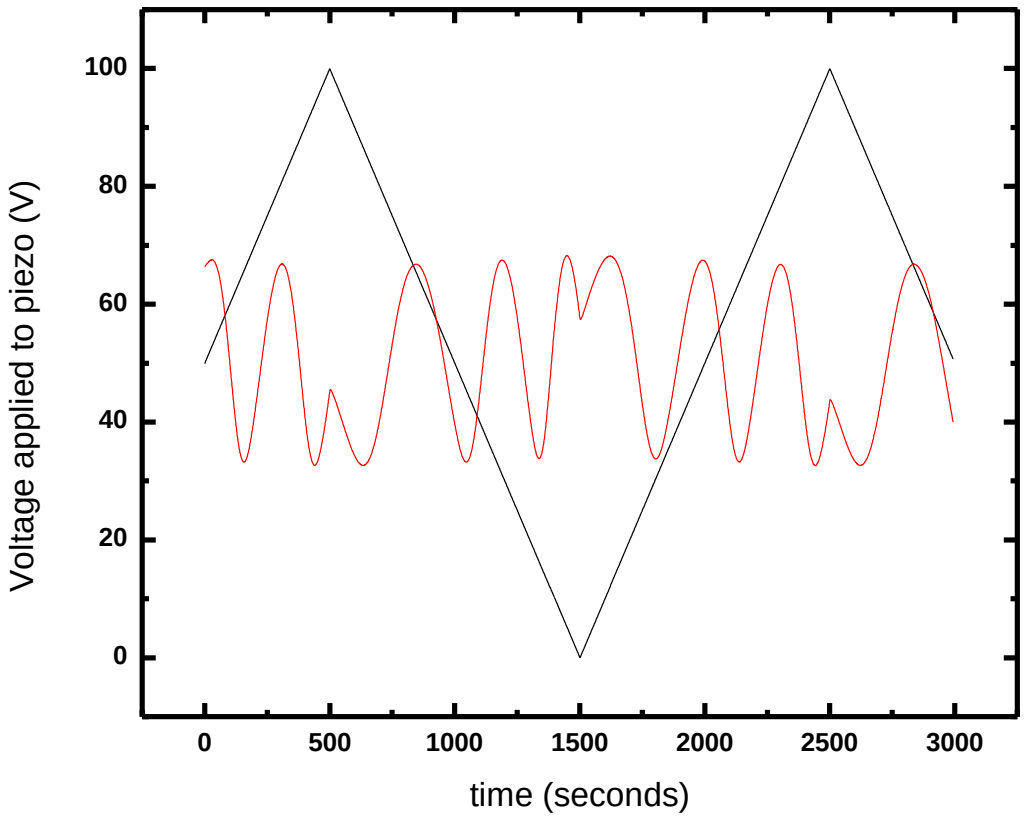


Figure 4- 2 The voltage applied (black line) on piezo is in the form of a triangular wave. The red line shows the corresponding interference signal from the reflection at the fiber facet and sample plate.

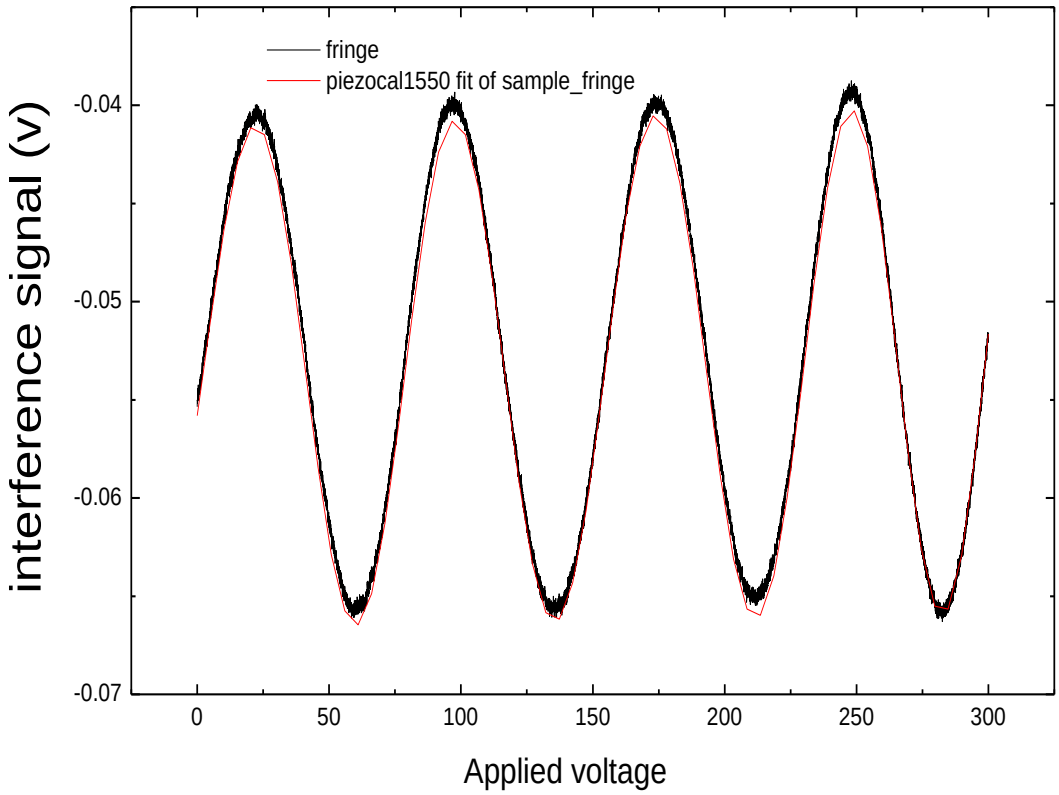


Figure 4- 3 The interference signal for the scanning range from 0 to 300 V. the black lines are experimental curve and the red line represents the least $\chi^2$ fit to the data by equation (4-1). The fit gives linear calibration value $P_1$~ 9.89 (nm/V) and first non-linear leading term $P_2$ ~ -0.159. For precise Casimir force measurement, we fit interference fringes to the tenth order term $P_{10}$.

### 4.1.2 Feedback loop control of separation distance between fiber end and cantilever

We used a feedback loop to keep (as shown in figure 4-3) a constant separation distance (d) between the fiber end and the cantilever. As we mentioned in chapter 3 , we would like to keep optical cavity length at the most sensitive operating point, "Q-point" as shown in figure 4-5.

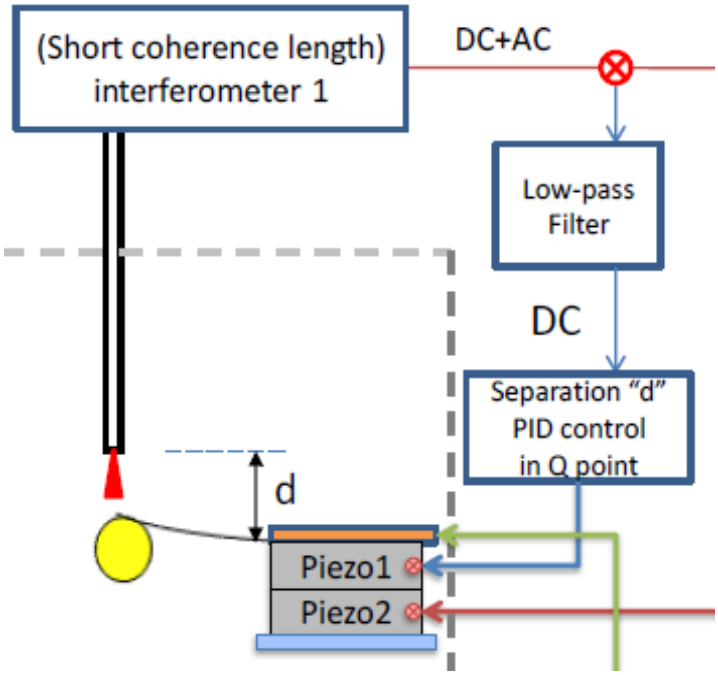


Figure 4- 4 Schematic of the feedback loop is used to control Piezo1 to keep a constant separation distance between fiber and cantilever.

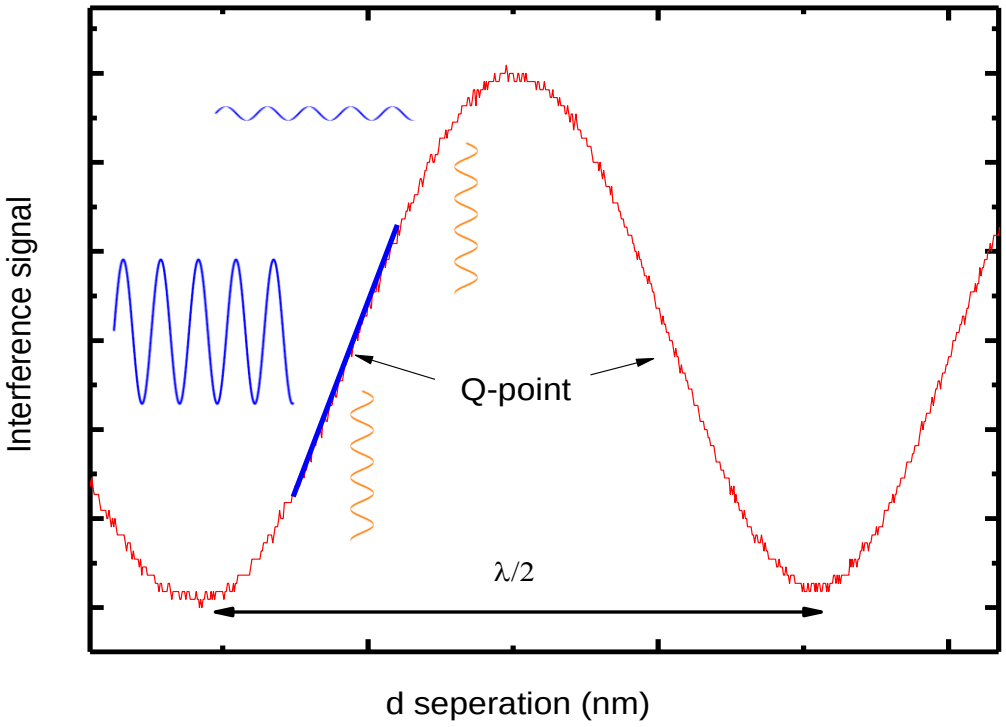


Figure 4- 5 The observed interference fringes versus optical sedations d. When we operate at the quadrature point, the vibration amplitude (orange curve) can be converted to large voltage signal (blue curve) to increase signal to noise ratio for the FM detection.

Another critical reason is that during the experiment , as the Au coated plate will be brought closer to the sphere on the cantilever, the force (electrostatic + Casimir) will cause the cantilever to bend. This is particularly an issue. Figure 4-6 illustrates the cantilever (k = 0.01N/m) deflection due to interactions which are electrostatic and Casimir force for the separation distances in our experiment at different voltage differences. It indicates the cantilever due to the Casimir force and electrostatic force (70mV) at 230 nm is ~4.882nm. The corresponding feedback voltage applied on the piezo to compensate the deflection of the is around 5nm shown as figure 4-7 (b).

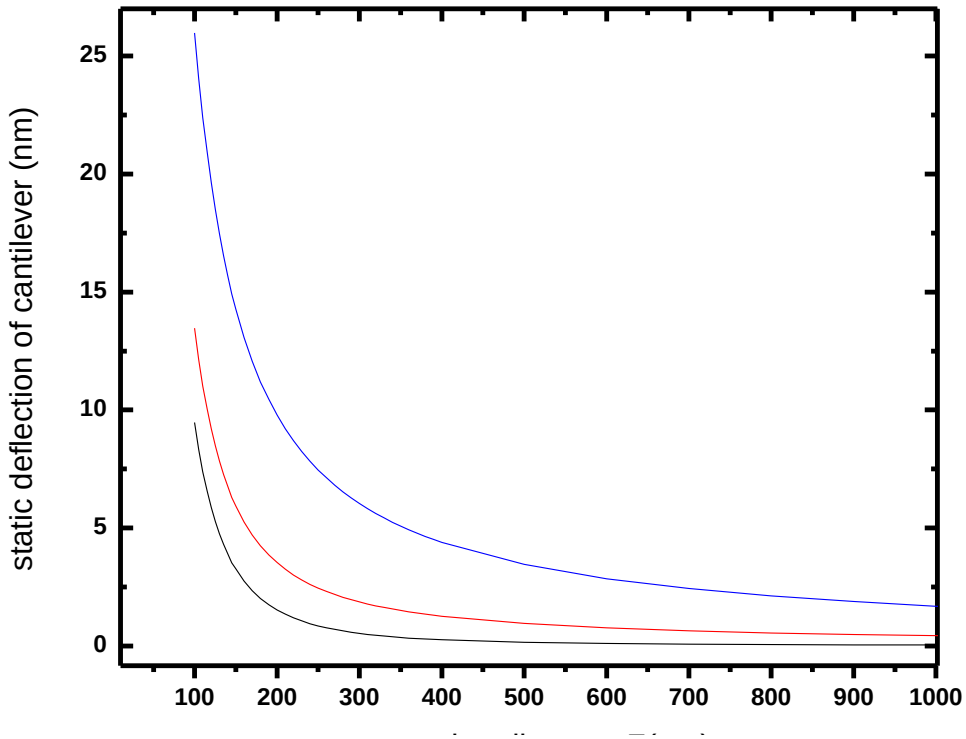


Figure 4- 6 The figure indicates the cantilever deflection due to the interaction between Au-coated sphere and Au-coated plate.

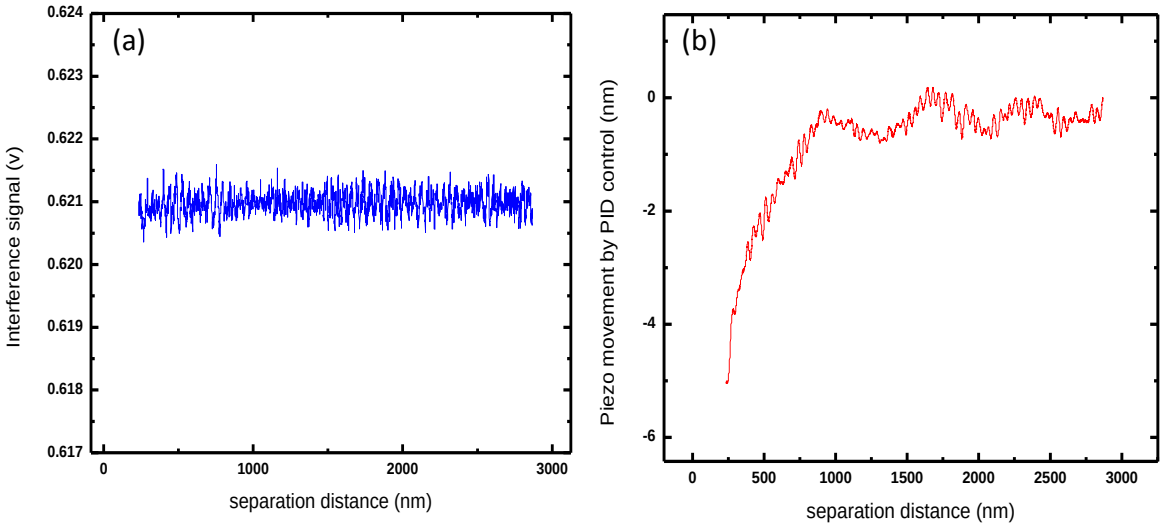

Figure 4- 7 In figure (a), interference signal is keep constant during each scan which indicates the separation between the fiber end and the cantilever is maintained constants by the PID feedback control. (b) The compensated movement by the piezo1 is ~5nm at 230 nm (70mV voltage difference).

### 4.1.2 Signal curve obtained from FM technique

As mention in chapter 3, the interaction force acting on cantilever causes a slight change in resonance frequency which is given by $\Delta\omega = \frac{\omega_0}{2k}\left(\frac{\partial F_{int}}{\partial z}\right)$. The frequency signal is measured by the FM detector and the cantilever oscillation is driven at the resonant frequency at a fixed amplitude by the FM controller. The frequency shift signal as a function of the sample movement is shown in figure 4-8.

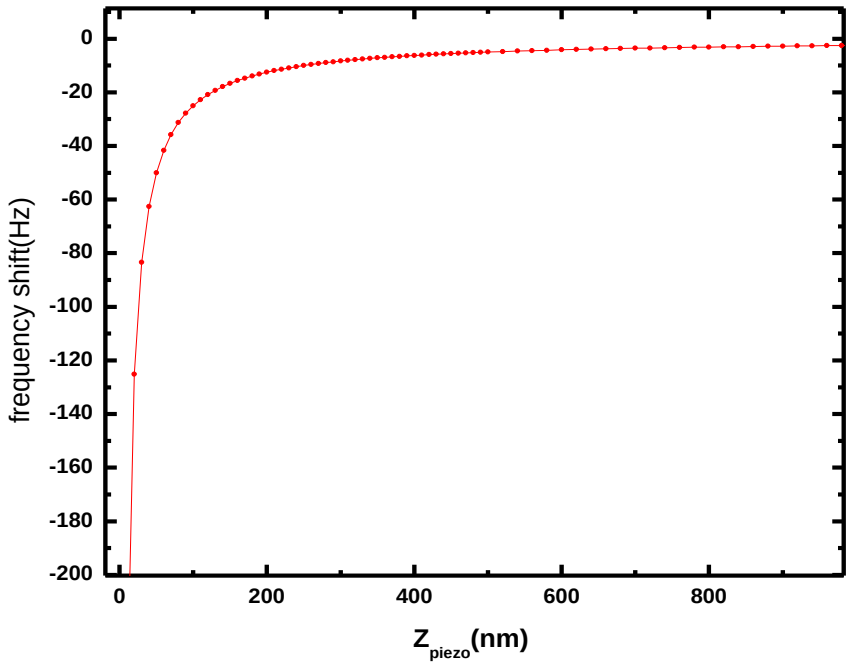


Figure 4- 8 Frequency shift as a function of the displacement of sample plate by the piezo $Z_{piezo}$.

## 4.2 Casimir Pressure Determination[10,25,53,54]

### 4.2.1 Casimir pressure using Proximity Force Approximation

Unlike the static measurement, in the dynamic measurement the Casimir force gradient $\frac{\partial F_{casimir}}{\partial z}$ is measured using $\Delta\omega = \frac{\omega_0}{2\mathrm{k}}\left(\frac{\partial \mathrm{F}}{\partial z}\right)$ by observing the change in the resonant frequency as a as a function of the separation distance between the sphere and plate. We use PFA to derive Casimir pressure (Casimir energy between two plates per unit area) from the force gradient in the sphere-plate configuration.

The basic idea of the PFA is that we can cut the sphere surface into infinitesimal small regions and integrate each piece for calculating Casimir energy. The proximity energy is $V_P = \iint E(D)d\sigma + corrections$. Here E(D) represents the Casimir energy per unit area of two parallel ideal metal plate at the separation D. The integral is over the area of the gap which is equivalently surface of the sphere.. The separation distance from a point on the flat region of the sphere to the plate can also be written as $D(x,y) = z + R(1-\cos\theta)$ and the area as $d\sigma = 2\pi R\sin\theta R d\theta$. Therefore, the proximity energy can be transformed to:

$$V_P(z) = \iint dxdyE(D) == 2\pi R\int E(z+R-R\cos\theta)R\sin\theta d\theta = 2\pi R\int_z^{z+R} dDE(D).$$

If $R >> z$, and E(D) approaches zero sufficiently rapidly for large values of R, the upper limit of the integral can be replaced by infinity. $V_P(z) = 2\pi R\int_z^\infty dDE(D)$. The Casimir force, which is given by the derivative of the energy between the sphere and plate is given by:

$$F_{casimir}(z) = -(\partial V_P / \partial z) = 2\pi RE(D). \quad (4\text{-}1)$$

Differentiating eq. (4-1) with respect to z one obtains

$$\frac{-\partial F_{casimir}}{\partial z} = 2\pi \mathrm{RP}_{\mathrm{casimir}}(z) \quad (4\text{-}2)$$

Thus, the Casimir force gradient between the sphere and plate can be directly related to the Casimir pressure between infinite parallel plates.

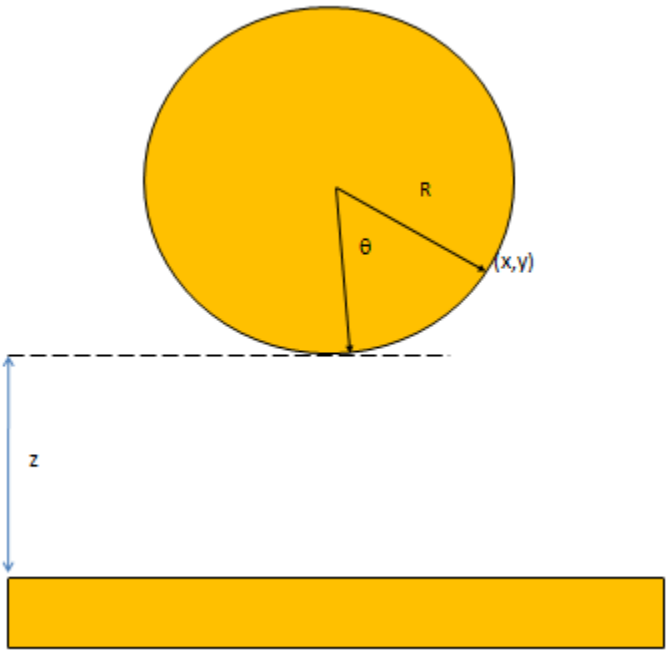


Figure 4- 9 Configuration of a sphere above a plate

The precision of the Casimir force from the Proximate Force approximation in our experiment with the sphere of the radius of 60 um and the closest separation 200 nm is smaller than 0.1%.

### 4.2.2 Electrostatic calibration

The electrostatic force between a sphere and plate is given by[55]:

$$F_{ele} = 2\pi\varepsilon_0(V - V_0)^2 \sum_{n=1}^{\infty} \cosh^{-1} n\alpha \,(\coth\alpha - n\coth n\alpha) \quad (4\text{-}3)$$

where V and $V_0$ are applied voltage on the plate and the residual voltage between the sphere and plate respectively. $\alpha = \coth^{-1}[1 + {}^{Z}/_{R}]$. Z $=Z_0 + Z_{piezo}$ is a separation distance between sphere and plate. $Z_0$ is the closest distance between sphere and plate. $Z_{piezo}$ is the plate movement due to the piezo which is calibrated interferometrically in the previous section. R is radius of the Au-coated sphere. Recalling eq.3-3 $\omega(z_0) - \omega_0 = \frac{\omega_0}{2k}\left(\frac{\partial F_{int}}{\partial z}\right)_{z=z_0}$, where $F_{int}$ represents the interaction force including Casimir and electrostatic force. According to PFA, eq.3-3 and 4-3, the frequency shift can be presented as the first derivative of the Casimir force and the electrostatic force. The equation is given by

$$\Delta\omega = \beta(Z, k, \omega_0, R)(V - V_0)^2 + C(k, \omega_0, R)\frac{\partial F_{Casimir}}{\partial z} \quad (4\text{-}4)$$

where $\beta(Z, k, \omega_0, R)$ is associated with the first derivative of eq. 4-3 and $C(k, \omega_0, R)$ which is related to parameters such as the spring constant k, resonant frequency $\omega_0$ and sphere radius R. To provide those parameters, we apply a series of known potential differences between the sphere and plate. The frequency shift as a function of the plate movement for the different applied potentials to the plate are shown in figure 4-10.

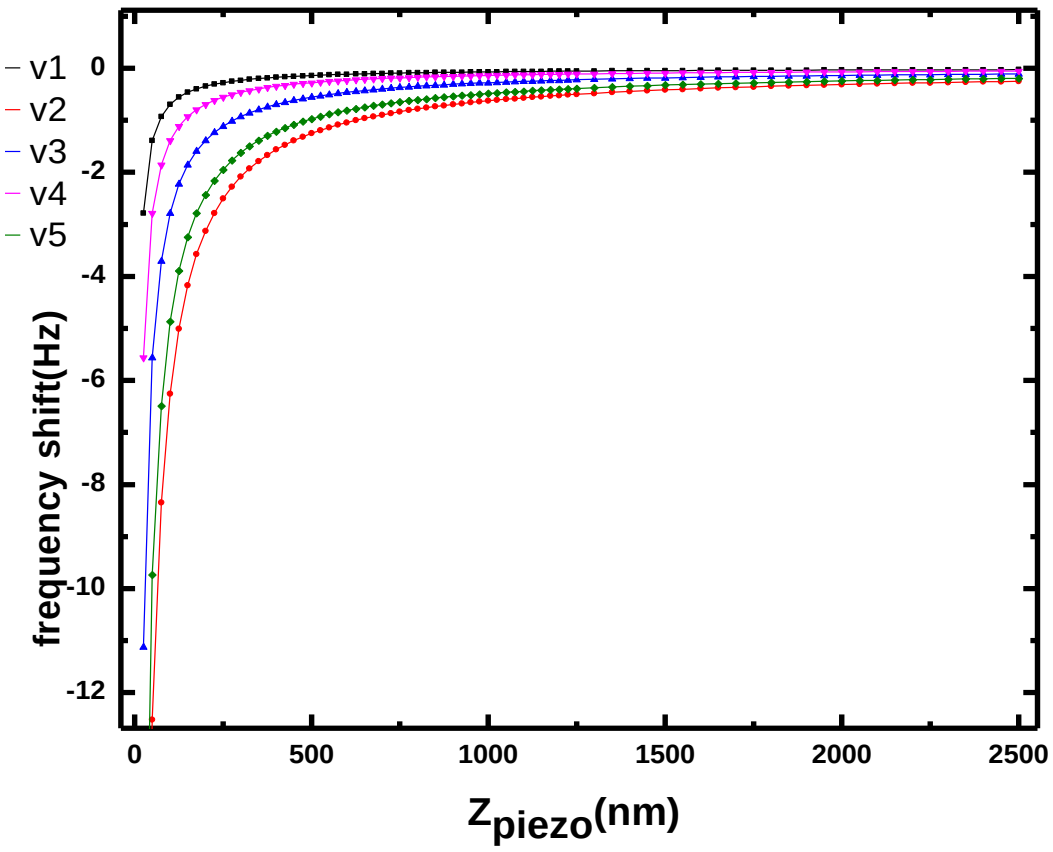


Figure 4- 10 Frequency shift as a function of plate movement for different voltages applied to the plate. In our experiments, we applied 13 different voltages at each piezo scan.

We apply 13 different potential differences. For a fixed $Z_{piezo}$ based on eq.4-3., the electrostatic force, the force gradient and therefore the frequency shift has a parabola dependence on the voltage $V_{applied}$ applied to the plate. This is shown in figure 4-11. From equation 4-4, the maximum in the frequency shift corresponds to $V_0$ (residual potential between sphere and plate and the offset from the zero level to associated $C(k, \omega_0, R) \frac{\partial F_{Casimir}}{\partial z}$ . The curvature of the parabola which includes the spatial dependence of the electrostatic force and the cantilever parameters is denoted by $\beta(Z, k, \omega_0, R)$ . The coefficient $C(k, \omega_0, R)$ which contains the cantilever spring constant, resonant frequency and the sphere radius can be obtained from $\beta(Z, k, \omega_0, R)$ to its theoretical expression :

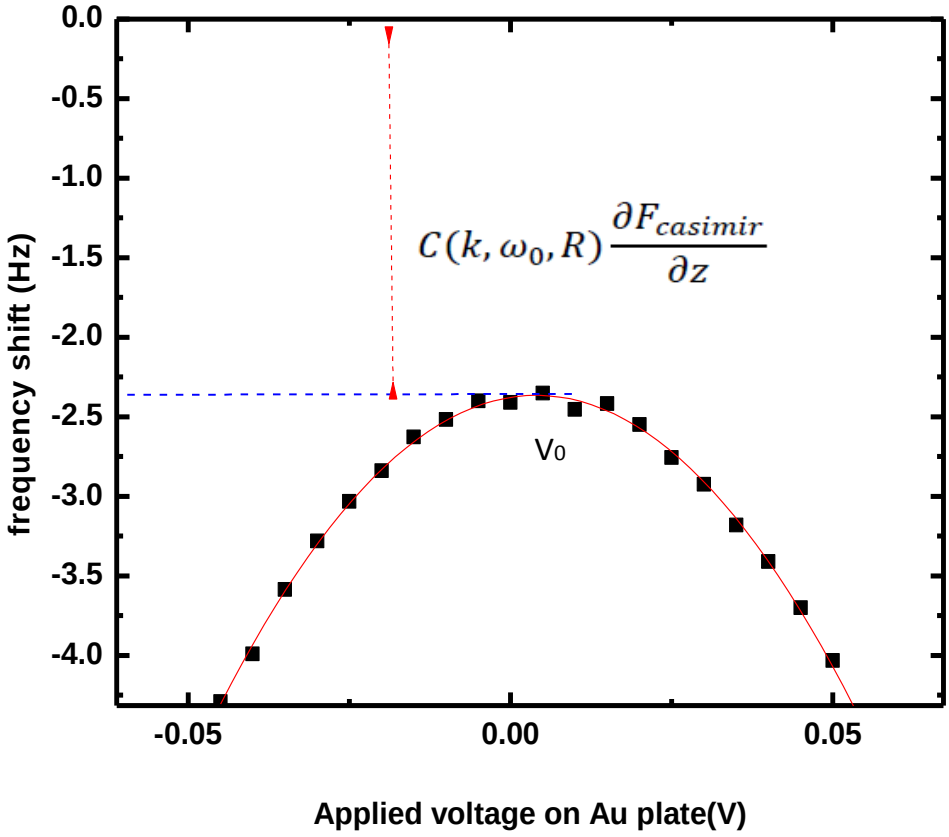


Figure 4- 11 Dependence of the resonant frequency shift as a function of the applied voltage on the plate. $V_0$ is given by the maximum in the parabola. The offset of the parabola maximum from the zero value is proportional to the gradient of the Casimir force as shown with the red dashed line.

### 4.2.3 Closest separation distance determination ($Z_0$)

As mentioned in the previous section, $\beta(Z, k, \omega_0, R)$ is associated with the first z-derivative of the electrostatic force coefficient which is given by

$$\beta = \frac{\omega_0}{2k} \cdot 2\pi\varepsilon_0\left[\frac{-R}{2Z^2} + 22.2375\left(\frac{1}{R}\right) - 571.366\left(\frac{2Z}{R^2}\right) + .. o(high\ order\ terms)\right] \quad (4\text{-}5)$$

where $Z = Z_0 + Z_{piezo}$. From the parabolas at each Z the $\beta(Z, k, \omega_0, R)$ is obtained. In Figure 4.12 (you have to be consistent and used Figure or figure or Fig) the $\beta$ is shown in black with error bars as function of the distance moved by the plate, $Z_{piezo}$. The red solid line in Fig.4-12 shows the best $\chi^2$ fit to fourth order term of eq.4-5 for the measured $\beta(Z, k, \omega_0, R)$ with the two unknown $Z_0$ and $C = \frac{\omega_0 R}{k}$ which are to be determined from the fit. In order to test for systematic errors in of the fitting parameters, the $\beta$ fitting is repeated at the different Z distance ranges . For example, we fix one end of the range to the sphere-plate closest distance and the other end is changed from 1200nm to 300 nm.

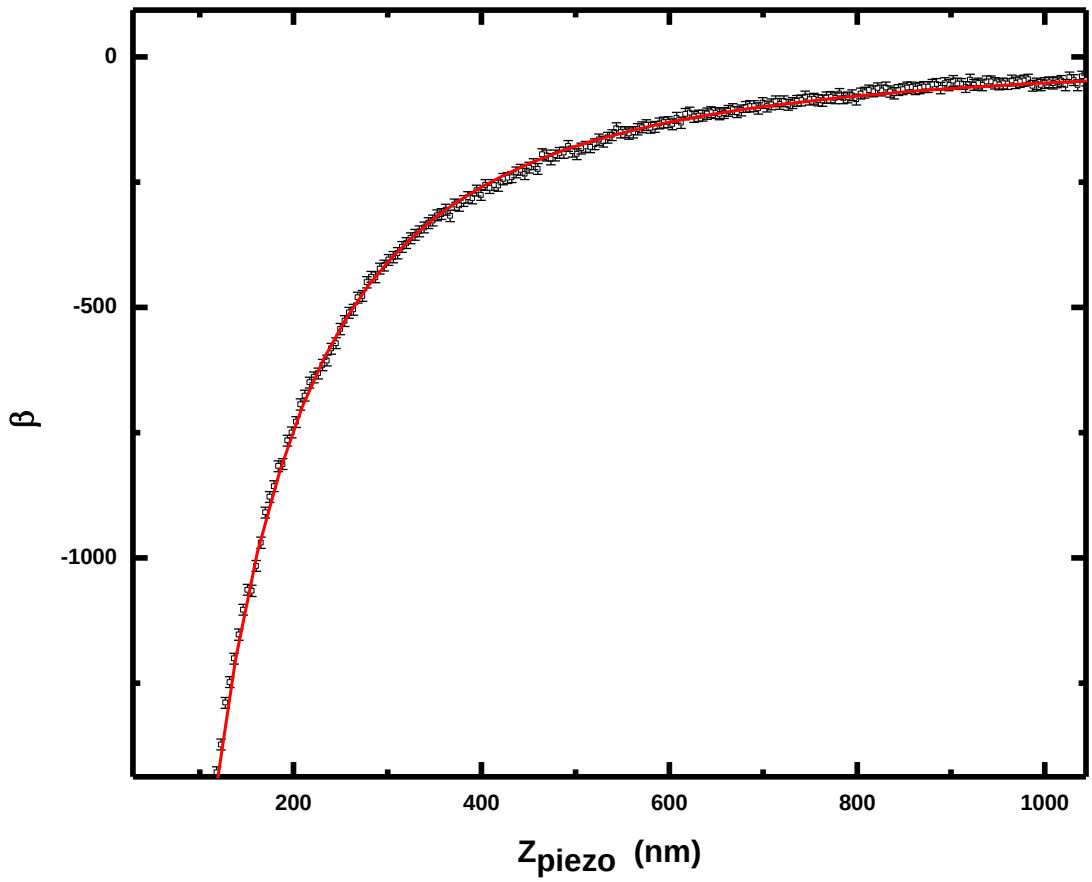


Figure 4- 12 The $\beta(Z, k, \omega_0, R)$ as a function of distance moved by the plate, $Z_{piezo}$. The data points in black includes error bar and represents the experimental determining symbol beta . The red solid line is the best indicates the best $\chi^2$ fit.

### 4.2.3 Electrostatic fringe field effect from fiber

Because the dynamic measurement is very sensitive, any small force interacting with cantilever will lead to a frequency shift. Here, we observed the effect of the fringe fields from the voltage applied to the plate which affects the charge distribution at the surface of fiber as shown in figure 4-13. It induces a small electrostatic force between fiber and cantilever as shown in blue line.

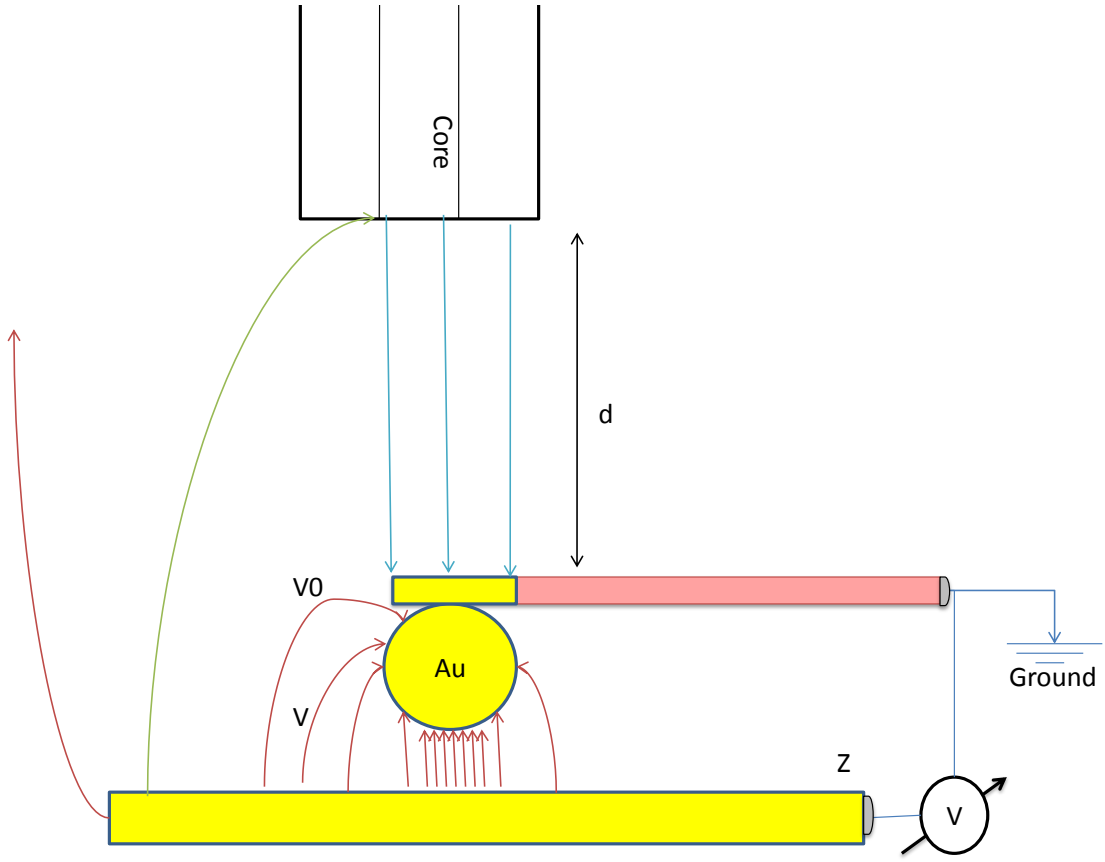


Figure 4- 13 In this figure, the fringe fields (green solid line) due to voltage applied on the plate affects the charge distribution on the fiber surface. The charge distribution induces an electrostatic force due to image charge from cantilever. The density of red lines due to electric fields between sphere and plate is much higher than blue line induced

by fiber which represents the electrostatic force between sphere and plate is dominated comparing to fiber effects.

We can prove experimentally and theoretically that the electrostatic force between fiber and cantilever is independent of sphere-plate separation distance Z as shown in figure 4-14. Hence, this force can be subtracted out from $\beta$ curve as shown in Figure 4-15 . In Figure 4-15 the frequency shift of the cantilever is shown for large voltages applied to the plate for three different sphere-plate separations .In order to able to observe electrostatic force due to fringes fields, we need to apply high voltages to the plate The voltage applied is two orders of magnitude larger than the usual voltage applied during the Casimir force measurement. As can be seen the frequency shifts are independent of the separation distance, pointing to the role of the fringe fields. From the curvature of the parabolas in Figure 4-15, the $\beta$ from the fringe fields can be measured to be -7.09 . This value is subtracted from that to obtained earlier as a function of the sphere-plate separation to eliminate the role of the fringe fields in the experiment. The role of the fringe fields can be further confirmed from Figure 4-16 where the frequency shift from applying voltages to the plate is plotted as a function of the distance moved by the plate. The insets show the parabolas generated at the different sphere-plate separations.

As expected from Figure 4.15, at large separation distances, the parabola curvatures become asymptotically constant due to the effect of the fringe fields. This asymptotic value can be subtracted to eliminate the effect of the fringe fields.

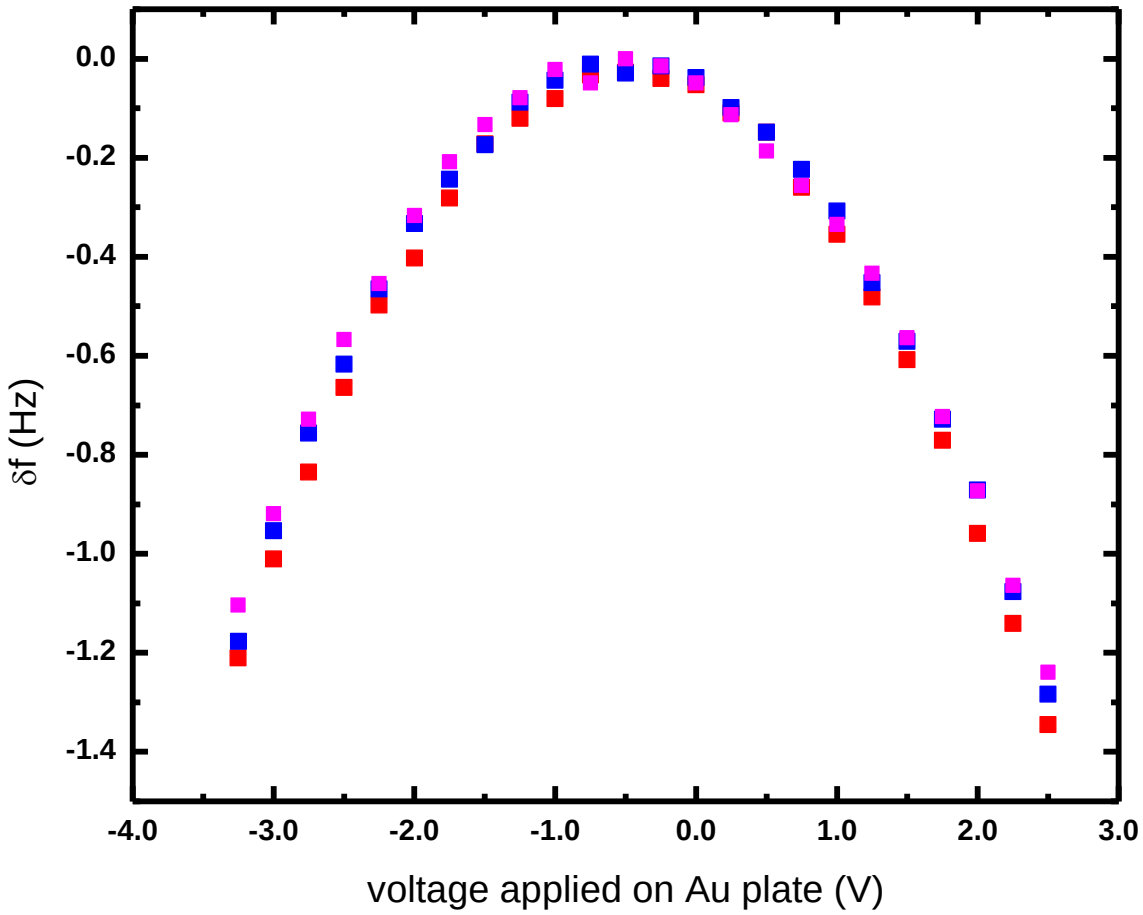


Figure 4- 14 . The red, blue and pink square dot indicate frequency shift versus applied voltage on plate at large plate-sphere separation distances ~3.2m, 4.4 and 5.6 ,respectively.

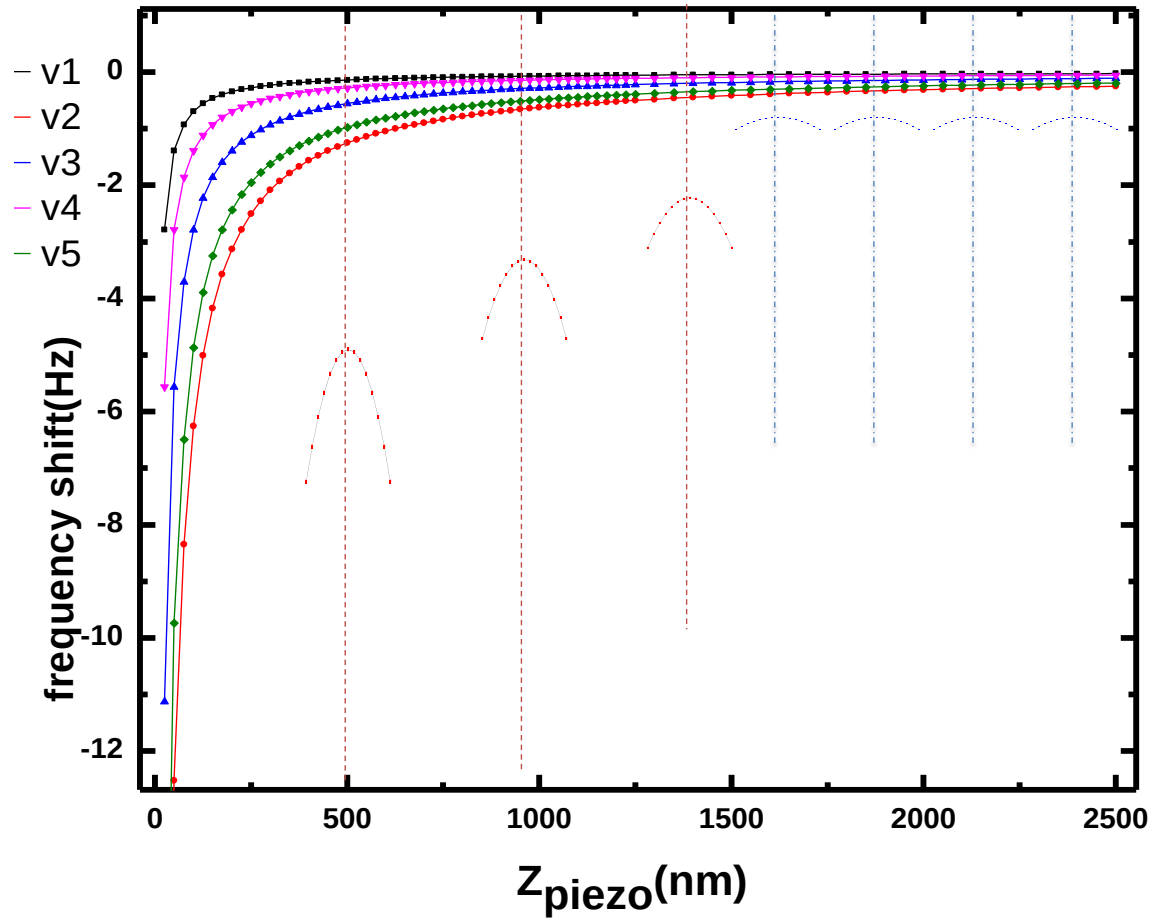


Figure 4- 15 The frequency shift for various applied voltages to the plate as a function of the distance moved by the plate. The corresponding parabolas at fixed separation distance are shown in the inset. The parabolas at large sphere-plate separation distances are seen to asymptotically tend to a constant value as expected from the effect of fringe fields.

# Chapter5 Experimental results and Theory[54]

## 5.1 Experimental results and Error budget

In Casimir force measurement, electrostatic calibration plays an important role. It allows precise determination of basic quantities such as absolute separation distance, spring constant, radius of the sphere and the residual potential as mentioned in Chapter 4. Because of this, any inaccuracy in the electric force used in the calibration will introduce additional systematic errors. Here, we present an unambiguous dataset with 3 runs from 200nm to ~1500nm calibrated by fitting the electrostatic force.

### ➢ Residual potential $V_0$

According to equation 4-4, $V_0$ comes from the fitting curve of the x coordinate of the maxima in the parabola at different separation distances. The $V_0$ plotted in figure 5-1 indicates it is independent of separation distance from 200nm to 1400nm. The $V_0$ is equal to a constant which is an indirect confirmation of the fact that the interacting regions of the surfaces are clean or the adsorbed impurities are randomly distributed with a sub-micrometer length scales.

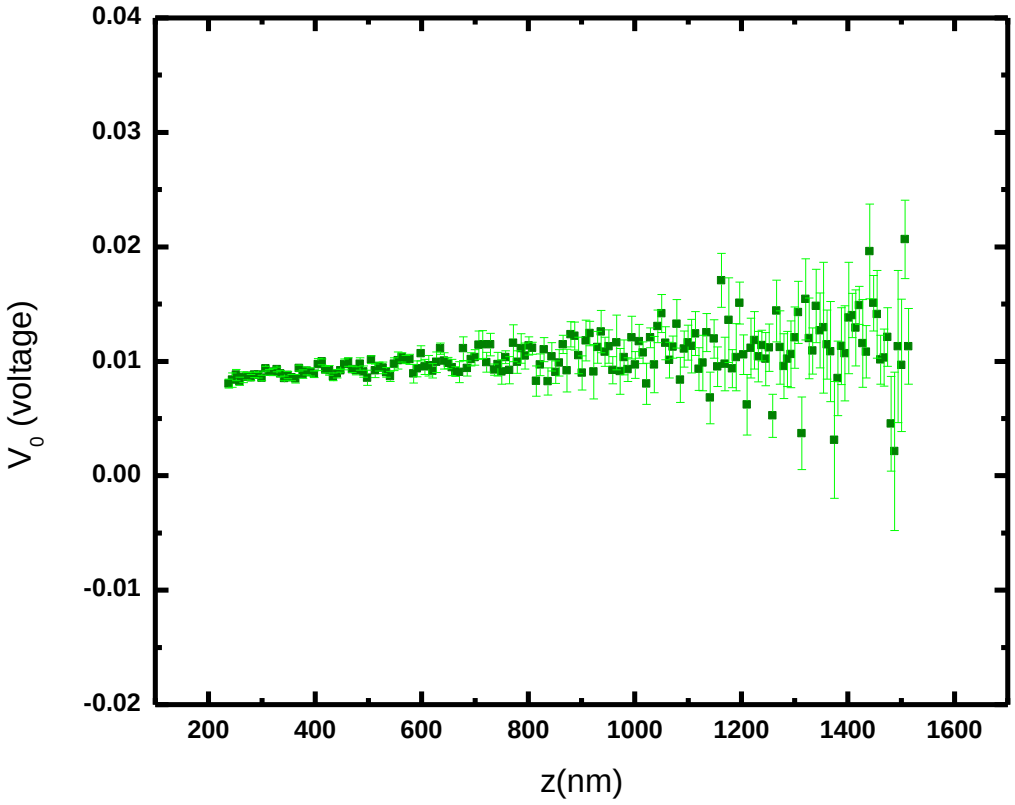


Figure 5- 1 Electrostatic results for the residual potential $V_0$ as a function of separations are shown in olive dots with error bars (green). The olive square dots indicate the residual potential between Au-coated plate and Au-coated sphere at $V_0$=10.86mV± 1.28 mV (one run data with 10 points reduction).

## ➢ Closest separation distance on sphere-plate approach $Z_0$

As discussed in the previous chapter, the absolute separation $Z=Z_{piezo}+Z_0$ needs the independent determination of the closest separation distance on sphere-plate approach $Z_0$. This and the other parameters associated with the cantilever such as the spring constant can be calibrated from beta value $\beta(Z, k, \omega_0, R)$ (parabola curvature of the electrostatic

force as a function of the applied voltage) determined at each separation. In fitting $\beta(Z, k, \omega_0, R)$ to the electrostatic force formula in eq. 4-5, the endpoint is kept fixed and the initial point is varied. In figure 5-2, $Z_0$ so determined is shown as a function of the initial point used in the fit. The values of $Z_0$ are seen to be independent of the start position indicating the absence of systematic errors resulting from $Z_{piezo}$ calibration, mechanical drift etc. in the experiment.

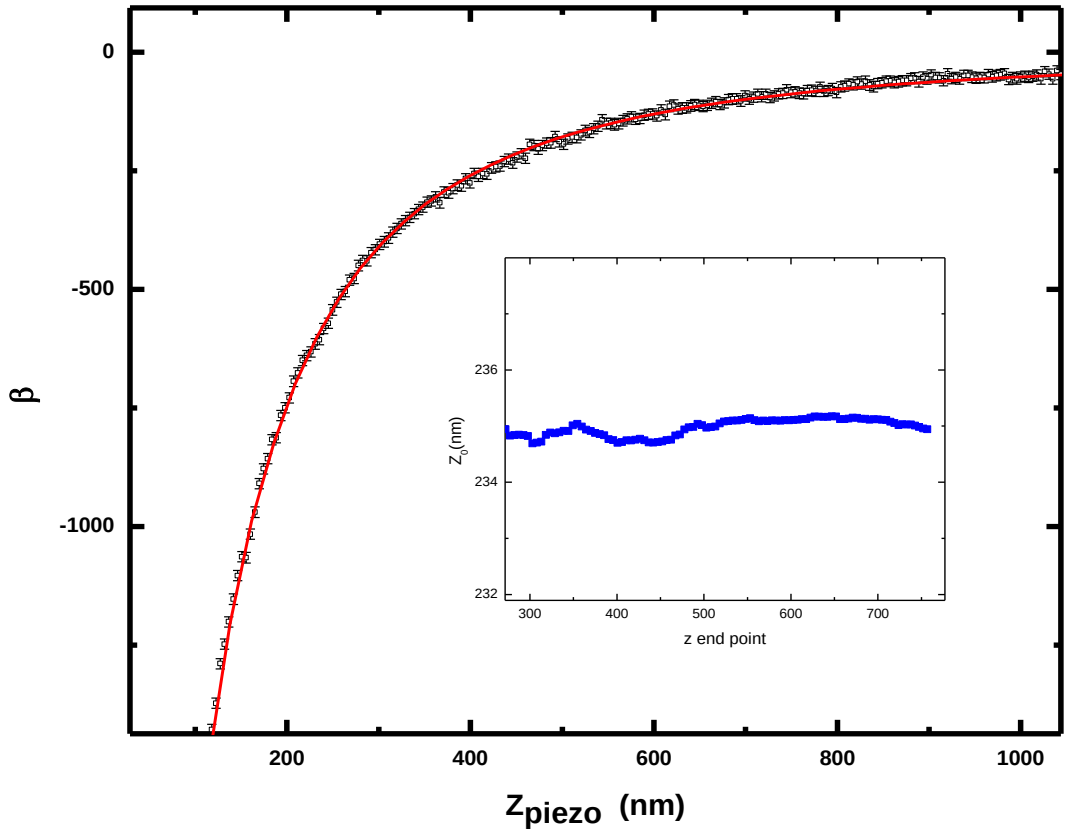


Figure 5- 2 The black line represent the data of the beta curve as function of sample movement. The red line is best $\chi^2$ fit curve of the coefficient of the electrostatic force eq. 5-2. In the inset, the blue line indicates $Z_0$ values obtained from the fit as function of the end point of the fit with different fitting range (during the fit the point of closest

separation is kept fixed and the last point is varied) . The average value (from region as blue line shown) is $Z_0 \approx 235.0 \pm 0.4$nm (one run data).

## ➢ Other calibration parameters ($k, \omega_0, R$ ) associated with sensor

The constant $C(k, \omega_0, R)$ can be also extracted by fitting the beta curve as a function of separation. The fit done using different regions similar to that for $Z_0$ by keeping the point of closest approach fixed and varying the endpoint to different Z is shown in figure 5-3. The flat line indicates the absence of systematic errors. Because we have three runs of $C(k, \omega_0, R)$ curve as separation distance, the average of $C(k, \omega_0, R) = 7.0922 \pm 0.037$ ($LTM^{-1}$) from the three runs. The parameters of each run are listed in Table 5-1.

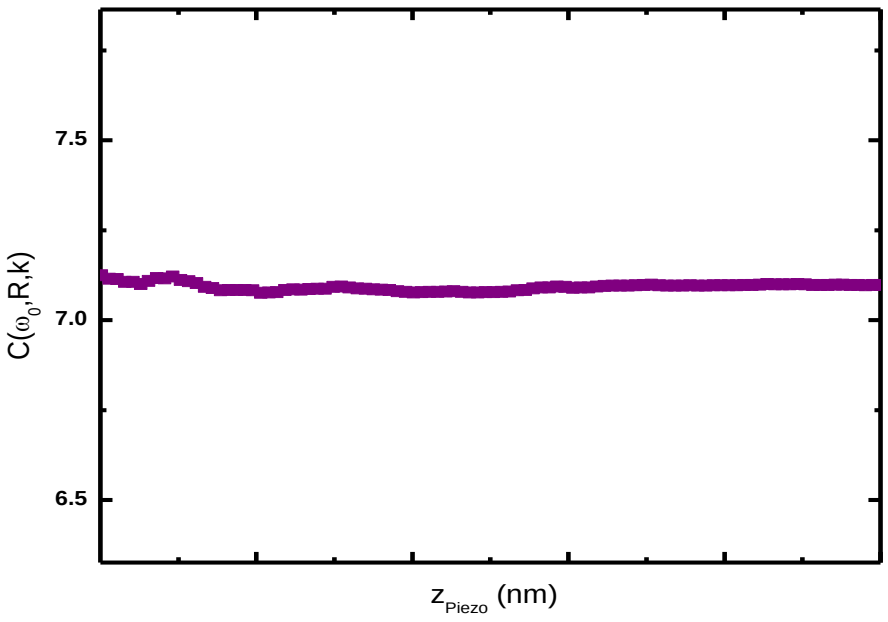


Figure 5- 3 The values of $C(k, \omega_0, R)$ obtained from fitting the beta curves in the same way as $Z_0$. The value of $C(k, \omega_0, R)$ is independent of separation indicating the absence of systematic errors during the duration of the experiment.

## ➢ Measure Casimir Pressure and Error budget

The Casimir pressure for the parallel plate is given by:

$$P^{Casimir}(z+z_0)=\left(\frac{-1}{\pi C(k,\omega_0,R)}\right)\frac{\partial F_{casimir}}{\partial(z+z_0)} \quad (5\text{-}1)$$

All parameters used for the Casimir pressure are calibrated from the electrostatic force as shown in table 5-1. The mean value of the Casimir pressure measured with the dynamic technique is shown in figure 5-4 as a function of the separation. Three different experiments are averaged to obtain the mean value of the Casimir pressure. The separation distance ranges from 230nm to 1400 nm.

| | **Run 1** | **Run 2** | **Run 3** |
|---|---|---|---|
| **$Z_0$ (nm)** | 235.09 ± 0.41 nm | 233.58 ± 0.37 nm | 234.98 ± 0.38 nm |
| **$C=\frac{\omega_0 R}{k}$ ($LTM^{-1}$)** | 6.9690 ± 0.0172 | 7.0668 ± 0.0194 | 7.0922 ± 0.0167 |
| **$V_0$ (mV)** | 10.47 ± 1.28mV | 10.12 ± 1.33 mV | 10.86 ±1.36 mV |

Table 5- 1 It indicates parameters which are calibrated from the electrostatic force for three different datasets. The errors including random errors and systematic ones for each parameters was extracted from fitting curve.

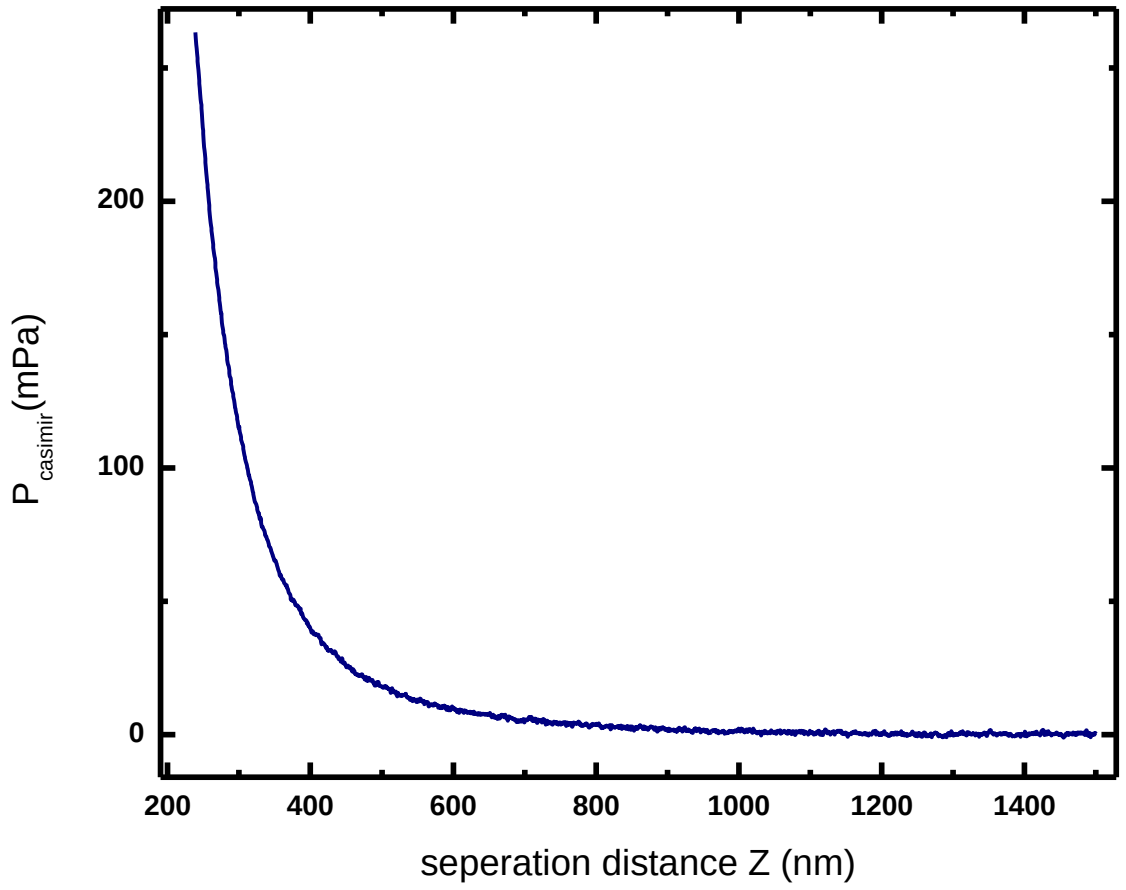


Figure 5- 4 Measure Casimir pressure between Au plate and Au sphere as a function of separation distance. The mean value of three different pressure measurement is plotted.

The following standard random error analysis of our experiment is based on 3 data sets. In the Gaussian normal distribution, random error can be presented as $\sigma/\sqrt{n}$ where σ is standard deviation from an average of n=3 runs of Casimir pressure. . The

mean value of standard random error of the pressure measurements is calculated to be 0.5mPa.

The systematic errors are usually used with two different definitions. the first meaning is some bias in a measurement which always makes the measured value higher or lower than the true value. Such errors in our measurement can be excluded by calibration (the subtraction due to fringes field background) or experimental set-up. For example, in chapter 4, the cantilever's bending due to interaction between sphere and plate is one of the systematic errors. it can be solved by feedback loop controlled by PID circuit. Therefore, in the following section, the systematic error is assumed that the experimental data under consideration are already free of such affection.

Another systematic error[54] which is the errors of a calibrated measurement system. The errors of a theoretical formula used to convert a directly measured quantity into an indirectly measured one. they are determined by the minimum frequency shift that we can be measured and other parameters which are calibrated by electrostatic force. In our detection system, the main frequency noise of 35mHz is determined by the shot noise level as we mentioned in chapter 3. Next, the fitting errors from the parameters $C(k, \omega_0, R)$ need to be considered. The relative error of the Casimir pressure can be used for the error propagation from eq. 5-1.

Because $C(k, \omega_0, R)$ and frequency noise δω are uncorrelated, the form of relative error in the Casimir pressure is given by:

$$\frac{\delta P(Z)}{P(Z)} = \frac{1}{\pi}\sqrt{(\frac{\delta C}{C})^2 + (\frac{\delta f}{f})^2}$$

where $C = 7.0427 \pm 0.0376$ coming from average out 3 runs data and $\delta f$ is 35mHz. Hence the systematic error varies from 2mPa at z=230nm to 1.5mPa at all separations when Z > 400nm. In figure 5-5, we show the systematic and random error with the black line and red bars, respectively. It indicates that the random error in our detection system is smaller than systematic error.

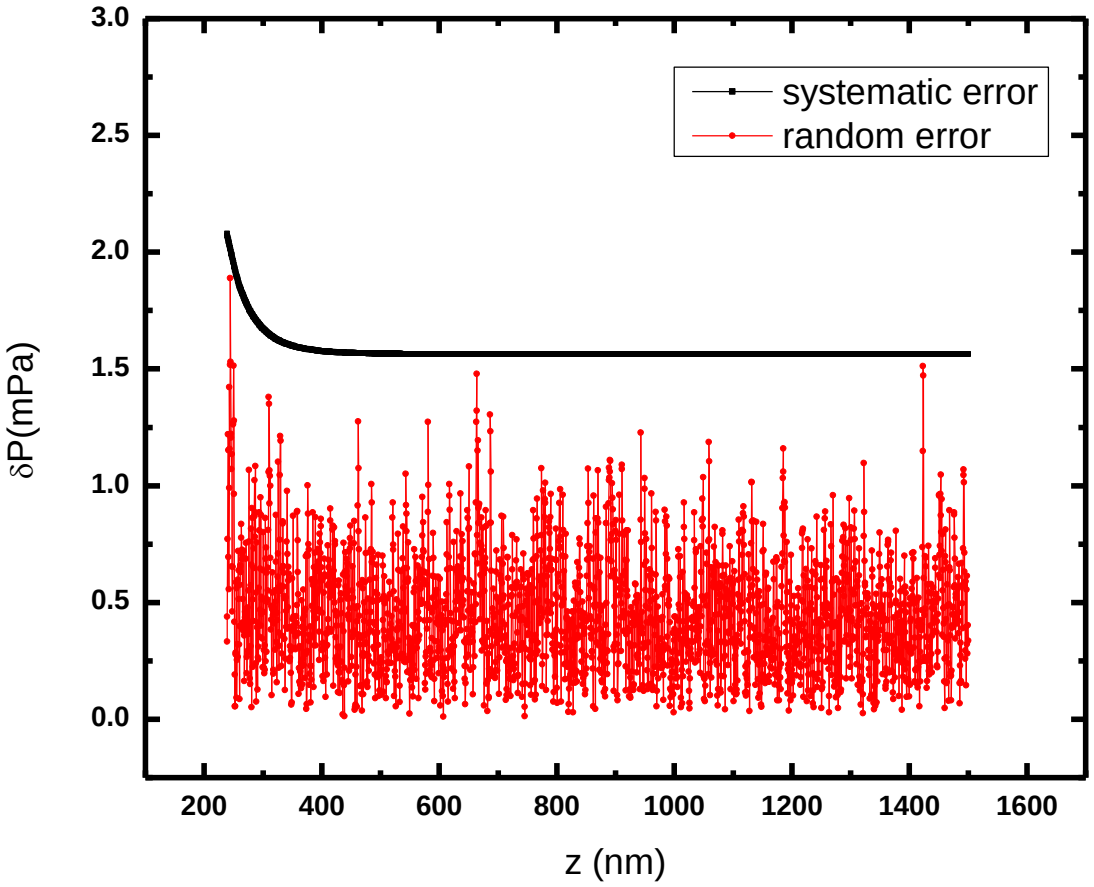


Figure 5- 5 The red bars and the solid black line represent the random and systematic errors in the experiment respectively as a function of the plate-sphere separation.

# 5.2 Comparison of experiment with theory

## 5.2.1 Theory

- **Roughness corrections**

The Casimir force at small separations depends sensitively on the profile of the surface roughness as we mentioned in chapter 2. Even though it is a very small effect in this experiment, the surface roughness should be analyzed and characterized. The roughness amplitude was investigated using an AFM system as shown in Fig.5-6.

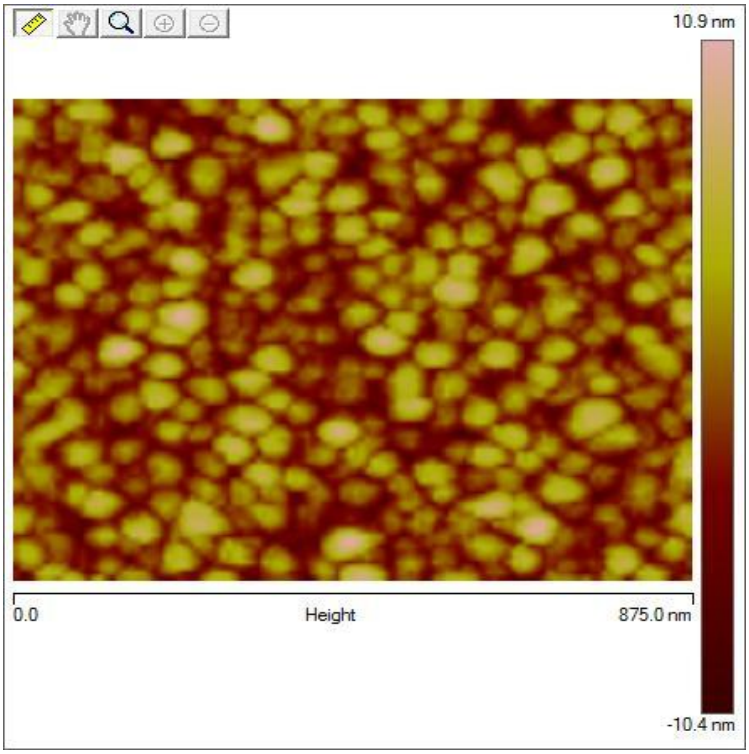


Figure 5- 6 The topography of the Au layer on the silica sphere is measured by taping mode in Air.

The roughness amplitude of the Au-coated sphere is 1.94nm and that for the Au layer on the sapphire is ~ 2.74nm. The roughness corrections due to these two average amplitudes are < 0.1% of the Casimir pressure at 200nm. It is negligible when comparing theory to the experimental data.

### ➢ Finite conductivity and finite temperature correction

As described in Chapter 2, for real metals, the Casimir pressure depends strongly on the model of the dielectric permittivity. Here, we apply two different models (Plasma and Drude models) of the dielectric function to the Lifshitz equations. Both models consider the case of the free electrons. In the Drude model, we take the energy dissipation into account which can be seen in the relaxation frequency $\gamma$ of the electrons. However, both the Plasma and Drude model disregard important physical processes determined by inter-band transitions of core electrons. Hence, for taking more high frequency response terms due to the core electrons, we would like to use the generalized Plasma-like model and generalized Drude-like model to compare our experimental data.

### ❖ Generalized Drude-like model

The basic idea is to obtain the dielectric permittivity along the imaginary frequency axis $\varepsilon(i\xi)$ (dielectric function) by using the Kramers-Kronig relation through the fitting tabulated optical data for $Im\varepsilon(\omega)$ where $Im\varepsilon(\omega) = 2n(\omega)k(\omega)$. $n(\omega)$and $k(\omega)$ are the

real and imaginary part of complex refraction coefficient, respectively. The generalized Drude-like model includes the inter-band transition from core electrons. The equation can be presented as:

$$\varepsilon_{gDrude}(\omega) = 1 - \frac{{\omega_p}^2}{\omega(\omega + i\Upsilon)} + \sum_{j=1}^{K} \frac{g_j}{{\omega_j}^2 - \omega^2 - \mathrm{i}\Upsilon_j \omega} \quad (5\text{-}2)$$

where the $g_j$ are the oscillator strengths, the $\Upsilon_j$ are the relaxation frequencies and $\omega_j$are the resonant frequencies of the oscillators describing the core electrons. By fitting the imaginary part of eq.5-2 to the optical data which is $2n(\omega)k(\omega)$, we can have fit values for the parameters of the oscillators. Thus the dielectric permittivity along the imaginary frequency axis $\varepsilon_{\mathrm{g-Drude}}(\mathrm{i}\xi)$ of generalized Drude can be obtained.

### ❖ Generalized plasma-like model

For the generalized plasma-like permittivity, we first need to subtract the Drude behavior of the conduction electrons from the tabulated optical data. The residual is then fit to six oscillators and their parameters are determined as before. The generalized plasma-like model which is given by:

$$\varepsilon_{gPlasma}(\omega) = 1 - (\frac{\omega_p}{\omega})^2 + \sum_{j=1}^{K} \frac{g_j}{{\omega_j}^2 - \omega^2 - \mathrm{i}\Upsilon_j \omega} \quad (5\text{-}3)$$

After obtaining $\varepsilon_{\mathrm{g-Drude}}(\mathrm{i}\xi)$ and $\varepsilon_{\mathrm{g-plasma}}(\mathrm{i}\xi)$ from both models, the theoretical Casimir pressure can be obtained from the Lifshitz equation.

### 5.2.2 Comparison of results

In the Fig.5-7 (a),(b),(c),(d) we compare the experimental data of the measured mean Casimir pressure including the total error bar with the two generalized models from 230nm to 410nm. The size of the total error bar is small enough to tell the difference between generalized Drude and Plasma model. Therefore, the experimental curve is in a good agreement with generalized Plasma model computed from the tabulated data. It is worth pointing out that the differences between the two models cannot be explained as an error in the measurement of the separation distance. Therefore, the experimental curve which is in a good agreement with the generalized Plasma model cannot be fit with a shift of a few nanometers of the experimental curve onto the generalized Drude model. This is because the curvature of the two models are different. For example, if we shift the experimental curve by 2.5nm towards the Drude model, there will be only small range of 240~280nm is in good agreement with Drude model but starts to deviate from 280nm. Thus this is added proof that errors in the separation distance cannot lead to an overlap with the Drude model. Additionally the shift of 2.5 nm required is much larger than the error of 0.4 nm in the separation distance.

However, in the Fig. (a), the mean value of Casimir pressure curve (blue dots) is slightly smaller than the generalized Plasma model. A possible reason is that the Au film used is slightly different from that in the optical data. . In this generalized Plasma theory curve as shown in Fig. 5-7 with black solid line, the plasma frequency is ~8.9 e.V. But the Plasma frequency we measured using ellipsometry is ~6.4 e.v. (These ellipsometry data is not shown in my thesis). It implies that the theoretical magnitude of the Casimir

pressure in will be slightly decreased which suggests that our experimental curve might be more in agreement with the generalized Plasma model. (The completed analysis considering spectroscopic data will be presented in a future paper ).

Furthermore, for statistical approaches to comparing experiment with theory, we need to provide the confidence interval for difference between the theory and experimental curve. Below, we follow the procedures from the book " Advances in the Casimir Effect[54] (Chapter18)". In the first step, the total experimental error including standard random errors and systematic errors must be ascertained regardless of the theory to be used. The second step is the uncertainties from the theory used. Finally, the statistical approach to experimental curve is explained by 95% confidence interval which can be used to describe the reliability of the results.

The confidence interval for the difference between theory and experimental data at a 95% confidence level is given by $[-\Xi_{\Pi}(\mathrm{Z}), \Xi_{\Pi}(\mathrm{Z})]$ ,where $\Xi_{\Pi}(\mathrm{Z})$ is determined from the equation[56]:

$$\Xi_{\Pi}(\mathrm{Z}) = k_{\mathcal{H}}^{(2)} \sqrt{[\Delta^{\mathrm{tot}}\Pi^{\mathrm{theory}}(\mathrm{Z})]^2 + [\Delta^{\mathrm{tot}}\Pi^{\mathrm{expt}}(\mathrm{Z})]^2} \qquad (5\text{-}4)$$

where $\Delta^{\mathrm{tot}}\Pi^{\mathrm{expt}}(\mathrm{Z})$ stands for total error at 95% confidence level including random error $\Delta^{\mathrm{random}}\Pi^{\mathrm{expt}}(\mathrm{Z})$ and systematic error $\Delta^{\mathrm{syst}}\Pi^{\mathrm{expt}}(\mathrm{Z})$ . $\Delta^{\mathrm{tot}}\Pi^{\mathrm{expt}}(\mathrm{Z})$ is the theoretical errors representing the accuracy of the theory. "Z" is separation distance between sphere and plate and $k_{\mathcal{H}}^{(2)}$=1.1 with 95% confidence level.

To have a conservative value of the total experimental error, we must combine random errors described by student-T distribution and systematic errors described by a

uniform distribution. Based on student-T distributions (as the number of samples is small ), the one sided 95% confidence level of our random errors is our mean value of random error (0.5mPa) times the student-t coefficient for n=3 (2.920) which is equal to 1.46 mPa. The systematic error as we mentioned in previous section, is the second kind of systematic errors coming from a calibrated device which is the smallest fractional division of the scale of the device at the limits of this range, The systematic errors are considered as random quantities characterized by a uniform distribution. Therefore, the 95% confidence level for the total systematic error is given by :

$$\Delta^{\mathrm{syst}}\Pi^{\mathrm{expt}}(\mathrm{Z}) = k_{\mathcal{H}}^{(J)} \sqrt{\sum_{i=1}^{J} (\Delta_{\mathrm{i}}^{\mathrm{sys}}\Pi^{\mathrm{expt}}(\mathrm{Z}))^2}$$

(5-5)

where $\mathcal{H}$ is the confidence level and $k_{\mathcal{H}}^{(J)}$ is the tabulated coefficient depending on $\mathcal{H}$ and on the total number of systematic errors J. Here we have two sources of systematic errors which indicate as J=2. For our case ,$\mathcal{H}$ is equal to 0.95 (95%) which means $k_{0.95}^{(2)}$ is equal to 1.1. Therefore, the 95% confidence level of our total systematic error varies from 1.1*2mPa (2.2mPa) at z=230nm to 1.1*1.5mPa (1.65mPa) at all separations when Z > 400nm.

The total experimental error is given by :

$$\Delta^{\mathrm{tot}}\Pi^{\mathrm{expt}}(\mathrm{Z}) = \mathrm{q}_{\mathcal{H}}(\mathrm{r})[\Delta^{\mathrm{random}}\Pi^{\mathrm{expt}}(\mathrm{Z}) + \Delta^{\mathrm{syst}}\Pi^{\mathrm{expt}}(\mathrm{Z})] \qquad (5\text{-}6)$$

where $q_{\mathcal{H}}(r)$ is determined by ratio of between systematic errors and random errors. At a 95% confidence level ($\mathcal{H} = 0.95$), $q_{\mathcal{H}}(r)$ varies between 0.71 and 0.81. Here, to be conservative, we used $q_{0.95}(r) = 0.8$.

Basically, the theoretical errors originate from (1) the dielectric permittivity of material we used for the Lifshitz theory. (2) deviation of the boundary surface (roughness) (3) the proximity force approximation we used with the configuration of a sphere and plate. (4) the errors in the measurement of the separation distance δZ which propagates into theory when we compare theory and experiment. Here, for simplicity, we only discuss the theoretical error from (4) because (1),(2) and (3) are relatively small compared to (4).

With the definition of error propagation, the errors due to δZ are presented as :

$$\Delta^{tot}\Pi^{theory}(Z) = \delta P^{casimir}(Z) = \frac{\partial P^{casimir}}{\partial Z}\delta Z \qquad (5\text{-}7)$$

where δZ is ~0.4nm as described from Table 5-1. Therefore, the confidence interval for the difference between theory (generalized Drude and Plasma model) and experimental data at a 95% confidence level can be calculated with eq.5-4 and is shown in Fig. 5-8.

In the Fig. 5-8, the blue solid lines and green lines indicate the single sided border of the 95% confidence level for generalized Plasma and Drude model, respectively. The red square dots indicate the difference between experimental data and generalized Drude model. Within the range of separations from 230 to 500nm the generalized Drude model approach is excluded experimentally at a 95% confidence level. The black dots represent

the difference between the experimental data and the generalized Drude model. As shown in Fig. 5-8, all dots are well below the 95% confidence level at all separations considered. This implies that the experimental data are consistent with the theory based on the generalized plasma-like dielectric permittivity.

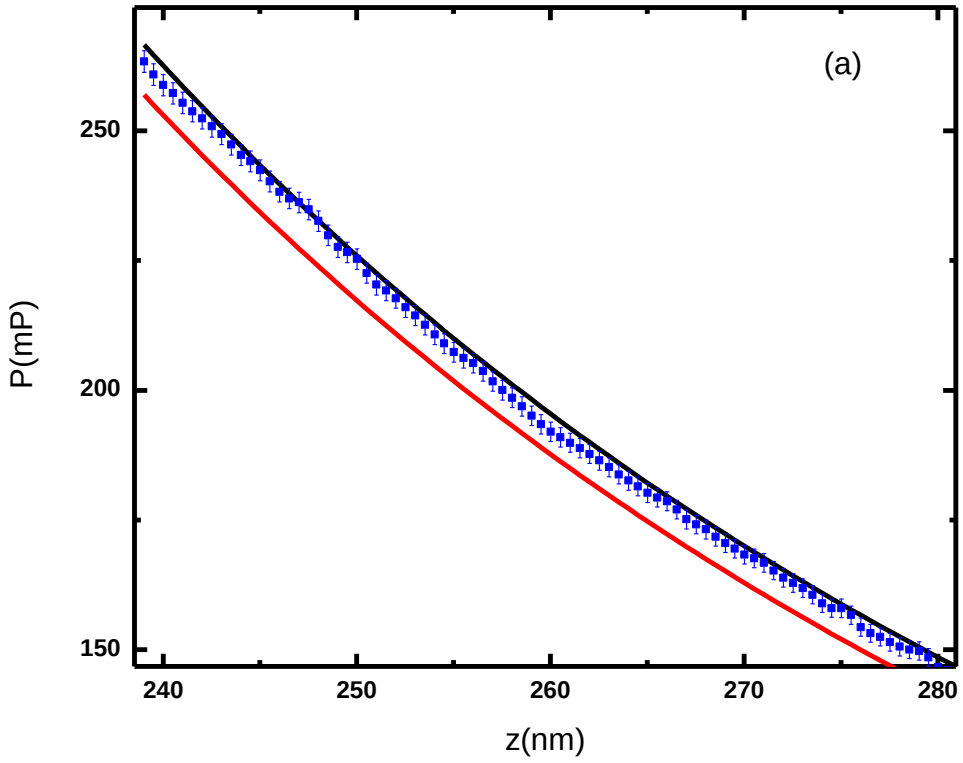

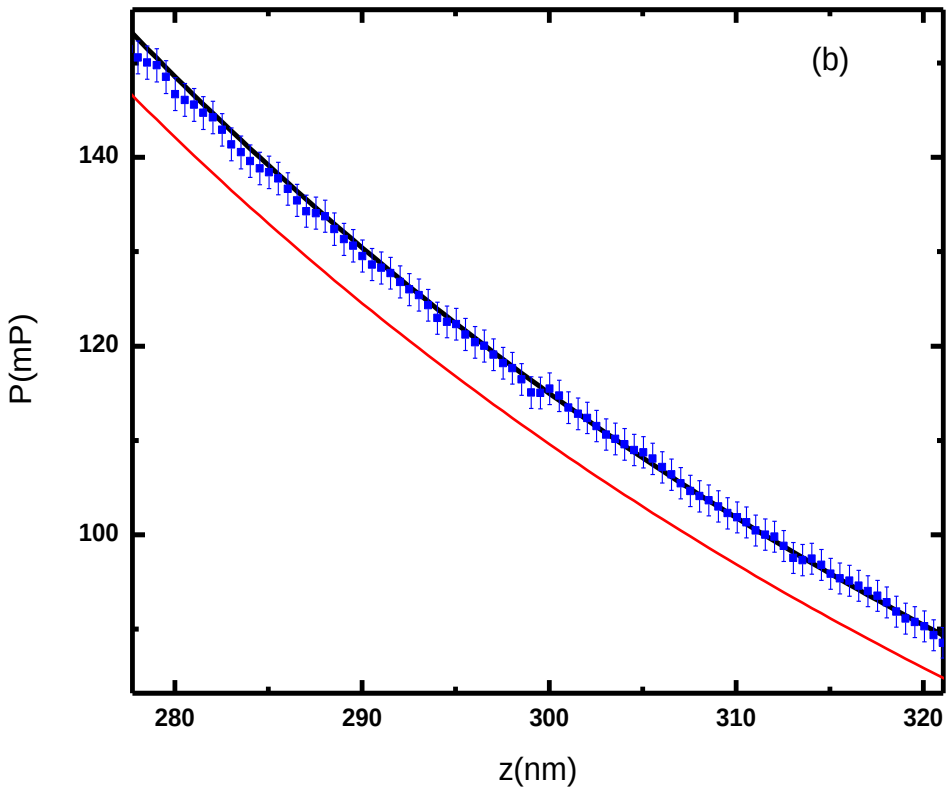
(b)
140
120
100
P(mP)
280
290
300
310
320
z(nm)

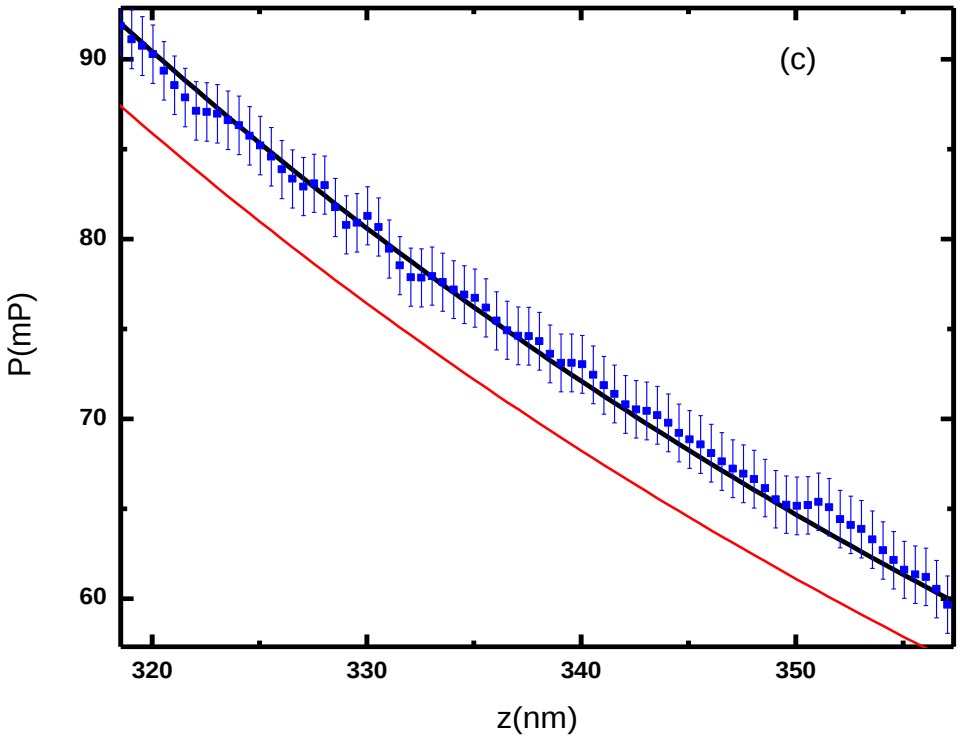
(c)
90
80
70
60
P(mP)
320
330
340
350
z(nm)

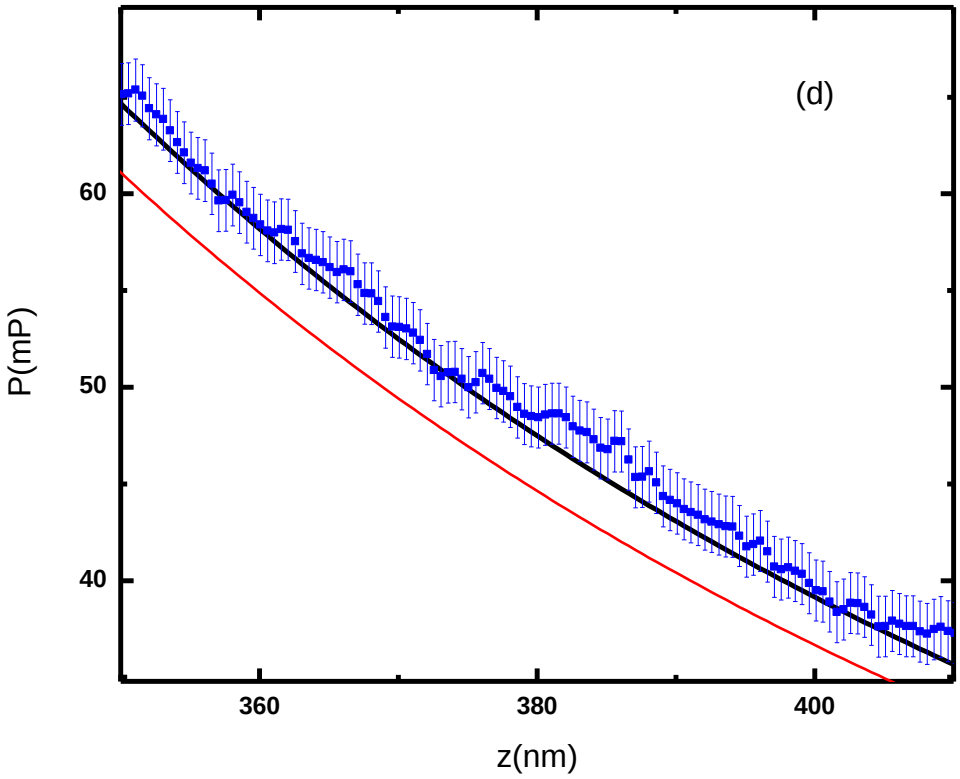


Figure 5- 7 In (a)(b)(c)(d), the blue square dots are the experimental mean value of Casimir pressure with total error bars. The red solid line is the generalized Drude model and the black line represent generalized plasma model.

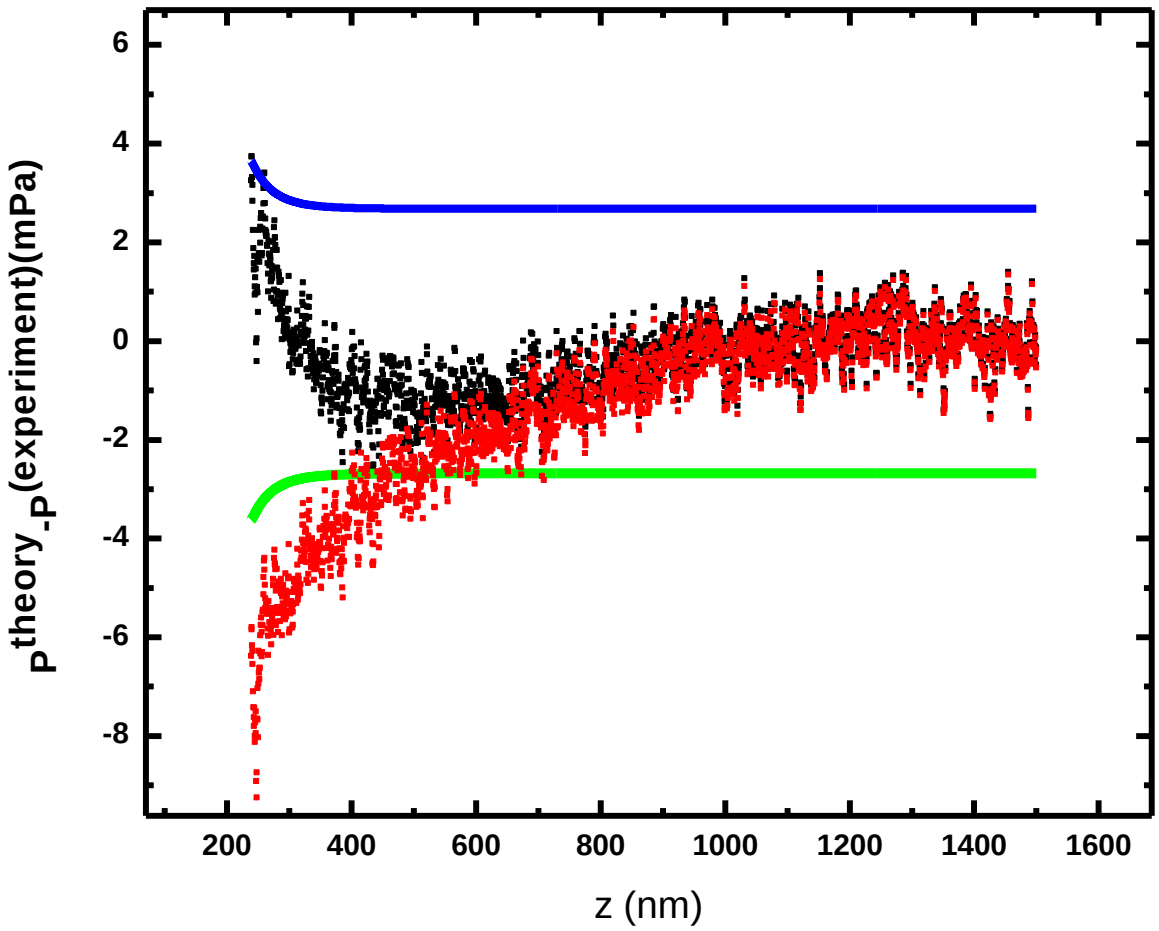


Figure 5- 8 Difference between theory (generalized Drude-red dots and Plasma-black dots model) and experimental Casimir pressure versus separations. The solid blue and green lines indicate the 95% confidence levels of generalized Plasma and generalized Drude model, respectively.

## 5.2 Preliminary experimental results for the Casimir force between an Au-coated sphere and ITO-coated plate (work in progress)

One of our motivations to investigate the Casimir effect is because of its application in nanotechnology. The continual drive to increase the functionality while minimizing energy consumption will lead to shrinking device sizes. Not only are features of the device smaller but also the separation distance between them. When separations become smaller, the Casimir force will be gradually dominate in the sub micrometer scale. Therefore, the Casimir force might cause stiction, in other words, malfunction of nano or submicron scale devices. Therefore, neutralizing the Casimir force using transparent electrodes such as Indium Tin Oxide coated on quartz plate might be a good solution for the future.

Here we demonstrate the Casimir pressure between an Au-coated sphere and ITO-coated plate without any comparison with theory. We used an ITO plate with a sputtered layer of ~100nm on a Quartz plate. The ITO sample resistivity was 7.2 (Ω/□). Fig.5-9 shows the SEM picture of ITO film where surface is very smooth. Fig. 5-10 indicate the roughness amplitude which is 2.08nm measured by using an AFM.

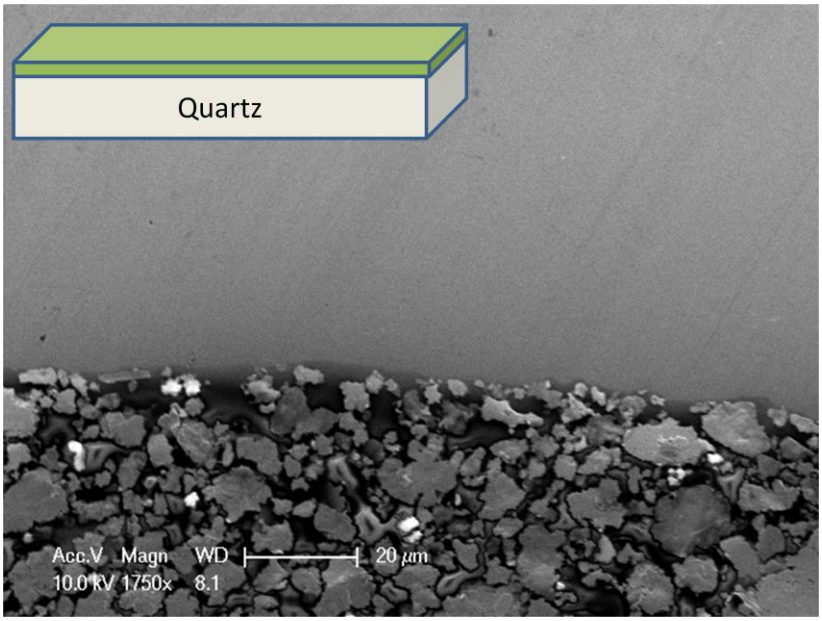


Figure 5- 9 SEM picture for the ITO film used. The grainy image below the film is that of the silver epoxy used to fix the sample for the analysis.

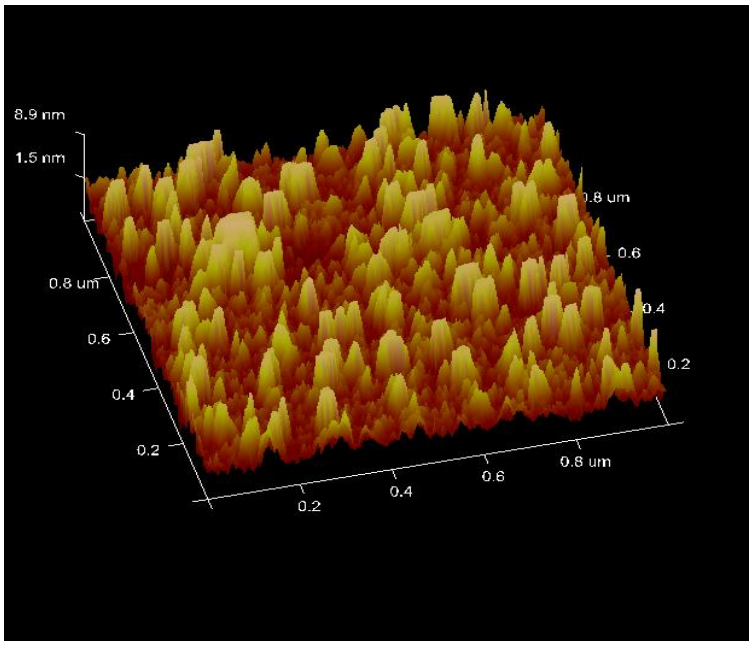


Figure 5- 10 The 3D image of ITO surface is taken using an AFM.

In figure 5-11, we present a single scan of the Casimir pressure and compare it with the measured pressure between an Au sphere and Au plate. The same procedures used for the case of two Au surfaces discussed above was followed in the case of the Au sphere and ITO plate. . Table 5-1 indicates the ratio of the Casimir pressure (AU/ITO) between the Au sphere and ITO plate to that between an Au sphere and Au plate at different separation distances.

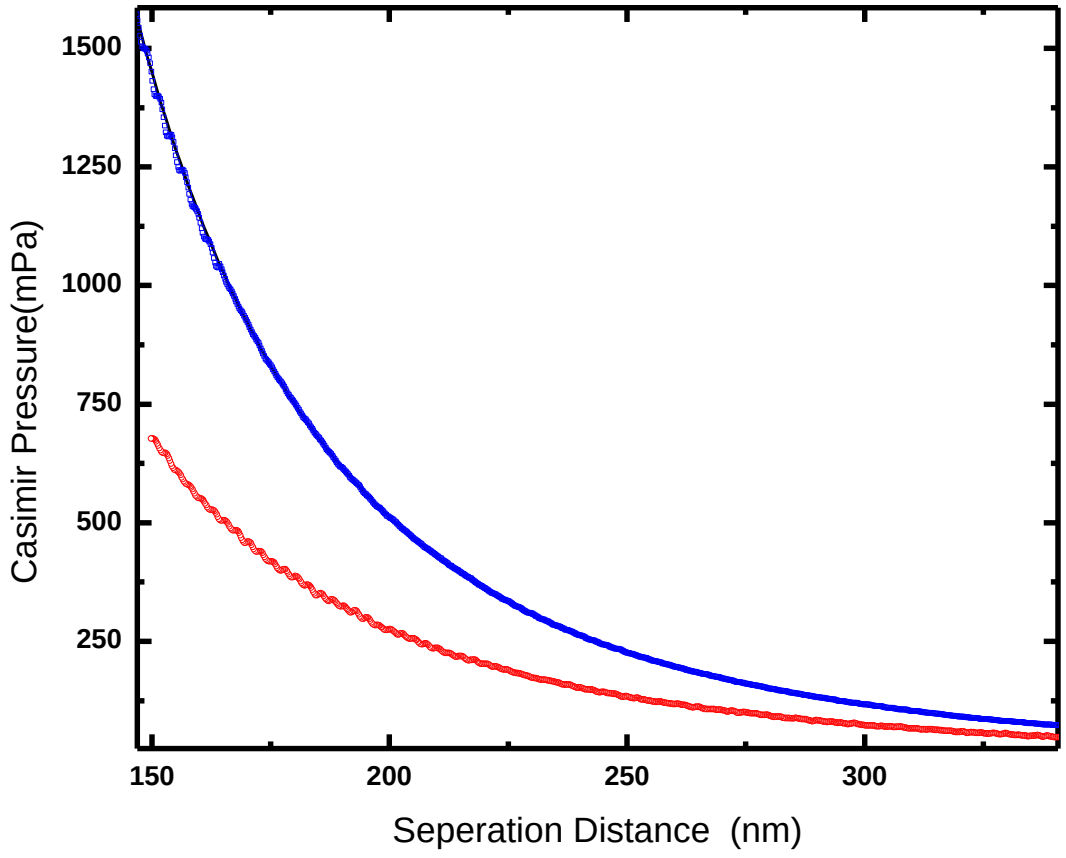


Figure 5- 11 The blue line indicates the measured Au-Au Casimir pressure. The red line is the measured Au-ITO Casimir pressure curve.

| Z (nm) | ITO (mPa) | Au(mPa) | Ratio(Au/ITO) |
|---|---|---|---|
| **150** | **677.21** | **1430.83** | **2.11** |
| **175** | **418.50** | **831.30** | **1.99** |
| **200** | **275.67** | **511.27** | **1.85** |
| **250** | **133.43** | **225.70** | **1.69** |
| **300** | **72.99** | **116.54** | **1.60** |

Table 5- 2 A factor of 2.11 reduction of Casimir pressure at 150nm is obtained by using an ITO plate in comparison to an Au plate.

# Chapter 6 Conclusion and future works

## 6.1 Conclusion

One of the motivations in investigating the Casimir effect is the puzzles in the application of the Lifshitz equation to real metals. To carry out this goal, we developed a FM force microscopy technique based on a short coherence length fiber-optic interferometer for precise dynamic Casimir measurement. In our measurement, the Casimir force between an Au sphere and an Au plate which using PFA is related to the Casimir pressure between two Au plates was measured with a precision of 1.5mPa. With this error, we are able to tell the difference between generalized Drude model and generalized Plasma model description of the permittivity of Au. The experimental curve is in a good agreement with generalized Plasma model at separations from 230nm to 410nm. It is worth pointing out that the differences between the two models cannot be explained as an error in the measurement of the separation distance, since the differences between the two theoretical curves vary as a function of the separation distance. Therefore, our results may imply that the model with energy dissipation for the conduction electrons will give discrepancies when comparing the theory including the thermal correction. In other words, our experimental results suggests physical insight thought that the energy exchange in materials with real photons or virtual ones might be different.

The Casimir force can be reduced by using conductive oxide (ITO) which is transparent to reduce the Casimir attractive force to half its original value but conductive enough to prevent surface charge accumulation. We have measured the Casimir pressure between an ITO sample plate and Au-coated sphere in vacuum . There is a factor of ~ 2 Casimir pressure reduction with the used of the ITO plate at separation distance of 160nm.

These findings, however, are slightly inconsistent with D.Iannuzzi et.al[57] results at large separations. Therefore, this may suggest to us that Casimir force measurements might be slight different in vacuum and in an air environment.

# 6.1 Future work

## 6.1.1 Increase force sensitivity in our system

To provide deeper insights into the Casimir effect, the increase in the sensitivity of the dynamic Casimir force measurement technique is our first concern. Below, we suggest directions to improve dynamic force measurement in our system.

- **Fabricating new sensor (work in progress)**

In the dynamic measurement technique, adding the mass of sphere will cause the sensitivity to decrease as mentioned in chapter3. Increasing the size of the sphere to increase the force and the resultant sensitivity, will lead the Q value to degrade dramatically because of unsymmetrical attachment of the sphere or the local deviations

from perfect spherical shape. For solving these problems, we plan to apply clean room micro fabrication technique to construct a cantilever with a spherical bottom made of a partial sphere at the end. This will reduce the attached mass and also prevent poor unsymmetrical attachment of the sphere. . We will use the standard cantilever fabrication techniques and combine it with the micro-lens construction technique (by ICP, photo-resist reflow, photolithography) to make our low noise spherical sensor. The Fig.6-1 shows each step for the proposed spherical sensor fabrication.

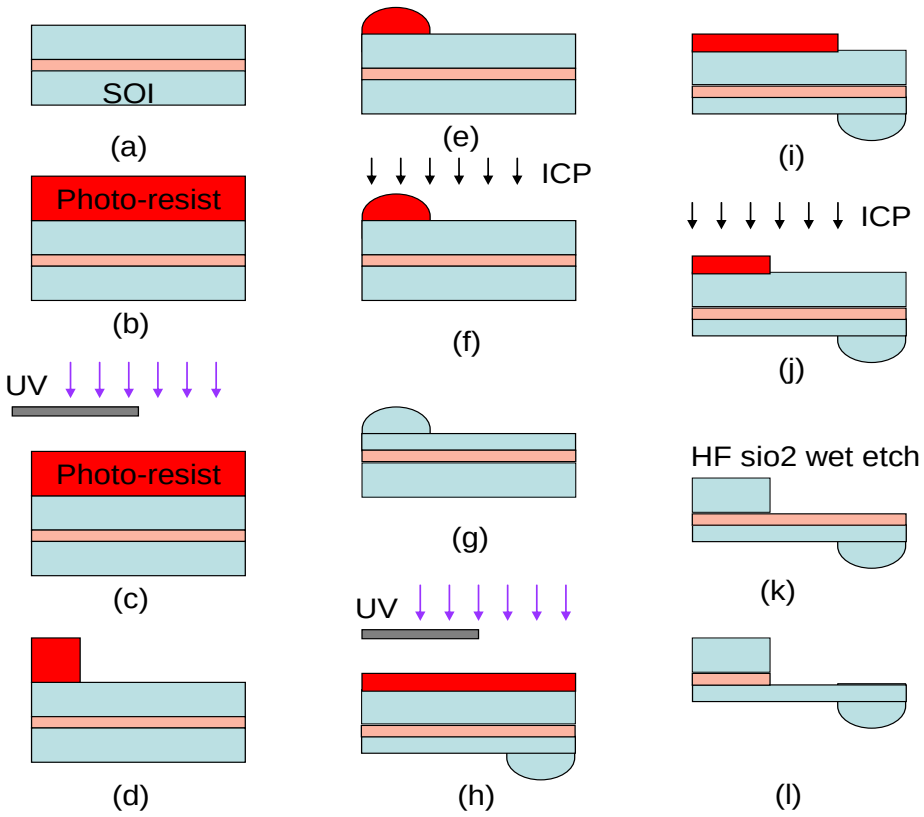


Figure 6- 1 The process for the fabrication of the spherical sensor (a) SOI wafer (b), (c), (d) pattern resist. (e) Reflow the Photo-resist (f) ICP transfer pattern to silicon wafer (g)(h)(i)(j)(k)(l) cantilever fabrication with backside etch and SiO2 layer wet etch.

However, right now we have a problem when we transfer the pattern to silicon wafer. Because the ICP chamber was always contaminated by the residual chemicals. as shown in Fig. 6-2, when we transfer the pattern, the residual chemicals lead to a very rough silicon surface (annealing the Si surface might solve the problem).

(a) (b)

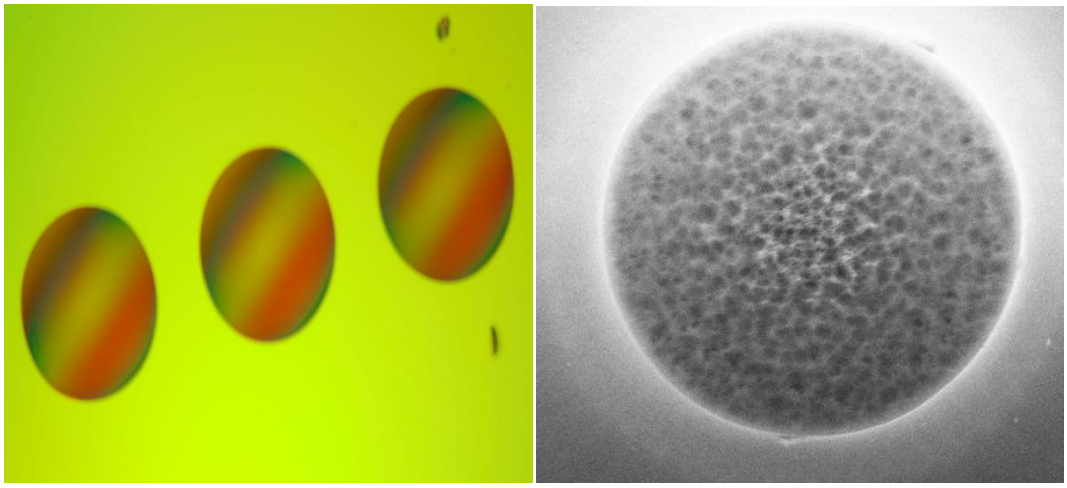

Figure 6- 2 Image (a) was taken with an optical microscope, before transferring pattern by ICP. From the optical pattern, we know the surface of reflowed photo-resist was smooth. Fig.(b) Shows the SEM image, after ICP etch (using $SF_6$ and $O_2$ etchant).

- **Using close loop piezo system for sample plate and**

One of methods to improve signal to noise ratio is to reduce the detection bandwidth $B_w$ as we mentioned in chapter 3. With a closed loop control at each sample position, we can average our frequency shift signal to approach 6mHz (phase detector limit) resolution limit of our PLL. This might lead to the systematic error of Casimir pressure being reduced down to 0.2mPa which is one order magnitude smaller than what is reported here.

- **Varying cantilever amplitude at different separation distance**

Another way to have better signal to noise ratio is using a larger driving amplitude on the cantilever. However, using higher amplitude means that we might go outside the range of using only the first derivative of the force at very short distances. This problem can be solved if we vary amplitude at different separation distance. Thus small amplitudes will be used at short distances and large amplitudes at large separation distances.

# REFERENCES


[1] H.B.G. Casimir, *Proc. Kon. Ned. Akad. Wet.* **51**, 793 (1948).

[2] I. E. Dzyaloshinskii, E. M. Lifshitz, and L. P. Pitaevskii, *Advances in Physics* **10** (38), 165 (1961).

[3] JACOB ISRAELACHVILI, *Intermolecular & Sruface Forces* SENOND ed. (ACADEMIC PRESS); J.N. Israelachvili and D. Tabor, *Proc. Roy. Soc. Lond. A* **331**, 19 (1972).

[4] F. London, *Z. Phys* (63), 245 (1930).

[5] E.M. Lifshitz, *Sov. Phys. JETP*, **2** (73-83) (1956).

[6] M. Bordag, U. Mohideen, and V. M. Mostepanenko, *Physics Reports-Review Section of Physics Letters* **353** (1-3), 1 (2001).

[7] V. M. Mostepanenko and N N Trunov, *Soviet Physics Uspekhi* **31** (11), 965 (1988).

[8] Grütter Plunien, Berndt M.ler, and Walter Greiner, *Physics Reports* **134** (2-3), 87 (1986); Mehran Kardar and Ramin Golestanian, *Reviews of Modern Physics* **71** (4), 1233 (1999); S K Lamoreaux, *REPORTS ON PROGRESS IN PHYSICS* **68** (1), 201 (2005); V. A. Parsegian, *van der Waals Forces: A Handbook for Biologists, Chemists, Engineers, and Physicists* (Cambridge University Press, Cambridge, 2005).

[9] E. Buks and M. L. Roukes, *Physical Review B* **63** (3), 033402 (2001); E. Buks and M. L. Roukes, *Europhysics Letters* **54** (2), 220 (2001).

[10] R. S. Decca, E. Fischbach, G. L. Klimchitskaya et al., *Physical Review D* **68** (11), 116003 (2003).

[11] R. S. Decca, D. Lopez, E. Fischbach et al., *European Physical Journal C* **51** (4), 963 (2007); R. S. Decca, D. Lopez, E. Fischbach et al., *Physical Review D* **75** (7), 077101 (2007).

[12] F. Chen, G. L. Klimchitskaya, V. M. Mostepanenko et al., *Physical Review Letters* **97** (17), 4 (2006).

[13] F. Chen, G. L. Klimchitskaya, V. M. Mostepanenko et al., *Physical Review B* **76** (3), 15 (2007); F. Chen, G. L. Klimchitskaya, V. M. Mostepanenko et al., in *Optics Express* (2007), Vol. 15, pp. 4823.

[14] H. B. Chan, V. A. Aksyuk, R. N. Kleiman et al., *Science* **291** (5510), 1941 (2001).

[15] H.B. Chan, V.A. Aksyuk, R.N. Kleiman et al., *Physical Review Letters* **87**, 211801 (2001).

[16] F. M. Serry, D. Walliser, and G. J. Maclay, *Journal of Applied Physics* **84** (5), 2501 (1998).

[17] Larry Hardesty, Mysterious quantum forces unraveled, (2010).

[18] Larry Hardsty http://web.mit.edu/newsoffice/2010/casimir-0511.html, *MIT News Office* (2010).

[19] M.J. Sparnaay, *Physica* **24**, 751 (1958).

[20] A. Roy, C.Y. Lin, and U. Mohideen, *Physical Review D* **60**, (R)111101 (1999).

[21] A. Roy and U. Mohideen, *Physical Review Letters* **82**, 4380 (1999); F. Chen and U. Mohideen, *Journal of Physics A-Mathematical and General* **39** (21), 6233 (2006); F. Chen, U. Mohideen, G. L. Klimchitskaya et al., *Physical Review A (Atomic, Molecular, and Optical Physics)* **72** (2), 20101 (2005); F. Chen, U. Mohideen, G. L. Klimchitskaya et al., *Physical Review A (Atomic, Molecular, and Optical Physics)* **74** (2), 022103 (2006); R. Castillo-Garza, C. C. Chang, D. Jimenez et al., *Physical Review A* **75** (6), 062114 (2007).

[22] F. Chen and U. Mohideen, *Review of Scientific Instruments* **72** (7), 3100 (2001).

[23] U. Mohideen and A. Roy, *Physical Review Letters* **81**, 4549 (1998); F. Chen, G. L. Klimchitskaya, U. Mohideen et al., *Physical Review A* **69** (2), 022117 (2004).

[24] G. Bressi, G. Carugno, R. Onofrio et al., *Physical Review Letters* **88** (4), 041804 (2002).

[25] R. S. Decca, oacute, D. lópez et al., *Physical Review Letters* **91** (5), 050402 (2003).

[26] R. S. Decca, D. López, H. B. Chan et al., *Journal of Low Temperature Physics* **135** (1), 63 (2004); R. S. Decca, D. Lopez, E. Fischbach et al., *Annals of Physics* **318** (1), 37 (2005).

[27] H. B. Chan, Y. Bao, J. Zou et al., *Physical Review Letters* **101** (3), 030401 (2008).

[28] M. Bordag, U. Mohideen, and V. M. Mostepanenko, *Physics Reports* **353** (1-3), 1 (2001).

[29] G. L. Klimchitskaya, U. Mohideen, and V. M. Mostepanenko, *Reviews of Modern Physics* **81** (4), 1827 (2009).

[30] M. Bordag, G.L. Klimchitskaya, and V.M. Mostepanenko, *International Journal of Modern Physics A* **10**, 2661 (1995); G. L. Klimchitskaya, A. Roy, U. Mohideen et al., *Physical Review A* **60** (5), 3487 (1999).

[31] M. Bordag, G.L. Klimchitskaya, U. Mohideen et al., *Advances in the Casimir Effect*. (Oxford Univesity Press, Oxford, 2009).

[32] M. Bostrom and B.E. Sernelius, *Physical Review Letters* **84**, 4757 (2000); G. Genet, A. Lambrecht, and S. Reynaud, *Physical Review A* **62**, 012110 (2000); M. Bordag, B. Geyer, G.L. Klimchitskaya et al., *Physical Review Letters* **85**, 503 (2000); Roya Zandi, Thorsten Emig, and Umar Mohideen, *Physical Review B* **81** (19), 195423.

[33] V. M. Mostepanenko and B Geyer, *Journal of Physics A: Mathematical and Theoretical* **41** (16), 164014 (2008).

[34] V.B. Bezerra, G.L. Klimchitskaya, and V.M. Mostepanenko, *Physical Review A* **66**, 062112 (2002).

[35] Franz J. Giessibl, *Reviews of Modern Physics* **75** (3), 949 (2003).

[36] Yozo Kanda, *Sensors and Actuators A: Physical* **28** (2), 83 (1991); Mo Li, H. X. Tang, and M. L. Roukes, *Nat Nano* **2** (2), 114 (2007).

[37] Takeshi Fukuma, Masayuki Kimura, Kei Kobayashi et al., *Review of Scientific Instruments* **76** (5), 053704 (2005).

[38] D. Rugar, H. J. Mamin, R. Erlandsson et al., *Review of Scientific Instruments* **59** (11), 2337 (1988).

[39] D. Rugar, H. J. Mamin, and P. Guethner, *Applied Physics Letters* **55** (25), 2588 (1989).

[40] C. Schonenberger and S. F. Alvarado, *Review of Scientific Instruments* **60** (10), 3131 (1989).

[41] U. Mohideen and A. Roy, *Physical Review Letters* **83** (16), 3341 (1999); F. Chen, U. Mohideen, G. L. Klimchitskaya et al., *Physical Review Letters* **88**, 101801 (2002).

[42] Y. Martin, C. C. Williams, and H. K. Wickramasinghe, *Journal of Applied Physics* **61** (10), 4723 (1987).

[43] H. R. Steinauer U. Dürig, and N. Blanc, *J. Appl. Phys.* **82**, 3641 (1997).

[44] Mervyn Miles, *Science* **277** (5333), 1845 (1997); T. R. Albrecht, P. Grütter, D. Horne et al., *Journal of Applied Physics* **69** (2), 668 (1991).

[45] CHRISTOPHER C. DAVIS JOHN H. MOORE, MICHAEL A. COPLAN, *BUILDING SCIENTIFIC APPARATUS* 3rd ed.

[46] T. R. Albrecht, P. Grütter, D. Horne et al., *Journal of Applied Physics* **69** (2), 668 (1991).

[47] D. Huang, E. A. Swanson, C. P. Lin et al., *Science* **254** (5035), 1178 (1991); Jackson D. A. Jones R. and Shannon C. Rao Y J, *J. Lightwave Technol.* **12** (9), 1685 (1994); Ning Y. N. and Jackson D. A. Rao Y J, *Opt. Lett.* **18** (6), 462 (1993); Y. J. and Jackson D. A. Rao, *Proc. SPIE* **2292** (1994).

[48] R. Castillo-Garza, Chang Chia-Cheng, Yan Dong et al., *Journal of Physics: Conference Series* **161**, 012005 (9 pp.) (2009).

[49] Franz J. Giessibl and Marco Tortonese, *Applied Physics Letters* **70** (19), 2529 (1997).

[50] A. N. Cleland and M. L. Roukes, *Journal of Applied Physics* **92** (5), 2758 (2002).

[51] U. Durig, O. Zuger, and A. Stalder, *Journal of Applied Physics* **72** (5), 1778 (1992).

[52] F. C. FITCHEN C. D. MOTCHENBACHER, *Low-Noise Electronic Design*. (JOHN WILEY & SONS, NEW YOUR).

[53] Fischbach E. Klimchitskaya G. L. Krause D. E. López D. and Mostepanenko V. M. Decca R S, **68** (11), 116003 (2003); G.L. Klimchitskaya, U. Mohideen, and V.M. Mostepanenko, *Reviews of Modern Physics* **81** (4), 1827 (2009).

[54] G.L.KLIMCHITSKAYA M.BORDAG, U.MOHIDEEN, V.M. MOSTEPANENKO, *Advances in the Casimir Effect*. (Oxford university Press, 2009).

[55] William R. Smythe, *Electrostatics and Electrodynamics*. (McFraw-Hill, New York, 1950).

[56] S. G. Rabinovich, *Measurement Errors and Uncertainties : Theory and Practice*. (Springer, New York, 2000).

[57] S. de Man, K. Heeck, R. J. Wijngaarden et al., *Physical Review Letters* **103** (4), 040402 (2009).